STUDY OF CONJUGATE HEAT TRANSFER OF A SPARK-IGNITED NATURAL GAS ENGINE CYLINDER

A Dissertation

by

ALIREZA SADEGH MASHAYEKH

Submitted to the Office of Graduate and Professional Studies of
Texas A&M University
in partial fulfillment of the requirements for the degree of

DOCTOR OF PHILOSOPHY

Chair of Committee,	Timothy Jacobs
Committee Members,	Jerald Caton
	Je-Chin Han
	Hamn-Ching Chen
Head of Department,	Andreas A. Polycarpou

August 2017

Major Subject: Mechanical Engineering

ABSTRACT

Large bore two-stroke natural gas engines are facing more stringent emission regulations in the near future. In order to comply with these new regulations, engine manufacturers have to modify their engines. Redesigning some relevant parts and/or modifications to the combustion setup of these engines are in order. A deeper understanding and analysis of all the details of the combustion process could help researchers/engineers in these modifications. While the experimental methods are still the primary way of analyzing internal combustion engines, recent advances in numerical methods, and the computing power of clusters (supercomputers) have opened a new path ahead of engine designers. Using numerical tools could significantly reduce the costs associated with engine modifications.

Three-dimensional CFD tools are the most accurate and detailed numerical tools available for engine research. CFD simulations of engines could reveal all the details of all the processes that happen in an engine: the air and fuel intake, mixing of the two, scavenging process, and the power cycle are some of the processes that could be looked into, using CFD tools.

The current study represents the numerical simulation of a large bore natural gas engine, using a commercial CFD software package, along with the required experimental study to validate the results of the simulation work. This document includes the case setup process for the numerical simulation, which includes the simulation of the reed valve (the air/fuel ratio control system of the engine), the simulation of the scavenging process, the simulation of the combustion process, and the conjugate heat transfer simulation between the solid parts of the engine and the cooling system. The study of conjugate heat transfer -which is the main objective of this research- provides researchers with the spatial temperature distribution on all the parts surrounding the combustion chamber. The results

show relatively higher temperatures near and around the spark plug and the air-start cavity. These results could be used for an improved mechanical design of relevant parts, and redesign of parts and/or combustion/cooling setup to reduce the emission production.

The simulation results were all validated by experimental data. Stuffing box pressure, in-cylinder pressure, and equivalence ratio of the stuffing box mixture were the validation criteria for the numerical results. In addition, a single temperature measurement in the solid parts was used for partial validation of the CHT simulations. This dissertation discusses the test apparatus, and the process of acquiring the required experimental data for validation purposes as well.

DEDICATION

To my wife, Mahya, and my Parents.

ACKNOWLEDGMENTS

The guidance and assistance form my committee chair, Dr. Jacobs, is acknowledged humbly and gratefully. Additionally, I would like to thank my other committee members, Dr. Caton, Dr. Han, and Dr. Chen for their assistance and efforts in supporting this research.

GE Oil & Gas is acknowledged for generous financial and technical support of this research; any opinions expressed in the dissertation, whether direct or implied, are strictly those of the author, and do not necessarily represent those of the sponsoring agency. Further, I would like to thank Convergent Science for their generous support of the CONVERGE software. Texas A&M Super Computing Center is acknowledged for supporting the seating of the computational software.

In the past few years, I was honored to get to know and work with my fellow lab mates. In particular, I have to acknowledge Mr. Aaron Griffin and Mr. Jeff Brown for their contributions in the engine test cell.

I am forever indebted to my wonderful family; this success was not achievable without their support throughout my entire life. My parents were the ones, who always emphasized to me the value of the knowledge; for that, I am always grateful and humble to them.

I cannot put it in words how grateful I am, to be blessed by having a kind, patient, and beautiful wife. It has been her love and support, which motivated me to break through all the hardship. I hope I can recompense for a portion of her devotion.

Above all, however, I have to emphasize that I owe all my life, and all that I have achieved to the God Almighty, and I pray every single day, to be blessed with his guidance for the rest of my life.

CONTRIBUTORS AND FUNDING SOURCES

Contributors

This work was supported by a dissertation committee consisting of Professor Timothy Jacobs [advisor], Professor Jerald Caton, and Professor Je-Chin Han of the Department of Mechanical Engineering and Professor Hamn-Ching Chen of the Department of Ocean Engineering.

All other work conducted for the dissertation was completed by the student independently.

Funding Sources

This work was made possible by GE Oil & Gas.

NOMENCLATURE

AERL	Advanced engine research lab
AFR	Air/fuel ratio
AMR	Adaptive mesh refinement
ATDC	After top dead center
BDC	Bottom dead center
BHP	Brake horse power
BMEP	Brake mean effective pressure
BTU	British Thermal Units
CAD	Crank angle degree
CFD	Computational fluid dynamics
CHT	Conjugate heat transfer
CMCV	Charge motion control valve
COV_{IMEP}	Coefficient of variability of IMEP
DAQ	Data acquisition system
DASI	Diesel assisted spark-ignition
DI	Direct injection
DMR	Dynamic mechanism reduction

Dyno	Dynamometer
EPC	Exhaust port close
EPO	Exhaust port open
FEM	Finite element method
FSI	Fluid structure interaction
GDI	Gasoline direct-injection
gpm	Gallons per minute
HC	Hydrocarbon
HCCI	Homogeneous charge compression ignition
HSDI	High-speed direct-injection
HTC	Heat transfer coefficient
IMEP	Indicated mean effective pressure
IPC	Intake port close
IPO	Intake port open
LDA	Laser Doppler anemometer
PDB	Pressure difference-based
ppr	Pulses per revolution

RANS	Reynolds-averaged Navier-Stokes
RNG	Re-normalization group
RPM	Revolutions per minute
SG-SIDI	Spray-guided spark-ignited direct-injection
SIDI	Spark-ignited direct-injection
STL	Standard triangle language
TCDI	Turbo-charged direct-injection
TDC	Top dead center
TKE	Turbulent kinetic energy
UDF	User-defined function
UHC	Unburnt hydrocarbon
V_c	Clearance volume
V_d	Displacement volume

TABLE OF CONTENTS

Page

LIST OF FIGURES

FIGURE Page

LIST OF TABLES

TABLE Page

1. INTRODUCTION

AJAX E-565 is a single-cylinder, two-stroke, large bore, spark-ignited natural gas engine, which has always been an important player in oil industry. This engine has provided pumping units with smooth, stable power, while offering lower field costs, less maintenance requirement, and a rugged design. The AJAX E-565 is capable of working with variable fuel compositions -including both high and low BTU fuels, and so is an easy choice for a reliable, continuous oilfield operation.

1.1 Background and Motivation

Large bore two-stroke engines are facing more stringent emission regulations in the near future. To meet these new regulations, some parts of the engines, and/or the combustion setup may need to be analyzed, and redesigned. There are different ways for analysis and modifications of engines, including experimental and numerical investigations. Additionally, some parts of the engine need to be redesigned for better mechanical endurance; for this purpose, the temperature distribution on these parts is required.

Experimental analysis and investigation of engines, not only are limited by instruments limitations, but also are cost prohibitive. Recently with advances in calculation powers of computers, and in CFD solvers, a new window has opened in front of researchers to analyze large bore engines; this provides engineers with a better understanding of all the details of fluid flow and combustion processes inside the chamber. In addition, other influential variables, important in engine efficiency and emission production can be analyzed.

Some of the important factors that affect the engine performance and emission production are listed:

- In-cylinder pressure, and temperature

- Temperature distribution inside the combustion chamber, and on its surrounding walls
- Port geometry, and scavenging method (2-stroke engines)
- Flame development characteristics
- Air/Fuel ratio control strategy
- Mixing characteristics inside the combustion chamber
- Location of the spark plug
- Spark timing, duration, and energy
- Fuel composition
- Burn rate, and heat loss

All of these factors influence both the engine performance, and the emission production of the engine. The old-school method of design, prototype, and test not only is intensely time-consuming; but also is very expensive. On the other hand, using numerical methods, in addition to reducing the required time, will broaden the understanding of many details that were not easily available through traditional analysis methods, such as fluid flow development, flame kernel growth, etc.

1.2 Objectives and Tasks

The ultimate objective of this project is to simulate, and analyze the conjugate heat transfer (CHT) in this engine's cylinder. Study of CHT in this engine will help researchers find the spatial temperature distribution in all the parts interfacing with engine coolant system; with this knowledge, relative parts of the engine, can be modified for improved engine efficiency, less emissions, and better mechanical endurance.

To reach the aforementioned objective, the following tasks should be done:

1. Simulation of the air and fuel intake to the engine's stuffing box and mixing:

   Building a model that can properly simulate this engine's reed valve is going to be the first task. This model should be able to predict the correct air-fuel ratio inside the stuffing box, which significantly affects the mixture in the combustion chamber, hence the combustion performance. The results acquired by this model should be validated by experimental data.

2. Simulation of the gas exchange process:

   The gas exchange process has significant effects on the mixing characteristics inside the combustion chamber, scavenging efficiency, and consequently the combustion performance.

3. Simulation of the combustion process:

   This will be the next milestone. To get this task done, the two previous tasks have to be accomplished. The results of this part of the simulation will require experimental validation through comparison of in-cylinder pressure curves.

4. Simulation of the conjugate heat transfer between this natural gas engine's combustion chamber walls and its cooling system:

   The results of the combustion simulation will then be used to start the conjugate heat transfer simulations. Near-wall gas temperatures, and convective heat transfer coefficients calculated in the combustion simulation will be used to simulate the CHT between the solid parts and the cooling system. This will be the ultimate objective of this project.

2. LITERATURE REVIEW

Different types of engines have been thoroughly studied over the past century, and yet it seems like there is not enough understanding of all the details of the processes that happen inside an internal combustion engine. With limitations in the instruments, and possible experiments, there is a consensus that the numerical simulations can help reveal more details of these processes. The data acquired by the numerical simulation, can then be used to broaden the knowledge of researchers, and engineers about engines, hence helping them improve the design and performance of them. [4, 5, 6]

Many factors and variables can affect an internal combustion engine's performance, and efficiency. For a stuffing box-compression cross-scavenged two-stroke engine, the major ones could be listed as: 1) stuffing box charging with fresh air and fuel, 2) mixing characteristics of the air and the fuel inside the stuffing box, 3) scavenging, 4) combustion, and finally 5) heat transfer process. [1, 7, 8]

In this particular engine, the charging of the stuffing box happens through a spring-loaded reed valve. This means that a better understanding of the behavior of the reed valve can help improve the AFR (air-fuel ratio) control system of the engine [9]. The valve also contributes in the mixing of the air and the fuel inside the stuffing box, which ultimately will influence the combustion performance.

The gas exchange process (scavenging) will dictate the residual fraction in the combustion chamber, and is responsible for almost all the UHC emissions through short-circuiting. [1]

The combustion process is where the power is extracted from the engine; hence is the most important process to be looked at. The combustion is also responsible for almost all the emissions production; this means that a closer look at the combustion process might

help reduce the emissions production in the future.

The engines in general have to dissipate around one-third of the total energy released by the combustion through heat transfer [7]. A proper heat transfer is critical to keep the cylinder head/block temperatures down, within the tolerable range for the materials. For this reason, study of the heat transfer process through the combustion chamber walls, and the coolant flow, is of utmost importance. Knowing the wall temperatures, can help with proper mechanical design of the relevant parts. In addition, production of emissions such as nitrous oxides (NO_x) are temperature sensitive; meaning that reducing cylinder wall temperatures may reduce the production of these emissions [10, 11].

Rolf Reitz in his paper, "Directions in internal combustion engine research" [12] has described the potential of CFD simulations in forging the future of the internal combustion engines. In the following sections, the literature related to all the aforementioned important factors -which shape the engine's overall performance-, and the effects of CFD simulations on each one of them will be reviewed.

2.1 Reed Valve Simulation

One of the most important factors in working characteristics of any engine is fuel control. This factor directly affects the engine performance, fuel efficiency, and emission production [1]. It can be seen in Figure 2.1 how changing AFR can affect the emission production of the engine. Based on this graph, which is for a small two-stroke engine, the following can be concluded:

- HC emissions decrease with increasing AFR.
- CO2 production increases moving from rich mixtures toward lean mixtures, and then decreases.
- CO emissions are high when the mixture is rich, and then with the mixture moving to the lean side (higher AFR) CO production is nearly zero.

- NO production is low with rich mixtures; it gradually increases with increasing AFR, and then after the mixture passes a certain lean point, it starts decreasing again.

Based on these observations, it can be concluded that AFR can significantly affect the combustion characteristics and emission production of an engine.

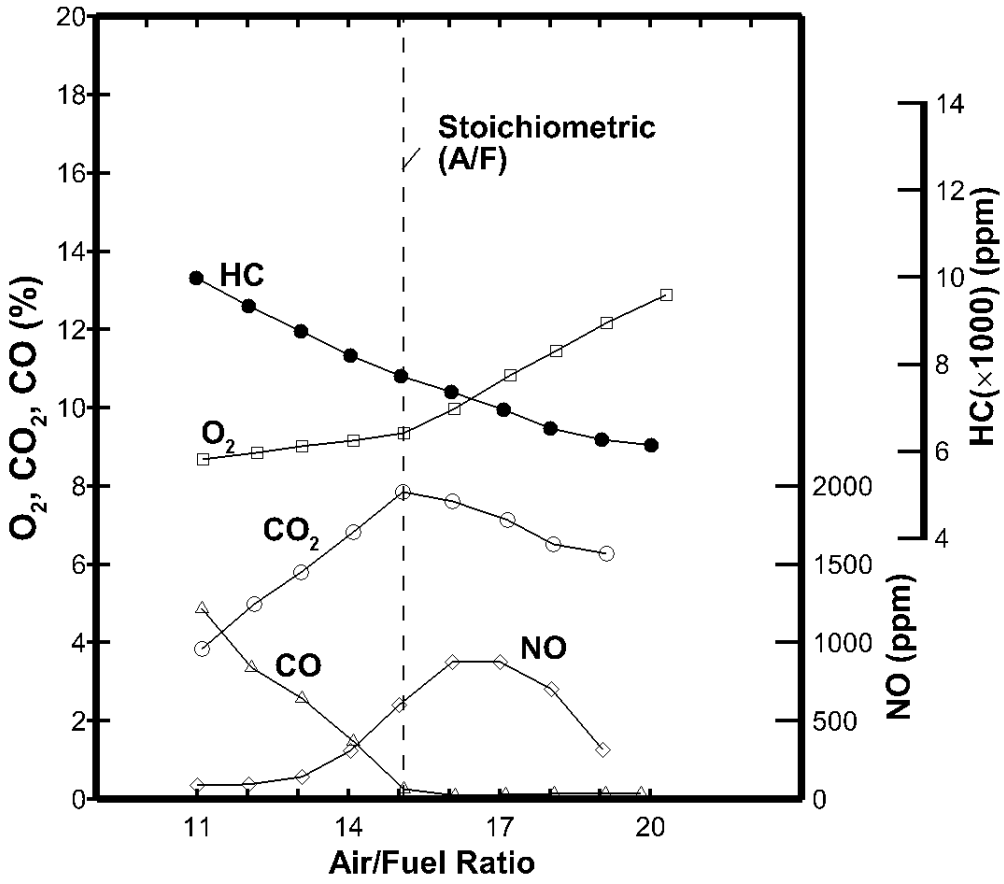

Figure 2.1: Effects of AFR on CO, CO2, HC, and NO emissions in dry exhaust gas from a small two-stroke SI engine (regenerated from [1])

As mentioned above, in this engine, the reed valve is responsible for controlling air fuel ratio; hence, it is very important to simulate this part properly. Numerical simulation of the

reed valves has been thoroughly studied. In 1978, Hinds and Blair [13] developed a model for cantilever type reed valves, which considered the petals as simple clamped beams. For this model, the differential equations of motion for a spring-mass-damping system was solved, to find the displacement for all the points on a petal. A year later, Blair, Hinds, and Fleck [14] used their method to simulate two reed valves. They concluded that their method is capable of simulating the reed valve. Looking at the results presented in these two papers, shows that although their model is capable of predicting the behavior of the reed valve petals, the displacement of the petals, and the downstream pressure simulation are not matching the experimental data very closely.

A few years later, they improved their model. Fleck, Blair, and Houston [15] in their improved model, considered the reed petal material, as well as the reed width profiles. Much better results were acquired using this improved model, but the results were not yet perfectly matching the experimental data.

A different approach to simulating the reed valve was suggested by Mitianiec, and Bogusz in 1996 [16]. They solved a more complete system of partial differential equations to simulate the forced vibration of the reed petals. They tried validating the simulation results with experimental data, and concluded that simulating the petals as plates rather than beams yields more accurate results.

Cunningham, Kee, and Boyall [17] reported the use of CFD for modeling a two-stroke engine's crankcase flows, with utilizing Hinds and Blair [13], and Fleck et al. [15] models, for prediction of reed petal motion. The average pressure on a plane on the inlet duct, and local pressure behind the petals were used as boundary conditions for the intake and outlet sides, respectively. For validation of the simulation results, they used 1-D simulation of the engine. The piston geometry and the connecting rod were not included in their simulation model; hence, the accuracy of the results were lower than expected. Another conclusion they made was that better boundary conditions on the outlet side are required for results

that are more accurate.

Cunningham, Kee, and Kenny [18] in another CFD simulation study on reed valves, tried to predict the motion of the reed petals. This time, to simplify the simulation, they assumed that the engine has symmetry. They also lumped all the petals into just one, and assumed pin joint, instead of a clamped joint, hence, neglecting the bending of the petals. Through linking the CFD model with a 1-D model, they provided the boundary conditions from CFD calculations to the 1-D model, and calculated the petal tip lift with the mathematical 1-D model. Average pressures from CFD simulations were used for both sides of the petals, in the 1-D simulation. At the intake, they assumed constant atmospheric pressure, which corresponds to wide-open-throttle situation. They then validated the CFD simulation results with the results of a proven 1-D simulation of the engine. They concluded that the inaccuracy in the results could most probably be attributed to pulsations in the inlet manifold, which were not considered in the CFD simulations, unlike the 1-D simulations. They suggested that predicting the intake flow fluctuations, could improve the results; this can be done by adding the inlet tract.

Matos, Prata, and Deschamps [19] assuming incompressible flow, simulated the body dynamics of a reed valve in a reciprocating compressor. For simplification, they also used a simple periodic flow rate, rather than the actual flow rate in the compressor. The complex interactions between the gas flow through the valve, and the reed dynamics were included in both physical and mathematical models used for this simulation. Their conclusion was that flow rate should be calculated as a function of ΔP between the upstream, and the downstream of the valve. In addition, to improve the accuracy of the simulation work, they suggested that the compressibility of the gases be considered.

Zeng et al. [20] extended the CFD code, KIVA, to develop a crankcase model that dynamically predicts the crankcase pressure. They also used the model proposed by Blair, Hinds, and Fleck [14] to simulate the flow through the reed valve. Since they included all

the intake and exhaust tracts, they no longer needed dynamic boundary conditions. They then compared the simulation results with experimental data for a single-cylinder engine; the exhaust pressure profiles showed an acceptable match. In the next step, they used the code for a twin-cylinder engine with a folded exhaust manifold. Again, the results showed acceptable resemblance to the experimental data. They later used the simulation results to optimize a production engine.

Battistoni et al. [21] simulated the deformation of the reed petals in a 150 cc engine, by coupling finite element methods, and 1-D pressure simulations. They calculated the effective area of the reed valve, and assumed that the valve works as a nozzle, with that calculated effective area. They then validated the simulated pressure at, a point after the reed valve, with experimental data, and showed good agreement. Through their results they showed that simulating the downstream pressure is not nearly as sensitive as simulating the flow rate through the reed valve.

Rothbauer et al. [22] studied two different methods of simulating the reed valve: 1) spring-damping system, and 2) bending beam model. To acquire validation data, they used a high-speed camera, and measured the displacement of the reed petals; they then compared the results of both methods, with the experimental data. They concluded that the numerical results are acceptable for the purpose of predictive simulation. Through their simulation results, it can be inferred that using pressure curves of the upstream of the valve, could significantly improve the simulation results; these pressure curves can be acquired experimentally, or through 1-D simulations.

Govindan, Venkatesan, and Ramasamy [23] developed a mathematical model capable of simulating a reed valve reciprocating air compressor. This reed valve, which is being used in braking system of heavy passenger vehicles and trucks, is a plate type. Experimental cylinder pressure was used to validate the simulation results. The fluctuations of pressure, during suction and discharge processes, and the fluttering behavior of the plate

was observed in their simulation models.

Jajcevic et al. [24] utilized Blair's 2-D model with CFD tools, and simulated a reed valve. In this study, the injection and combustion processes were not simulated. Results of previous simulations, and/or experimental data were used to initialize the simulation domain every time. In the end, the simulation results were validated with experimental crankcase pressure; the results showed good correlation.

Gonzalez, et al. [25], used FSI (fluid structure interaction) methods to simulate the flow of an incompressible gas through reed valves with typical use in reciprocating compressors. In this study, a LES based CFD solver was used for modeling the turbulent flow. They have presented some of the numerical results, but unfortunately, no validation has been done with experimental data.

In summary, it appears that the most accurate results come from the models, which simulated the body dynamics of the reed valve. The significant effect of setting proper boundary conditions (from 1-D Simulation results, or experimental data) on the results is obvious throughout these studies. However, the simulation of the body dynamics, adds to the complexity of the models, which inevitably will increase the CFD simulation run time.

2.2 Scavenging Simulation

The process of scavenging the burnt gases from the combustion chamber with fresh charge is present in all two-stroke cycle engines, and has several consequences. The first issue with this process is that a big portion of the fresh charge will be vented out through the exhaust manifold during the scavenging. This phenomenon is called short-circuiting, and for a typical two-stroke engine, can be as high as 20% of the fresh charge. In premixed two-stroke engines, where fuel and air are mixed in the stuffing box (crankcase in some cases), and both enter the combustion chamber during the scavenging process, the short-circuiting makes up for almost all the UHC (unburnt hydrocarbon) emissions. This

significantly reduces the fuel economy of theses engines [1].

From as early as 1985, researchers such as Sweeney et al [26] have been trying to look into the details of the scavenging process, through numerical simulations. They used a 3-D computational fluid dynamics program, to simulate the scavenging process of a loop-scavenged two-stroke engine. In this study, they only considered the flow inside the combustion chamber. They carried out the simulation for five different engines, and ranked the engines based on their scavenging efficiency. They then compared this ranking, with the ranking acquired by testing all these engines in an experimental rig, and stated that the numerical simulation shows good agreement with the experimental data. They concluded that in order to improve the results of this numerical simulation, better boundary conditions, and validation data is required.

Smyth, Kenny, and Blair [27] performed an experimental and numerical study, on a loop-scavenged two-stroke engine, because they deemed a detailed knowledge of the scavenging port flow is essential. They used a laser Doppler anemometer (LDA), to do measurements both in the cylinder, and the ports. They then reported the results as Scavenging Efficiency-Scavenging Ratio characteristics, and presented measurements of the mass flow rate as functions of pressure drop across the ports, for different port openings. Through the experimental study, they showed that the flow does not enter the cylinder in the design direction of the port for any port opening. They then ran simulations, with either experimental velocity boundary conditions, or the assumption of plug flow in the design direction of the ports. Comparison of the results showed that the assumption of the plug flow predicts much lower short-circuiting, thus is not acceptable. This means that either measured velocity boundary conditions, or a complete simulation of the flow entering the cylinder through the ports is necessary to get acceptable results with CFD simulations. Although their simulation results were not matching the experimental data that closely, they concluded that the use of CFD simulations as a design tool for two-stroke engines is

justifiable.

In 1990, Sher [28] published a review of all the work done for 30 years to experimentally and numerically evaluate the success of the scavenging process. In this paper, he stated that the scavenging process is the most important factor that controls the efficiency, and the performance of two-stroke engines. In the review of the numerical models, he first cited the one-phase models, which assume that: 1) the scavenging process happens in a constant volume and pressure inside the cylinder; 2) fresh charges will push the burnt gases out by a perfect displacement mechanism, while entering the combustion chamber; 3) fresh charge, and the burnt gases do not exchange any heat or mass; and 4) that the cylinder walls are adiabatic. He then concluded that while the one-phase models are very simple to use, they are not realistic. To solve this issue, researchers then looked into multi-zone models to simulate the scavenging process. For these models, three phases are assumed: 1) displacement, 2) mixing, and 3) short-circuiting. The chamber is subdivided into zones, each of which contains either fresh charge, or a mixture of the fresh charge and the burnt gases, or just the brunt gases. For this model, the following assumptions are made: 1) uniformity of the in-cylinder pressure; 2) dependency of the temperature to the zone, but uniformity of it within one zone; and 3) no heat exchange between the zones. He then extracted the conclusion that while these multi-zone models are much more accurate than the one-phase models, they still are not very realistic, since assuming definite phases is erroneous. He then discussed some of the very early CFD simulation models as "hydrodynamic models", and suggested that the complexity of the scavenging process requires these sophisticated tools to capture all the details of this process. These models are capable of solving the complete set of the differential equations (conservation laws of mass, energy, and momentum), which govern the scavenging process. In addition, he concluded that these CFD models could be used for optimizing the geometry of the cylinder, and the ports.

Sher et al. [29] presented a numerical and experimental study on a steady uniflow-scavenged two-stroke engine. They used a very simple engine geometry, to make the study less complicated. For the experimental study, they used a hot-wire anemometry technique, to measure the three orthogonal components of the average velocity, and the turbulent intensity at 28 different points inside the chamber. For the numerical investigation, they modified a CFD code, and solved the differential equations. They concluded that the getting extremely good agreement between numerical and experimental results is very difficult, even for a relatively simple geometry. They suggested that a more accurate turbulent model might help getting numerical results, which are more reliable.

Lai, Przekwas, and Sun [30] numerically simulated the scavenging flow process of a motored two-stroke engine. For this study, they divided the geometry into six computational domains: cylinder, engine dome, exhaust, and transfer ports. They also studied the effects of the inclination of the boost port angle on the scavenging process. For simulating the turbulence, a two-equation turbulence model was used; the equation was corrected to consider the compressibility of the gases. They concluded that the scavenging flow is significantly sensitive to the geometry of the ports, and the upstream pressure. They also concluded that the transient nature of these turbulent flows requires the simulation of the whole geometry, including the ports, and manifolds; they ruled that isolated simulation of the chamber would not be accurate and acceptable. They argued that the CFD simulations are capable of being used to provide detailed flow field information.

Dekanski, Bloor, and Wilson [31] tried a numerical method, to optimize the geometry of a two-stroke engine. In their work, the elements of the internal geometry of the engine were represented by partial differential equation, and the flow inside the engine was simulated by CFD methods. They used a code, based on finite volume methods, and used a $k-\varepsilon$ model to simulate the turbulence. They have not done any validation attempts for the simulation work. They were trying to prototype the optimized design, and run experiments

on it to validate the simulation results later.

Raghunathan and Kenny [32] used a STAR-CD CFD code to simulate a loop-scavenged two-stroke engine under motoring condition. This code uses a multi-block approach to simulate the flow in different parts of the geometry. They then compared the simulation results with experimental data (velocity field) acquired before. They mentioned in the results that the in-cylinder flow is significantly sensitive to reverse flow from the exhaust manifold at EPO. Their simulation results shows a complex structure for the in-cylinder flows, majorly consisting of recirculating flow features. The comparison of the numerical simulations results and the experimental data revealed that the CFD code is capable of capturing the large-scale flow structures, and the global flow properties. On the other hand, they concluded that the numerical results do not capture the detailed flow characteristics. They mentioned that the simulation results were not accurate enough during the open-port phases of the cycle, and attributed the inaccuracy to low mesh density around the ports.

McElligott et al. [33] used the CFD code VECTIS to simulate a stratified scavenging process in a two-stroke engine. The goal of their work was to reduce exhaust emissions. They ran experiments on the same engine to acquire validation data for the numerical study. The CFD results showed good correlation with the experimental data. The results of the CFD simulations were interesting because they were able to provide detailed insight into the flow behavior inside the cylinder. They then used the CFD code, to test different cylinder geometries, to investigate possible improvements in trapping efficiency.

Payri et al. [34] coupled a 1-D model with CFD simulations, to simulate the scavenging process of a small two-stroke engine, trying to optimize the geometry. The results of the 1-D simulation were used as boundary conditions for the CFD code. The port geometries were built by parametric design, letting the researchers change the geometry with ease, and test the effects of the geometry on the scavenging process.

Benajes et al. [35] analyzed the combustion process, emissions, and the efficiency of

a newly designed two-stroke HSDI (high-speed direct injection) engine. As a part of their study, they looked into effects of the scavenging process, and the mixing in the cylinder, on the combustion characteristics, exhaust emission levels, and the engine efficiency. This study, although purely experimental, showed how important the scavenging process is on the combustion efficiency, and the emissions production of two-stroke engines. The trapping efficiency of the engine was shown to have significant effects on the NO_x emissions. The mixing characteristics on the other hand, were shown to influence the soot production.

In two-stroke engines, short-circuiting is the main reason for having high levels of UHC emissions. Garg et al. [36] used a CFD model to simulate a small two-stroke loop-scavenged engine, in an attempt to understand the short-circuiting phenomenon. They used STAR-CD for the CFD modeling of the engine, and simulated the expansion, scavenging, and the compression processes. They then used a PIV measurement in motoring conditions to validate the simulation results. Experimental in-cylinder pressure, and experimentally measured trapping efficiency were also used as validation criteria. After validating the numerical results, they used the CFD model to calculate the delivery ratio, trapping efficiency, scavenging efficiency, and amount of short-circuiting of the fresh charge, at different load and speed conditions. The numerical results showed that the engine has 20-25% short-circuiting in all speed-load conditions, and the culprits were decided to be the port design, and the wave dynamics of the exhaust pressure. They then ran simulations for three different port designs, and showed that for this engine, an optimized port is capable of reducing the short-circuiting by 12%. They then experimentally tested the same optimized port design, and showed 10% reduction in UHC emissions.

Overall, it can be established from the literature that the proper simulation of the scavenging process in two-stroke engines is very important.

2.3 Combustion Simulation

In 1981, Butler et al. [5] published a review of all the numerical methods available at the time, capable of simulating multi-dimensional chemically reactive fluid flows in internal combustion engines. The importance of the combustion simulation is discussed, and then a list of researchers and institutes who have done work on the numerical simulation of the combustion process are presented.

Kong, Han, and Reitz [6] used a CFD code to simulate a diesel engine. For the combustion phase of the simulation, they used a multi-step kinetics model, and a combustion and ignition model, which were switched at 1000 K. The ignition model was used in locations with temperatures below 1000 K, and the combustion model for places with higher than a 1000 K temperature. Extended Zel'dovich mechanism was used to describe the NO formation. The numerical results showed good correlation with the experimental data.

Reitz and Rutland [37] developed and validated a CFD model for diesel engines. This model is capable of simulating the combustion, and calculating the emission production. They used a modified version of the KIVA code for the computations, and done some modifications to the sub-models to improve the results. For the combustion process, they used multi-step kinetics ignition, and laminar-turbulent characteristic time combustion models, Zel'dovich NO formation, and soot formation. They reported on using a modified $RNG\ k-\varepsilon$ model for turbulence modeling, with significantly improved results. They then ran experiments on a single-cylinder version of a heavy-duty truck, and validated the simulation results with the experimental data. They reported that the combustion performance is significantly affected by intake flow process. The comparison between the CFD results, and the experimental data showed a generally good agreement between the in-cylinder pressure, heat release, soot and NO_x emissions prediction, and the combustion visualization.

In 1999, Jasak et al. [38], with concerns about the long simulation time for internal combustion engines, tried to develop models to the end goal of rapid CFD simulations. They briefly presented some of the combustion calculation results, and showed that using finer grids could result into prediction of the combustion inside the cylinder that are more accurate. This of course, requires parallelization capabilities of the CFD code, to speed up the simulation, and reduce overall simulation run-time.

Senecal [39] in his dissertation, discusses a new methodology for optimization of internal combustion engines, using multi-dimensional modeling. Simulating the combustion inside the cylinder is a part of his research; the combustion model used for CFD simulations of a diesel engine is discussed in detail in this dissertation. A comparison between numerical simulation results and experimental data is done; in-cylinder pressure, and emission production, show close correlations. The numerical model is then used with a genetic algorithm optimization method, to find the best design characteristics for the simulated engine, to achieve reduced emissions production, and improved performance.

Kong and Reitz [40] implemented a detailed chemical kinetics mechanism into KIVA-3V CFD code, to simulate the combustion and emissions of a HCCI engine. They started the simulations from IPC (intake port closure), and used the results of a 1-D simulation, capable of gas-exchange process simulation, as initial conditions. The simulation results were validated with experimental data; close agreement between in-cylinder pressure and heat-release rates were achieved. The inclusion of effects of turbulent mixing on reaction rates, made the prediction of combustion phasing possible. The simulation results showed that the concentrations of UHC and CO are higher near the walls.

Drake, Fansler, and Lippert [41] used CFD methods to model a spray-guided direct-injection spark-ignition (SG-SIDI) gasoline engine. They used high-speed spectrally resolved combustion luminosity imaging, and in-cylinder pressure measurements as validation data. The CFD calculations were done using GMTEC, which solves for momentum,

energy, and species concentration equations. The boundary conditions for the CFD code were obtained from a 1-D simulation work on the engine. The simulation was divided into two parts: 1) the open portion, and 2) the close portion. The open portion uses a courser grid to simulate the induction flow faster; the results are then mapped to a finer grid after the intake valves are closed, and the close portion simulation starts with the finer grid size. The spark plug was not included in the simulation domain; instead, the ignition was imposed on the cells, by a burn rate at the ignition timing. From both numerical and experimental studies, they concluded that for a fixed injection timing, an earlier ignition timing would increase rich burning. The simulated and measured heat-release rates showed good agreement for different engine operating conditions. They claim that the detailed knowledge acquired through this numerical simulation work, could be used as a basis for engine design optimization.

Cheng and Wallace [42] used CFD models, to simulate the ignition and combustion for a glow plug assisted DI natural gas engine. In the numerical study, the swirl ratio inside the combustion chamber was set manually as an initial condition. The simulation work included both un-shielded and shielded glow plugs. The results of the former were compared with experimental data, and showed very good agreement. The conclusion was that the shielded glow plug performs much better than the un-shielded version. The work again emphasizes the ability of the numerical simulations to capture details of ignition and combustion.

Yang, Solomon, and Kuo [43] used n Arrhenius combustion model in the CONVERGE CFD software, to simulate ignition and combustion in a SG-SIDI engine. To simulate the spark event, they used an energy deposition model, allowing the spherical ignition source to move. They validated the simulation results, with experimental data acquired from a single-cylinder SG-SIDI engine with both single and double-pulse fuel injections, at idle-like lean-burn operating conditions. They mentioned that a very fine mesh (≈ 0.125 mm) is

required to capture the flame front development properly. They also studied the effects of advanced spark timing numerically and experimentally, and concluded that the simulation is capable of providing reasonable predictions for this engine.

Wang et al. [44] used a 1-D GT-Power code to provide initial and boundary conditions for a CFD simulation of a light-duty spark ignition (SI) gasoline direct injection (GDI) engine. The CFD simulation is carried out using CONVERGE CFD. This engine has a dual-fuel combustion system; hence, three combustion modes are being used, based on the engine load:1) at high load conditions, a diesel micro-pilot (DMP) mode, 2) at low loads spark-ignition combustion, and 3) in the transition zone, diesel assisted spark-ignition (DASI) combustion are used. The main focus of the paper is the DMP mode simulation. The optimization of the main parameters of the engine is the final goal of this study. For the combustion simulation, a dual-fuel chemical kinetics mechanism was used; this mechanism consists of 43 species, and 78 reactions. The numerical simulation results were validated with experimental data (rate of heat release, and in-cylinder pressure) for various operating conditions. The concluded that the CFD simulation is capable of accurately predicting the combustion, in all tested operating conditions. In addition, the mentioned that the combustion process is sensitive to parameters, like intake temperature, EGR rate, injection pressure and timing, etc. The CFD was used to assess the influence of each of these parameters on the combustion.

Raju et al. [45] implemented multi-zone model in CONVERGE CFD code, with the goal to speed up the simulation of the combustion process. It is known, that while detailed chemical reaction mechanisms are preferred for their added accuracy, they could reduce the simulation speed significantly, up to the point that the combustion simulation is the most time-consuming part of any engine simulation. The multi-zone model has the potential to reduce the combustion simulation time significantly. In this method, cells with similar temperature and equivalence ratio are grouped into zones. The calculations are

done within the zones, and then the calculated temperature and mass fractions of the zones are re-mapped into the CFD cells, in a way that preserves the temperature and composition non-uniformities. They then compared the multi-zone-enabled simulation results, with detailed chemical reaction mechanism simulation results, for two different cases, and showed good correlation; while saving ≈90% simulation time.

Etcheverry, Patterson, and Grauer [46] used CONVERGE CFD to simulate a re-designed large bore natural gas engine with high pressure fuel injection and electronic prechamber fuel control. The goal of the simulation was to assess the effects of the engine modification on the emissions production of the engine, and to confirm the reduction in the emissions prior to manufacturing the re-designed engine. They compared the simulated in-cylinder pressure with experimental data, and confirmed the accuracy of the models. Then they looked into exhaust emission levels, and compared the results of the re-designed engine, with the baseline results. The simulations confirmed significant reduction in both CO and NO_x emissions; in addition, UHC emissions were reduced by approximately 70%. They concluded that the CFD tools are invaluable tools at engineers' disposal, which could be used for analyzing new designs.

In another study, Etcheverry, Patterson, and Grauer [47] used multi-dimensional numerical simulations, to re-design another large bore two-stroke natural gas engine, with the goal to reduce the emission production of the engine. This naturally aspirated, crankcase-scavenged, horizontal engine was simulated using CONVERGE CFD. Experimental in-cylinder pressure was used as validation criterion for the simulation data. They then used the simulation results of the combustion, in another CFD package to simulate the conjugate heat transfer inside the prechamber, and looked into thermal stresses on the walls of the prechamber. These results could be used to improve the design of the prechambers for these engines. In the conclusions, they emphasized the potential of CFD tools for virtual design and analysis of engines.

Givler et al. [48] used CONVERGE CFD to test a reduced chemical reaction mechanism for gasoline combustion modeling. They started from the detailed Primary Reference Fuel (PRF) mechanism with 1034 species and 4236 reactions from Lawrence Livermore National Laboratory (LLNL), and reduced the mechanism for two different scenarios. A high-pressure (20-50 bar) mechanism with 123 species and 502 reactions, and a low-pressure (2-10 bar) mechanism with 110 species and 488 reactions. They then coupled the mechanisms with multi-zone chemistry solver, and simulated gasoline combustion for various engine conditions. Two engines were tested in this study: a Turbo-charged Direct Injection (TCDI) engine, and a Port-Fuel Injected (PFI) engine with Charge Motion Control Valve (CMCV). They then presented the results of the simulation work, compared the simulated in-cylinder pressure with different reaction mechanisms with experimental data, and showed acceptable correlations. This shows that the CFD simulation is capable of predictive studies, and the details of the combustion process could be captured using these numerical tools.

The great potential of the CFD simulations in predictive study of combustion in internal combustion engines have been established through literature review.

2.4 Conjugate Heat Transfer Simulation

It is well known that the heat transfer information in internal combustion engines is very important, for multiple reasons; the heat transfer influences the engine efficiency, and significantly affects the emissions production. Experimental studies to evaluate the heat transfer in CI and SI engines have been done thoroughly over the past decades; one of these studies was done by Alkidas [49] on characterizing the heat transfer in a four-stroke spark-ignition engine. In this study, he modified an eight-cylinder engine to operate on one cylinder, and modified the cylinder head to insert four heat flux probes in different location on the head. He then recorded the crank angle resolved surface heat flux for both

motoring and firing conditions, for different engine speeds and spark timings. He found out that the heat flux significantly is dependent on the location of the measurement. In addition, the results showed that the peak heat flux increases for higher engine speeds.

Two years later, Alkidas and Myers [50] used the same test apparatus as [49] to assess the effects of AFR and volumetric efficiency on the heat flux. They showed that the heat flux is higher for near-stoichiometric mixtures, and is lower for both lean and rich mixtures. They also presented the results that showed a 30% increase in heat flux, with a 20% increase in volumetric efficiency. They then measured the heat transfer to the walls in the closed portion of the cycle, and showed that the results match with calculations from the heat flux measurements.

Later, numerical modeling of the wall heat transfers started. Angelberger, poinsot, and Delhay [51], in 1997, developed a model from direct numerical simulation results, which could be implemented in CFD solvers. This model could estimate the mean heat loss through combustion chamber walls; thus, improve the numerical simulation of the spark-ignited engines, by modeling the flame quenching at the walls due to wall heat transfer.

Xin et al. [2] proposed a method to integrate the combustion simulation, with conjugate heat transfer analysis. The goal of their work was to be able to evaluate the temperature of different components of the engine quantitatively. It is known, and they mention that the temperature distribution is too non-uniform on the chamber walls to be assumed uniform for the CFD simulations; hence, the results will not be accurate with the latter assumption. With their proposition, they offer a way to reduce the errors associated with the uniform temperature distribution assumption. For the CFD simulation of the combustion, they used commercial KIVA-3V code. The flowchart of their integrated analysis method is presented in Figure 2.2.

For the simulation work, they included the cylinder head, head gasket, cylinder block, and cylinder liners, and the coolant passage through these parts. They only considered one

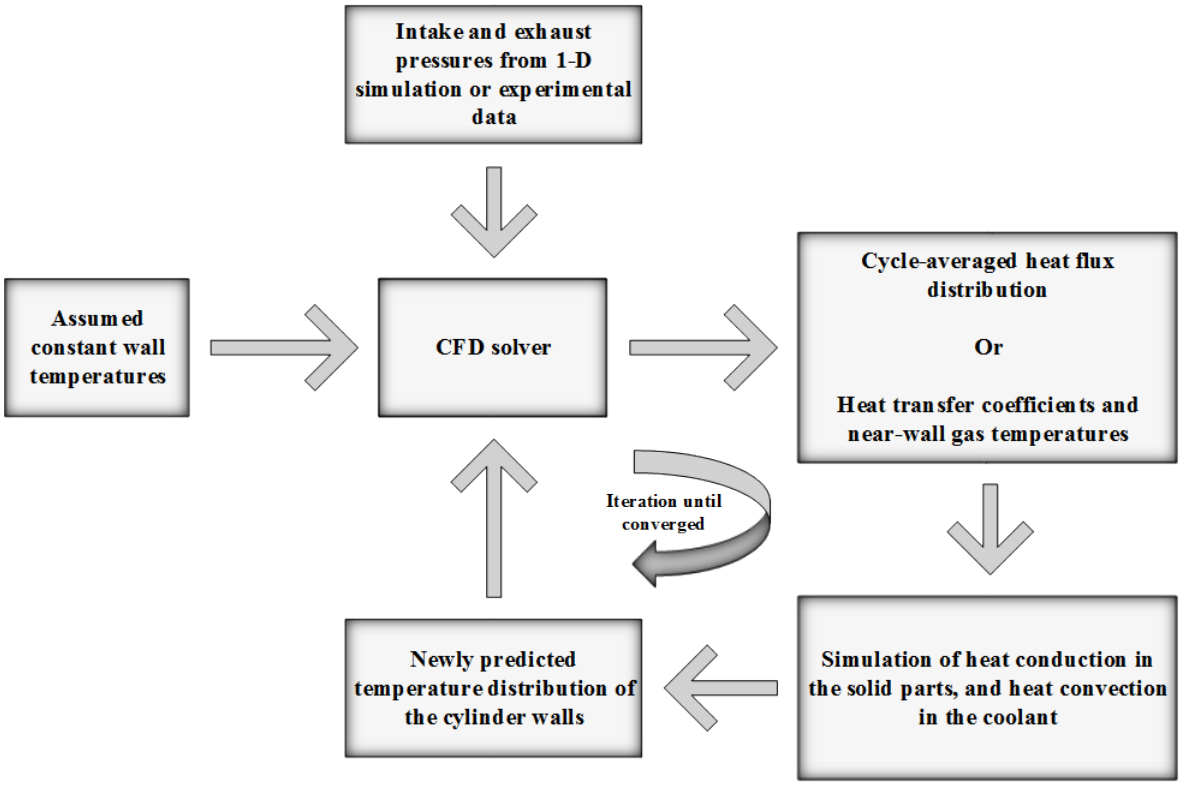

Figure 2.2: Flowchart of the integrated analysis method proposed by Xin et al. (regenerated from [2])

bank of a V6 engine for this study. It should be noted that in their simulation of the coolant flow, the phase change was not considered. The combustion simulation was first validated with experimental in-cylinder pressure data; while the results were not perfect matches, they were acceptable enough for the purpose of temperature prediction. The simulated spatial heat flux values from this step were mapped to the walls for the conjugate heat transfer simulation. The resulting temperature distribution was then used as boundary condition for the CFD simulation. The iteration process continued until both simulations converged.

Baniasad, Khalil, and Shen [52] reported on using an in-house developed 1-D two-zone combustion model, to provide boundary conditions (such as crank angle resolved

combustion flame propagation, burnt/unburnt gas temperatures, and heat transfer coefficients) for 3-D conjugate heat transfer simulations. This 1-D model was first validated against experimental data. The model could be calibrated for different engine load and speed conditions. For the conjugate heat transfer simulation with commercial software STAR-CD, a nucleate boiling model was considered for the coolant flow, to increase the accuracy of the simulation results. The maximum temperature through the exhaust valve was then calculated using the 3-D simulation code, and the results were validated against experimental data; the simulation results show good correlations with the experiments.

Esfahanian, Javaheri, and Ghaffarpour [53] coupled KIVA-3V and NASTRAN commercial software packages to do a thermal analysis of a piston in a spark-ignition internal combustion engine. The 3-D simulation results of the combustion inside the cylinder were used as boundary conditions for the calculation of heat conduction through the piston body. As the temperature distribution on the piston crown is one of the boundary conditions for the combustion simulations, an iterative method has been used to get results for both simulations that are more accurate. To analyze the effects of combustion boundary condition on the conjugate heat transfer study, the authors ran the CHT simulation with 3 different combustion boundary conditions: 1) surface and cycle averaged values for the gas heat flux at the piston top surface; 2) locally cycle averaged values for the gas heat flux at the piston top surface; and 3) fully locally transient values for the gas heat flux at the piston top surface. They concluded that the third method is the most accurate, and the most time-consuming; the first method is the less accurate, and the fastest; and the second method is in between.

Urip, Liew, and Yang [54] used KIVA-3V to simulate the in-cylinder flow and combustion of a 5.4-L V8 engine, and modified the code to also simulate the conjugate heat transfer of the solid parts. At the gas-solid interface, they added pyramid, prism, or hexahedron elements to transmit the data from the fluid simulation domain to the solid simulation

domain. Unlike the previous studies covered in this chapter, this study couples the gas-phase simulation with the solid-phase simulation throughout the whole engine simulation cycle. It should be mentioned that the authors state that this method would require several simulation cycles to get to periodic steady-state temperature distribution for the solid domain, as opposed to the fluid domain, which will reach periodic steady-state, within two or three simulation cycles; hence, this method will be much more numerically expensive than the previously mentioned methods.

In another study, Urip and Yang [55] used the simpler method of iterating between gas flow and combustion simulation, and conjugate heat transfer to calculate the temperature distribution on the walls of one cylinder of a truck engine. KIVA code was used for the gas flow and combustion simulations, and FLUENT was used for the coolant flow and conjugate heat transfer simulation. They ran the simulations two different ways: 1) steady-state, and 2) periodic steady-state. The results showed that the difference between the two solutions is minimal, thus, the additional complexity associated with the second method is not justifiable.

Fontanesi, and McAssey [56] reported on an experimental and numerical study, focused on improving the accuracy of CHT simulations. For this purpose, they compared the experimental data (temperatures at different points, and heat fluxes) acquired from a very simple electrically heated horizontal aluminum channel supplied with constant volumetric flow rate coolant, with numerical results. They then used several different turbulence and boiling models in the numerical simulation, to analyze the effects of these models on the accuracy of the results. They concluded that the simplified boiling models are not capable of accurate predictions. The validation process proved that the v2-f model provides the most accurate results, with reasonable additional computational cost. They then applied this model to a 3L HSDI diesel engine to predict the temperature distribution within the cylinder head, and the cylinder block.

In another study, Fontanesi, Cicalese, and Giacopini [57] simulated the conjugate heat transfer of a V6 turbocharged diesel engine, to analyze and optimize the engine's water cooling jackets. For this purpose, a full CFD and FEM analysis of the engine under actual engine operation conditions was carried out. Boundary conditions were set from a combination of experimental measurements, and 1-D models of the engine. The CFD simulation setup was calibrated and then validated by experimental temperature distribution within the cylinder head at eight different points. The phase transition and vapor formations models were also included in the numerical simulation. In addition, design optimization of the engine to improve fatigue strength was addressed. The numerically simulated temperature distribution correlates very well with the experimental data; in addition, the locations on the engine that were predicted by the numerical simulation to be susceptible to fatigue failure, were very close to the experimentally marked points.

Fontanesi, Cicalese, D'Adamo, and Pivetti [58] looked into the effects of setting proper boundary conditions, and detailed representation of the physical properties of the materials on the conjugate heat transfer simulation results of a V8 high-performance SI engine, separately. In addition, the effects of simplifying assumption of single-phase coolant, versus two-phase coolant was assessed. The numerical simulation results were validated with experimental temperature measurements in the cylinder head. The results emphasized the importance of considering the entire cooling circuit in the simulations. In addition, importance of proper boundary conditions for the CHT simulation was concluded. The authors suggested that the use of two-phase models for the coolant is not necessary, and due to the added complexity, should be avoided, unless a very critical thermo-mechanical study is being carried out.

Li and Kong [59] fully coupled the calculations of the fluid flow and the transient heat conduction in the solid components (cylinder head, and the piston crown), for a diesel engine. To validate the model, a simple simulation in a slab was compared with the ana-

lytical calculations. The model was then applied to a section of the engine's combustion chamber, and the solid parts. The results show that the model is capable of predicting the temperature distribution on the combustion chamber surfaces. It is evident that the wall temperatures change almost 100 K within one cycle of the engine, due to the transient nature of the diesel spray and combustion. This study shows that the use of CHT models does not change the predictions of the global engine combustion and emissions parameters, significantly.

Fontanesi and Giacopini [60] analyzed and optimized the water cooling jacket of a V6 diesel engine, by means of multi-phase CFD-CHT numerical simulations. The goal of the study was to assess the fatigue strength of the cylinder head. They included vapor formation and phase change in the simulation of the coolant, and simulated one bank of the engine. Numerical simulation results were validated by comparing the simulated temperatures at a few different points with experimental data. A thermo-mechanical study was then carried out to optimize the design of the engine for fatigue strength.

Punekar and Das [61] used CFD tools to simulate and assess the effects of sub-cooled nucleate boiling in the cooling jacket of an internal combustion engine. To simulate the multi-phase flow, momentum, continuity, and energy equations were solved for the mixture; in addition, the volume fraction equations were solved for the secondary phases in ANSYS FLUENT. The capability of the models to capture the effects of changes of the wall temperature under different pressures, and flow velocities on wall heat flux was tested against a very simple experimental work. The model is then applied to just the cylinder head of a single cylinder engine. In the cylinder head, there are three fluid zones (exhaust and intake manifolds, and cooling jacket) and one solid zone. Time-averaged heat flux acquired from combustion simulation was applied as boundary condition for the CHT simulation. Heat transfer enhancement of up to six times were observed in small surfaces were boiling was captured. Looking at the presented results, though, reveals minor

changes in the overall temperature distribution on the cooling jacket walls, between the multi-phase and the single-phase simulations.

In yet another study, Fontanesi et al. [62] integrated the combustion simulation and the conjugate heat transfer of a high performance GDI engine. An iterative approach was taken between the two simulations, until convergence was achieved in both. Combustion and knocking events were recorded. CHT simulation converged after just one loop of the simulation. The combustion simulation was validated via in-cylinder pressure comparison with experimental data. The CHT simulation results predict a higher in-cylinder mixture temperature, compared to the uniform wall temperature simulations, hence, the combustion development is faster with CHT calculated wall temperatures.

Iqbal, Arora, and Sanka [63] coupled CONVERGE CFD and StarCCM+ to map the temperature distribution of an internal combustion engine with conjugate heat transfer simulations. The combustion simulation was done using CONVERGE CFD, while the CHT simulation was done with the StarCCM+. Convective heat transfer coefficient and near-wall gas temperatures from combustion simulation are applied as boundary conditions for the CHT simulation. A Pseudo steady-state boiling model was utilized in the CHT simulation study. Simulation was done for three different operating conditions. A few thermocouples were installed in the engine, and experimental local temperatures were acquired. The numerical simulation results were compared to the experimental data, and acceptable correlation was observed. In higher temperature regions, the numerical data was reported to be within 5% of the experimental temperature.

Jahangirian et al. [64] utilized ANSYS FLUENT to study the conjugate heat transfer of a heavy duty V6 diesel engine. The goal was to do a thermos-mechanical fatigue study on critical parts of the cylinder head for various operating conditions. The simulation results were validated, using 31 thermocouples in different locations of the cylinder head. The measured local temperatures were compared with numerical data for validation of

the CHT results; predicted temperatures, were correlating with the measured temperatures well. They, too, used an iterative method, going back and forth between the combustion simulation, and the CHT simulation until convergence was achieved. The temperature distribution was then imported into a FEM analysis, to assess the fatigue strength of the designed cylinder parts.

Cicalese, Berni, and Fontanesi [65] applied their previously developed method to a turbocharged DISI engine, to evaluate the thermal field of the engine. A modified thermal law was proposed to formulate CHT; a comparison between the results of this modified law and experimental data shows a very good agreement. Regardless of the location of the measurement and the engine speed, the calculated temperatures were usually higher than the measured temperatures. In some conditions the temperatures were very close, and some were between 10 to 60 K higher than the measured values.

Kundu et al. [66] performed CHT simulations on a small diesel engine in order to calculate the heat loss, and then used it to quantify the efficiency gain achieved by using thermal barrier coating on the piston bowl. CONVERGE CFD was used as the numerical tool in this study. A grid-size study was done, and 0.5 mm grid size was shown to be sufficiently fine. The average error in the results compared to experimental temperature measurements is less than 5%. The gain in efficiency and the reduction in heat loss were shown to have an asymptotic behavior with higher thermal resistances. The model also provides the researchers with the temperature distribution in the solid regions; this data could be used to improve the thermos-mechanical design of relevant engine parts.

Overall, it is well established in literature that the numerical simulation tools are capable of predicting the temperature distribution inside the solid parts of any engine, as well as the coolant flow. The results of such simulations were shown to have been used for thermo-mechanical design of engines, analysis of fatigue resistance of solid engine parts, study of local hot spots in the combustion chamber and its effect on knocking, etc. The

potential uses for such information seems to be endless.

3. EXPERIMENTAL STUDY

As reliable as numerical simulations can get, the need for experimental data to validate the numerical results is still inevitable. In order to acquire the needed data, a thorough experimental study was done on an AJAX E-565 at Advanced Engine Research Lab (AERL) at Texas A&M University. In this section the instrumentation of the engine for this study, the experimental procedure, and finally some of experimental results will be presented.

The instrumentation of the engine was done by Mr. Aaron Griffin, a former member of the AERL as presented in his Master's Thesis [67], and Mr. Jeffrey Brown, a current member of the AERL. Experimental work was done with tremendous help from Aaron Griffin, and Jeffrey Brown.

3.1 Test Apparatus

3.1.1 Engine

AJAX E-565 is a single cylinder, two-stroke, large bore, spark-ignited, natural gas engine (Figure 3.1). The important characteristics of the engine are presented in Table 3.1. The details of how a two-stroke cycle engine works will be presented in the NUMERICAL SIMULATION chapter.

3.1.2 Dynamometer

To apply known loads on the engine, a 50 kW eddy current dynamometer is connected to the engine. A potentiometer is used to send a control signal of 0-10 VDC to the dyno to command load. The dyno can be seen to the right side of the engine in Figure 3.2. The dynamometer can be connected/disconnected from the engine by a manual clutch.

Table 3.1: AJAX E-565 natural gas engine specifications [3]

Property	Imperial Units	SI Units
Rated continuous BHP	40 hp	29.8 kW
Rated RPM	525	—
Bore × Stroke	8-1/2" × 10"	216 mm × 254 mm
Piston Displacement	567 in^3	9.29 lit
BMEP	53.6 psi	369.6 kPa
Effective Compression Ratio	6:1	—
Torque	400 ft-lb	542 N·m
Weight (Including flywheel)	4716 lb	2139 kg

3.1.3 Data Acquisition System (DAQ)

The DAQ system was built using NI provided hardware. In order to acquire the experimental data needed for the numerical simulations, the engine was instrumented with a data acquisition system as presented in Figure 3.3. As can be seen in this figure, the DAQ system is capable of providing the in-cylinder pressure, the stuffing box pressure, the intake air, intake fuel, and exhaust pressures, and also the load and temperature of the dyno. The temperatures of the coolant and the wall temperature for the CHT study are acquired separately.

3.1.4 Sensors

Different sensors are used to get the required data from various parts of the engine. In this section, each will be discussed briefly.

In-Cylinder Pressure

A piezoelectric pressure transducer (Figure 3.4 (A)) was used to measure the in-cylinder pressure. Pressure changes on the surface of this transducer's crystal will output a charge, which is proportional to the pressure change. This charge will then pass through a charge amplifier, which transforms the charge into an output voltage signal. This voltage is what

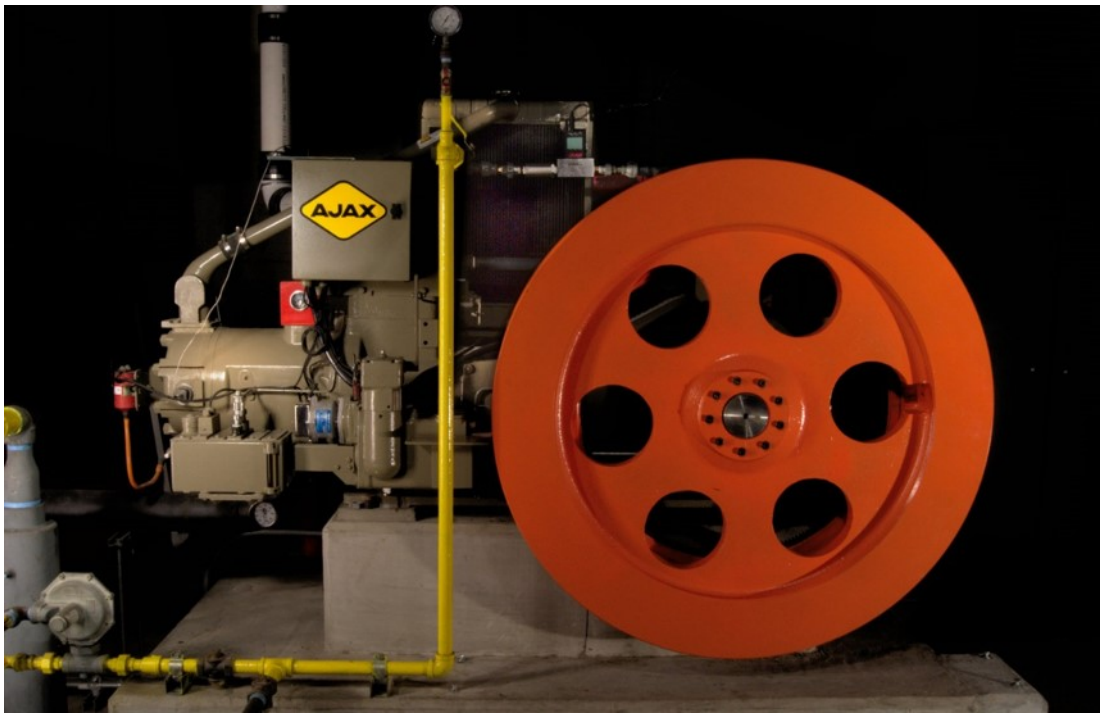

Figure 3.1: AJAX E-565 engine (Image courtesy of Jacob Hedrick)

the DAQ system reads, and translates into pressure data for given gain and offset values, which are set, based on the sensor's calibration. Needless to mention that the transducer is calibrated regularly, based on manufacturer's suggestions.

Stuffing Box Pressure, Exhaust Pressure, and Intake Pressures

A water-cooled piezoresistive absolute pressure sensor (Figure 3.4 (B)) was used for measuring the mentioned pressures. This sensor utilizes a Wheatstone bridge, implanted in a silicon measuring element, which generates an electrical signal proportional to the applied pressure [68]. This sensor has its own in-line amplifier to transduce the charge to a signal, readable by the DAQ system. The measuring range for this transducer is 0 to 5 bars, which is more than the required range for the mentioned pressure readings.

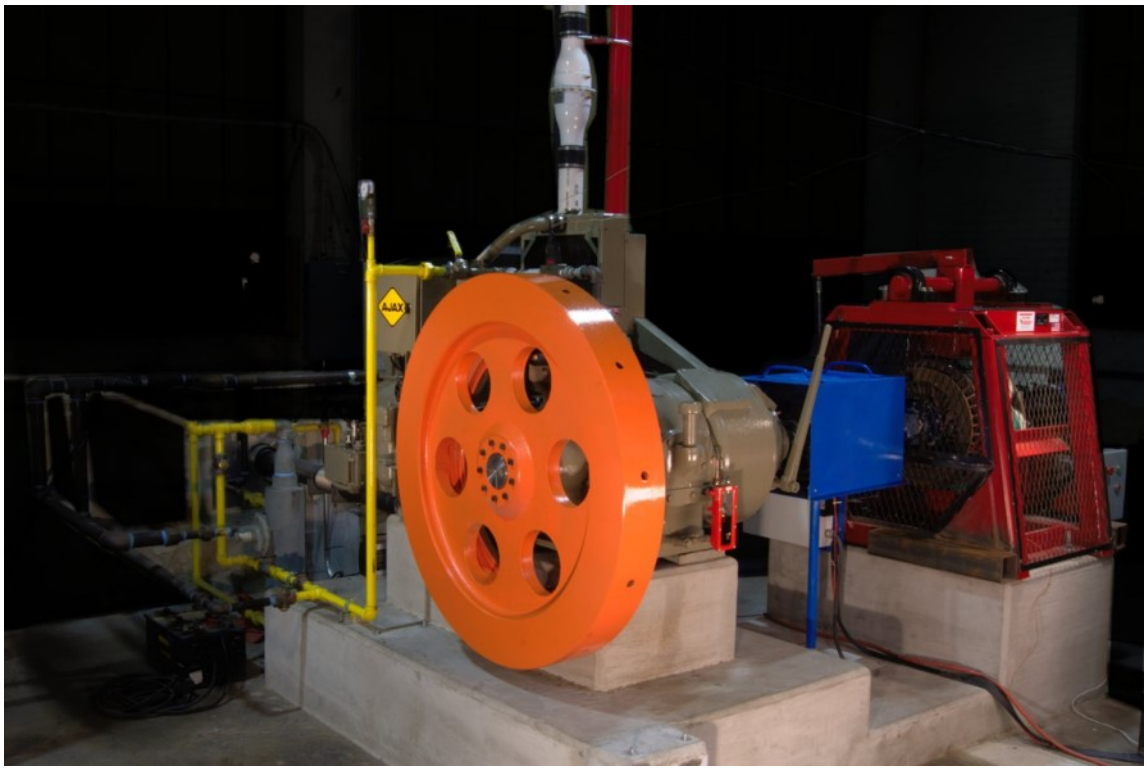

Figure 3.2: AJAX E-565 engine and the eddy current dynamometer (Image courtesy of Jacob Hedrick)

Encoder

Piston position is measured using an optical encoder with 1440 ppr, which can trigger measurements every 0.25 CAD. In order to set the TDC location right on the encoder, motoring curves of the engine were used. Because of the large size of the engine, it is unlikely to be able to motor the engine as done on smaller engines, where it is done with electrical motors. Instead, after getting the engine up to speed, the fuel was quickly cut off, and the spark plug was disabled. The huge inertia of the flywheel will keep the engine running for a long time, decelerating very slowly. This provides enough time to record the in-cylinder pressure data for a few cycles. Without the ignition and combustion events, it can be assumed that the peak pressure will happen at TDC. This way the difference

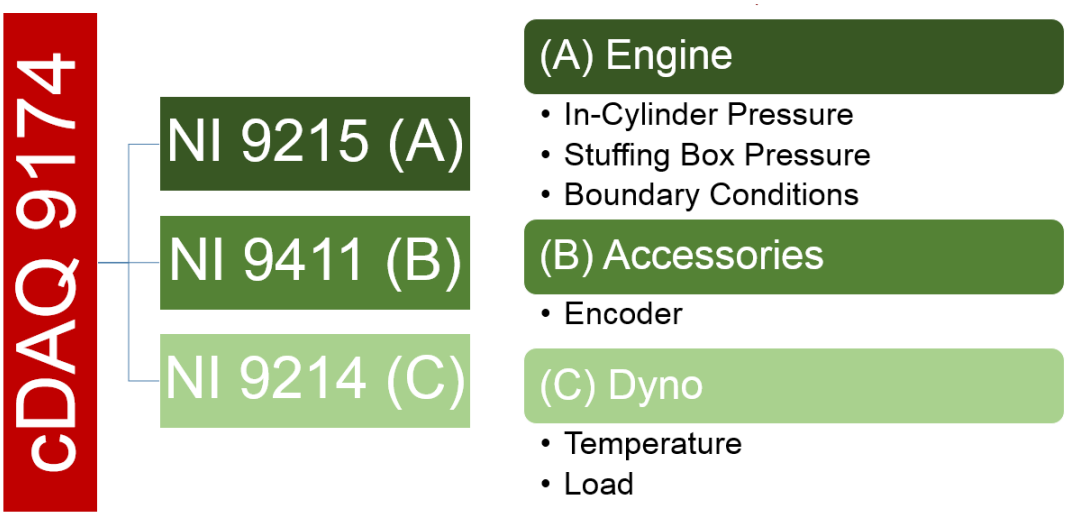

Figure 3.3: Data acquisition system design

between the peak pressure location and TDC can be set as offset of the encoder.

Coolant Flowmeter and Thermocouples

The study on the cooling system of the engine was done by Jeffrey Brown, Tim Kroeger, Srivatsa Chakravarthy, and Yujie Sun, all Masters students at Texas A&M University as a course project [69]. The primary instruments they used for this study were a venturi flowmeter, and multiple thermocouples in different locations of the system. Since the cooling system of the engine does not have a water pump and works solely based on the density gradient throughout the system caused by temperature gradients, the flowmeter should be such that has the lowest possible pressure drop. Additionally, since the flowrate is lower than the lowest range of most types of meters (e.g., turbine meters, etc.), a venturi-type flowmeter was chosen. The flowrate then can be calculated from the pressure differential between the flowmeter pressure taps. The venturi flowmeter can be seen in Figure 3.5.

Another important variable of interest is the temperature. To find the required tem-

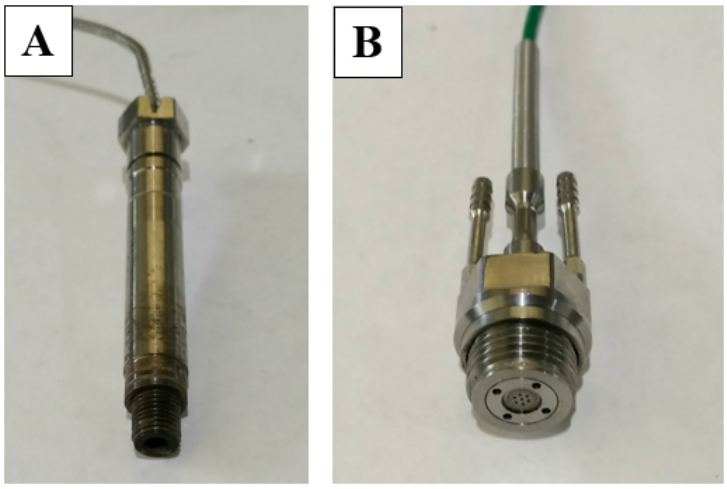

Figure 3.4: (A) piezoelectric pressure transducer, (B) piezoresistive absolute pressure sensor

peratures, type-T thermocouples were mounted on both hot and cold sides of the cooling system (e.g., inlet and outlet of the cylinder coolant passage, and before and after the radiator).

3.2 Experimental Procedure

After making sure that all the sensors are calibrated, and the DAQ system is working properly, the engine is checked for any loose parts. If everything checks safe, the engine is started. The engine then should idle for about 15 minutes to warm up, after which time the dyno with zero load is engaged to the crankshaft manually via the clutch lever. Then by adjusting the potentiometer on the dyno, the load is applied to the engine gradually, until it reaches the desired load for the current test-point. The next step would be adjusting the fuel governor to increase or decrease the speed of the engine to get to the desired value. The engine is then left running at this load-speed condition, until the coolant temperature stays constant, indicating that the engine has reached its steady-state point. At this point, the data can be recorded from the engine.

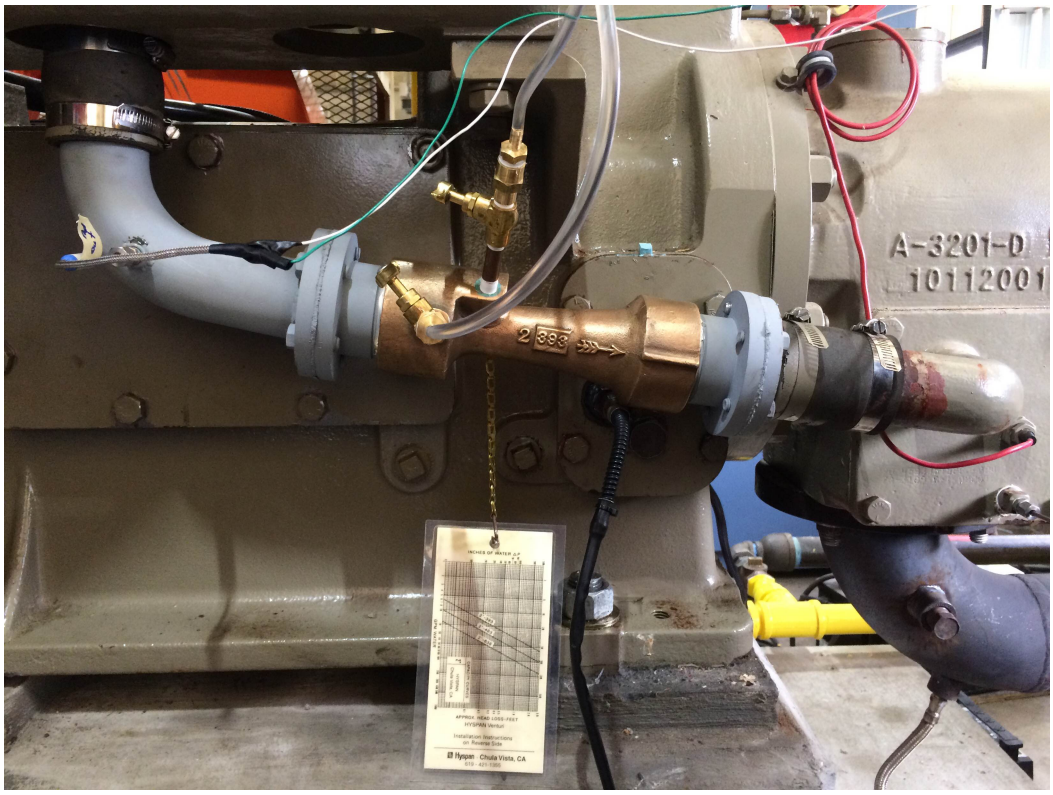

Figure 3.5: Venturi flowmeter (Image courtesy of Jeffrey Brown)

As mentioned before, the recorded data will include in-cylinder pressures, fuel intake pressure, air intake pressure, stuffing box pressure, exhaust manifold pressure, coolant flowrate, and coolant temperatures at different locations. As the pressure curves show a lot of variation (cyclic variation), an average of 300 consecutive cycles will be recorded. Additionally, 10 non-sequential individual cycles, and 10 consecutive individual cycles will be recorded. After all the data is acquired for this speed/load condition, the load and speed will change to the next test point, and this process starts over.

3.3 Test Matrix

For the purpose of the numerical simulation, the only speed-load condition desired is the full load at rated speed (HS-HL), which the engine has been designed to work at

continuously in the field. However, to help understand some of the observations, three more conditions will be tested as well. The test matrix is shown in Table 3.2.

Table 3.2: Test matrix of the experimental study

		Speed (RPM)	
		350	525
Load (% Full Load)	50	LS-LL	HS-LL
	100	LS-HL	HS-HL

4. NUMERICAL SIMULATION

In this chapter, the details of the numerical simulation are discussed.

4.1 Approach / Methodology

Convergent Science's CONVERGE CFD is the software of choice for this project. As mentioned in the LITERATURE REVIEW chapter, this software has been utilized before for many simulation studies for 2-stroke and 4-stroke gasoline, diesel, and natural gas engines. This software has some unique features, which make it appropriate for this study:

- Automatic mesh generation:

  The software utilizes an innovative run-time mesh generation technique, which helps the user avoid the time-consuming and complicated mesh generation process. CONVERGE CFD always uses perfectly orthogonal cells in mesh generation; which ensures improved accuracy, and simplified numerics. The software is also equipped with fixed embedding, and AMR (Adaptive Mesh Refinement). The latter, refines the grid size, based on user inputs, in locations where gradient of an assigned variable reaches a certain predefined critical value. This technique ensures accurate results, along with reduced total run-time. Working flowchart of the software can be seen in Figure 4.1.

Figure 4.1: Working flowchart of CONVERGE CFD from convergecfd.com/products

- Automatic handling of moving boundaries:

  Ordinarily, moving boundaries are a challenge in CFD simulations. This software automatically handles all moving boundaries, making the simulation work much simpler.

- Maintaining the true geometry:

  The software uses STL files to handle geometries, which enables the true geometry to be preserved regardless of mesh size.

- Fluid Structure Interaction (FSI) model:

  Proper simulation of the reed valve requires the solver to solve both fluid flow, and body dynamic equations. CONVERGE CFD has a powerful FSI UDF, which can be tailored for the specific needs of the simulation work.

- Combustion models:

  The software has a variety of different combustion models, including, a generalized chemical equilibrium solver, diesel ignition and combustion models, spark ignition models, premixed combustion models, and lastly the SAGE detailed chemistry solver. The latter, solves for all the chemical reactions in the combustion process, with no mechanism size limit. It is also equipped with multi-zone model, DMR (Dynamic Mechanism Reduction), and adaptive preconditioning (which improves the efficiency of linking CFD and detailed chemistry).

- Conjugate Heat Transfer (CHT) simulation:

  The idea of simulating CHT is to model flow and heat transfer in both solid and fluid regions. CONVERGE CFD is capable of simulating CHT, using a unique computational tool known as Two-Phase Super-Cycling. More details about this model are presented in Super-Cycling Method section.

With all these points in mind, it can be seen that CONVERGE CFD is the right tool for this project. In the following sections, more details of the models that are used in this project are discussed.

4.2 Case Setup

In this section, all of the steps to the simulation work are presented. Some of the experimental data acquired from the previous section will be used, and shown.

4.2.1 Geometry Preparation

The CAD file of the engine has been provided by the sponsoring company -GE Oil & Gas. A cut-view of the engine can be seen in Figure 4.2. Different parts and regions of the engine are clearly visible in this figure. The reed valve is colored gray on top of the stuffing box. It can be seen that the air and fuel enter the reed valve separately; the air enters from the top, while the fuel enters from the backside of the valve. More details about the reed valve and its working principle will be discussed in following sections. The volume behind the piston (the larger yellow body) and below the reed valve is named stuffing box; which is the place where the intake air and intake fuel are mixed. The intake manifold is the path between the stuffing box and the main chamber, which is the only connection between the two. The combustion chamber is the volume in front of the piston; this is where the combustion happens. The spark plug is colored red, and as can be seen is on the bottom of the combustion chamber. The exhaust manifold is on the bottom of the chamber, and is where the combustion products exhaust out of the chamber. The cylinder head is in blue, and the cylinder block is orange. The coolant paths are also visible in both the cylinder head, and the cylinder block.

The first step was to extract the surfaces of the engine that were needed for simulating the combustion; which included boundaries of stuffing box, reed valve (air and gas intakes and manifolds, strips, and strip holders), intake and exhaust manifolds, exhaust

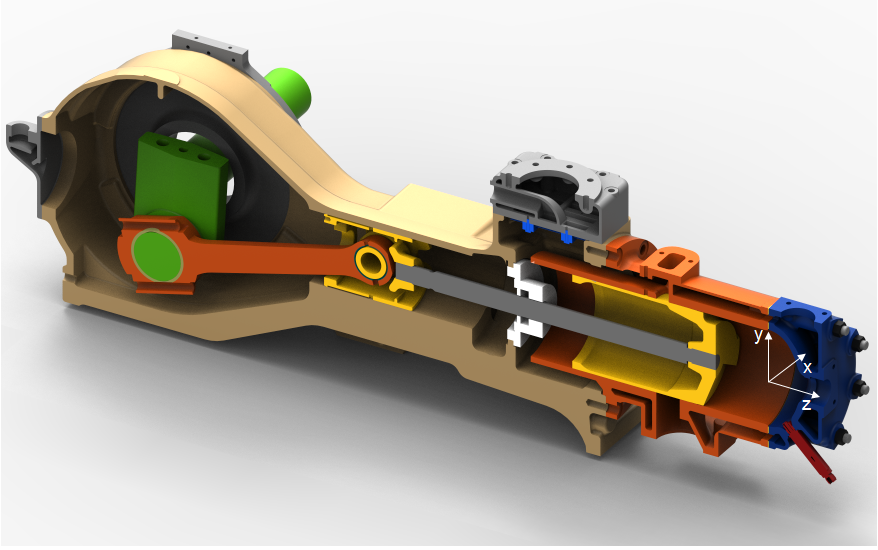

Figure 4.2: Cut view of the AJAX E-565

outlet, combustion chamber, spark plug, piston, and piston rod. This task was done using ANSYS SpaceClaim. The CAD file was cleaned up and fixed in this software, and then was exported as STL (the surface file format readable by CONVERGE CFD). The geometry was then imported into CONVERGE CFD, where it undergone another clean up and fixing, to have a proper geometry for the simulation. This time-consuming task was done, and the resulting geometry can be seen in Figures 4.3 and 4.4.

Figure 4.3 shows the whole simulation geometry. In this figure, cylinder head (in dark blue), spark plug (in red), liner (in orange), exhaust manifold (in green), intake manifold (in purple), stuffing box (in cream), reed valve strips and strip holders (in blue), fuel intake manifold (in brown), and air intake manifold (in light gray) are visible.

In Figure 4.4 the piston rod (in light gray), the piston (in yellow), the intake manifold (in purple), and the exhaust manifold (in green) are visible. This picture helps better understand the alignment of the piston crown and intake and exhaust ports. It should also be noted that the shape of the piston crown is designed to guide the intake flow towards

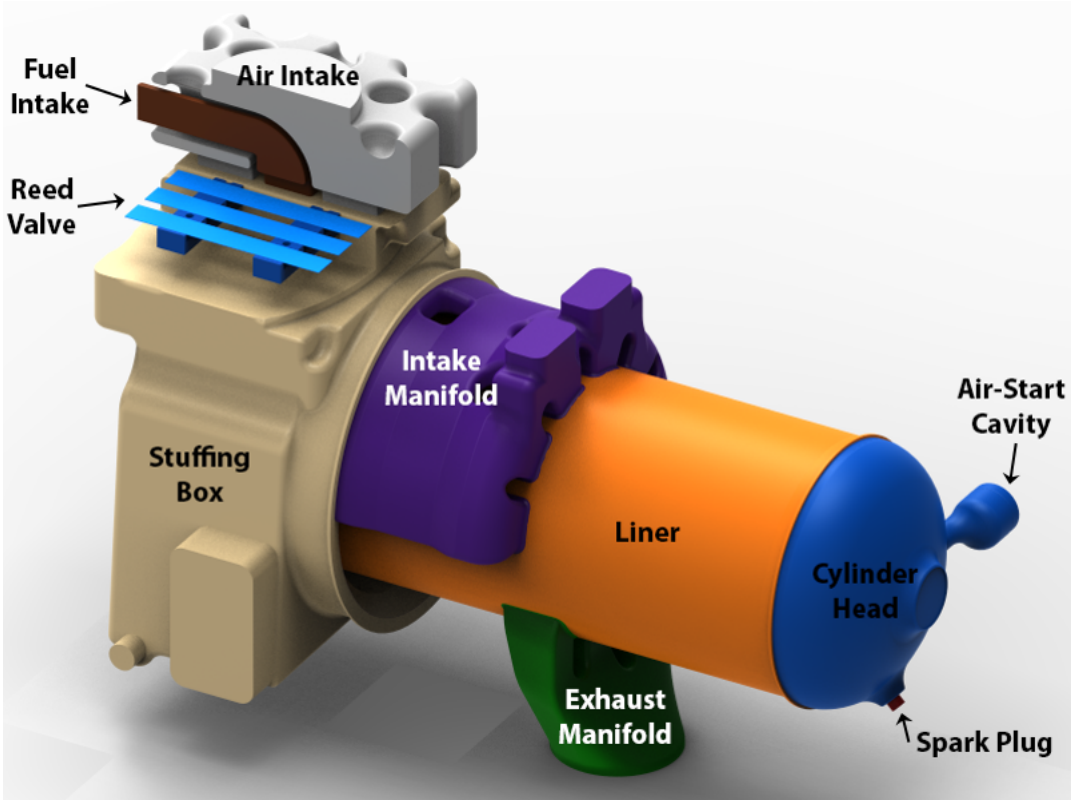

Figure 4.3: Prepared geometry for the numerical simulation (the air and gas intakes and the reed valve are shown in cut-view to help with the visualization of the whole simulation domain)

the cylinder head, and away from the exhaust manifold, to reduce the short-circuiting and improve the scavenging process. This engine has been designed based on cross-scavenging principles.

Confirming the Accuracy of the Geometry

For the numerical simulation to be accurate and reliable, the CAD file should be checked to make sure it is identical to the actual engine geometry; otherwise, the results will not be comparable with the experimental data. For this purpose, the engine was disassembled, and physical measurements were done on different parts. Figure 4.5 shows a picture from the tear-down of the engine. In this picture, the piston crown is visible inside

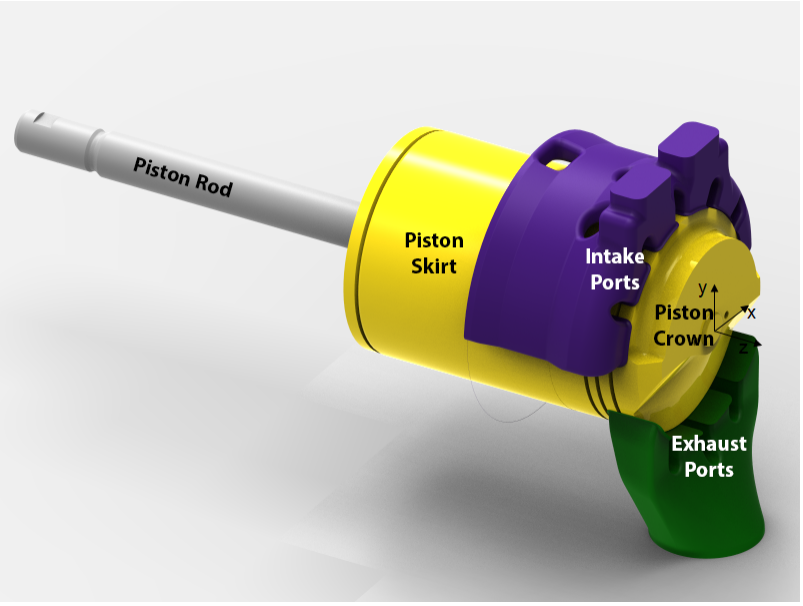

Figure 4.4: View of the piston and the piston rod vs. intake and exhaust ports

the cylinder. The piston in this picture is at BDC, so it also can be seen how the piston aligns with the intake and exhaust ports.

Figure 4.6 shows the inside of the cylinder head. In this picture, the spark plug is visible. The whole in the center is filled with a plug; this is the place where a direct injector could be mounted, if desired. The other hole on the right side goes to the air-start cavity. Currently this hole is used to mount the in-cylinder pressure transducer. Coolant paths and the gasket are also visible in this figure.

A very important factor that can significantly affect the simulation results is having the same compression ratio as the engine which is used to acquire the validation data. The compression ratio is the ratio of the volume at the BDC and the volume at TDC (clearance volume), as stated in Equation 4.1.

$$CR = \frac{V_c + V_d}{V_c} = 1 + \frac{V_d}{V_c} \tag{4.1}$$

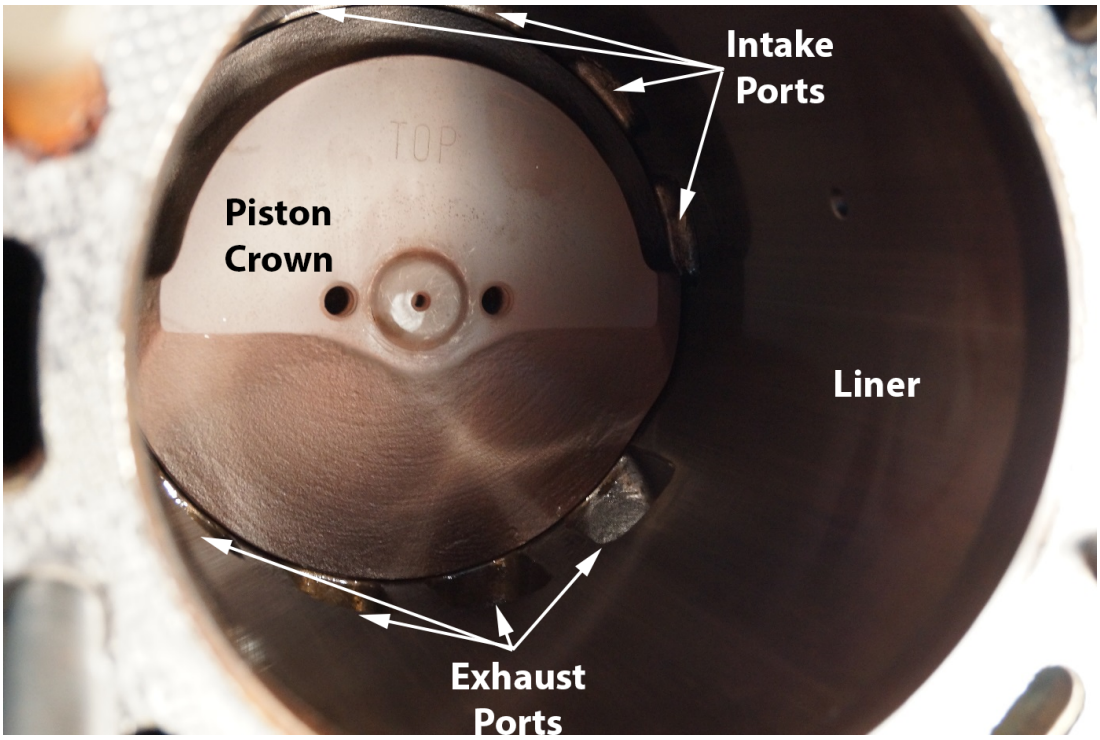

Figure 4.5: Tear-down of the engine; view of the piston crown inside the cylinder block, and against the intake and exhaust ports (image courtesy of Jacob Hedrick)

Where V_d is the displacement volume, and V_c is the clearance volume. In vertical 4-stroke engines, the clearance volume is usually measured by filling the chamber (with piston at TDC) with a thick oil, and measuring the volume of the oil. For the engine of study, since the engine is horizontal, it is not possible to measure the clearance volume this way. To make this measurement, and innovative approach was taken. Silicone molding was used to make a replica of the clearance volume. The resulting replica can be seen in Figures 4.7 and 4.8.

Figure 4.7 shows the inside of the cylinder head. The air-start cavity, which was mentioned earlier, can be seen to the right side of this picture. Additionally, the bulging in the bottom of the picture is where the spark plug sits. Figure 4.8 shows the negative of the piston crown. The top side goes against the intake ports, and is designed in such a way to

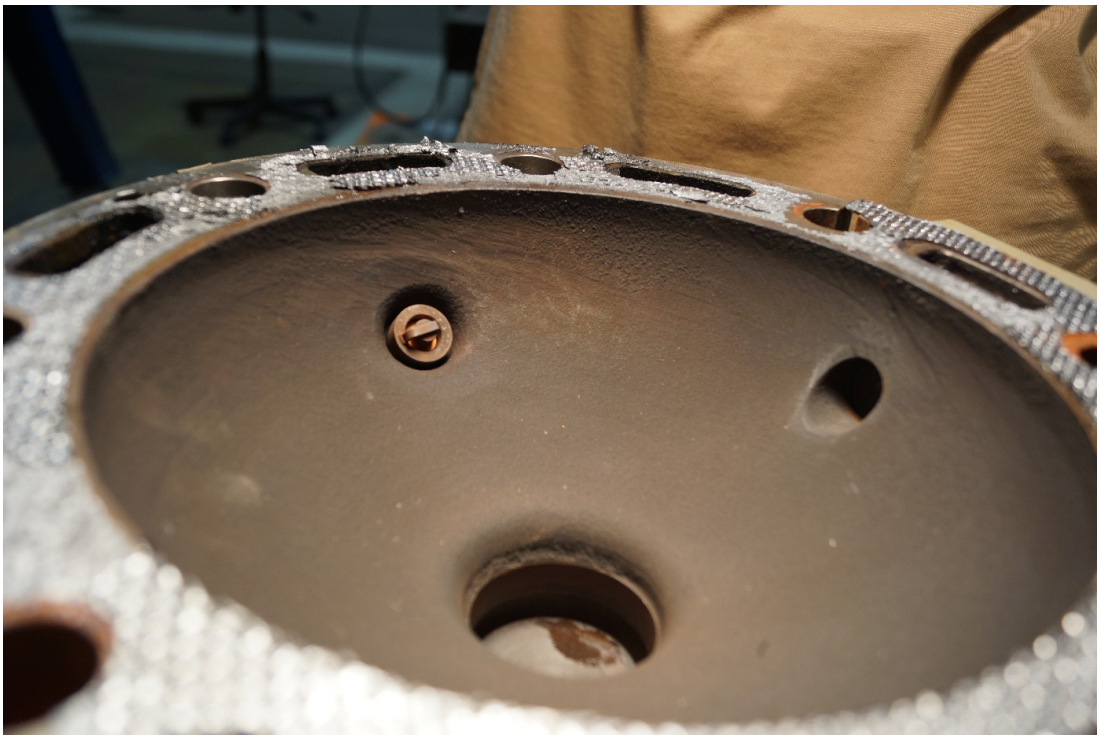

Figure 4.6: Tear-down of the engine; view of the cylinder head (image courtesy of Jacob Hedrick)

guide the intake flow towards the cylinder head and away from the exhaust ports during the scavenging process. The bottom side, on the other hand, goes against the exhaust ports.

This mold was used to measure the clearance volume, using a water displacement method. A large bucket was filled up to a certain level by water, and the amount of water was measured. The water was emptied from the bucket, and the mold was placed inside. Water was then poured in the bucket until it reached the same marking on the wall. The amount of water used, was measured again. The difference between the two volumes of water was calculated to be 1.585×10^{-3} m^3 and is the clearance volume (V_c). The piston location at TDC was then set to match this volume for the numerical simulation.

Figure 4.7: Silicone mold of the clearance volume: view of the inside of the cylinder head

4.2.2 2-Stroke Engine Cycle

At this point, a short discussion on how a 2-stroke engine cycle works is beneficial to show how the numerical simulation should be approached. Figure 4.9 shows all the important steps in a two-stroke engine cycle.

The spark plug ignites and starts the combustion event in the chamber at -11.2 ATDC crank angle degrees (CAD), while the mixture of air and fuel in the chamber is still being compressed. The chamber compression cycle continues until top dead center (TDC); from this point forward the expansion cycle of the chamber, and the compression cycle of the fresh air and fuel in the stuffing box start. The expansion of the chamber and at the same time compression of the stuffing box continue until exhaust ports open (EPO) at 120.4 ATDC; the high pressure, high temperature combustion products start exhausting through exhaust ports to the exhaust manifold. A few crank angles later (at 138.1 ATDC), intake ports open (IPO), letting the high-pressure mixture of the stuffing box enter the combustion

Figure 4.8: Silicone mold of the clearance volume: view of the piston crown

chamber. At this time, both intake and exhaust ports are open. The combustion products will continue to leave the chamber, and the intake charge will help the process. Because of the fact that both ports are open during this time, some of the fresh charges from the stuffing box will leave the chamber through the exhaust ports; this will be the short-circuiting of the engine. The piston continues moving back, until it reaches the bottom dead center (BDC). From this point forward the expansion of the stuffing box starts. This expansion will make a vacuum inside the stuffing box, which will force the reed valve strips to open, letting fresh air and fuel enter the stuffing box. The cycle continues until the intake ports are closed (IPC) at -138.1 ATDC, and a few crank angles later (at -120.4 ATDC) the exhaust ports will get closed (EPC). This is the start of compression cycle in the chamber, moving towards TDC, and this cycle repeats.

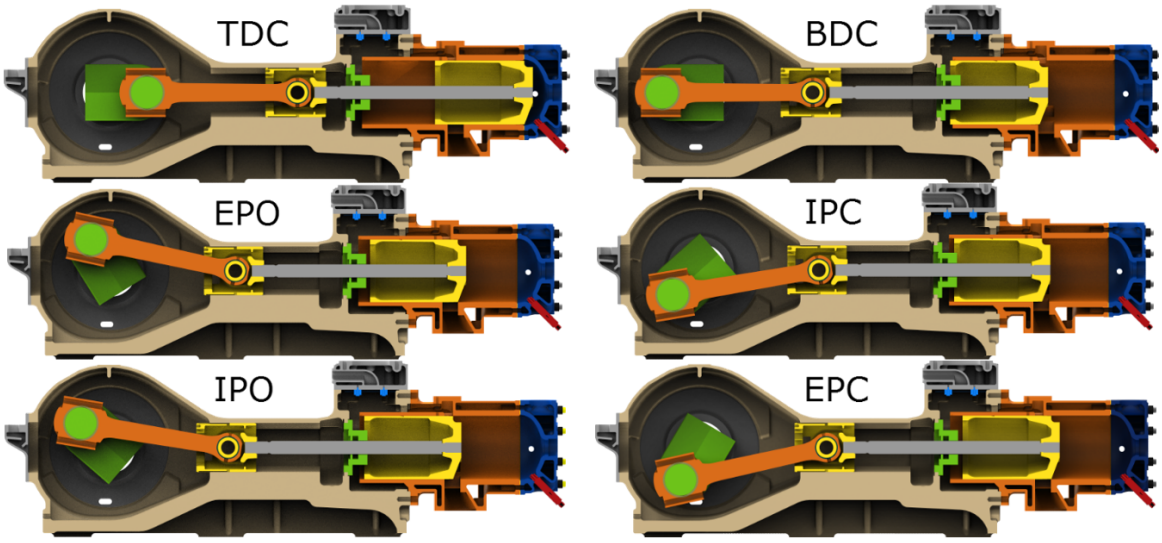

Figure 4.9: Important steps in a two-stroke engine cycle

The timing map of the engine is presented in Figure 4.10. It can be seen that the port timings are symmetrical, and that the EPO happens 17.7 CAD before the IPO.

4.2.3 Reed Valve

As mentioned in the explanation of the 2-Stroke Engine Cycle, in this engine, a reed valve is controlling the air and fuel that enter the stuffing box during its expansion cycle. As shown in Figure 4.3, air and fuel enter the stuffing box through the reed valve, separately. It also can be seen in Figure 4.11 (A) & (B), where the separate paths for the air and the fuel intakes are visible.

The reed valve consists of six spring-loaded steel strips, which are visible in Figure 4.11 (C). These strips can move individually, and their maximum displacement is 5.5 mm. The bottom side of all the strips is exposed to the stuffing box pressure, while the white regions on the top sides of the strips are exposed to intake air pressure, and the red regions on the tops of the two middle strips are exposed to intake fuel pressure. The strips move based on the forces applied to each individual one. When the balance of forces on a

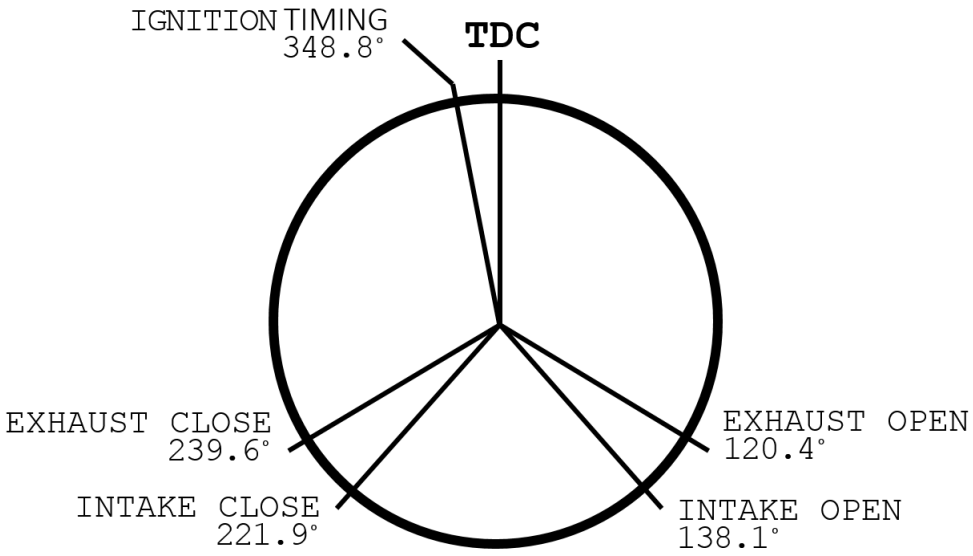

Figure 4.10: Timing map of the AJAX E-565

strip is in -z direction (which happens during the expansion of the stuffing box), that strip starts opening, letting the intakes to flow into the stuffing box. Later when the piston starts moving towards BDC (during the compression of the stuffing box) the direction of the balance of forces changes, causing the strips to move upward until they seal against the reed valve body, which will eventually stop the flow into the stuffing box. The total area covered by air (summation of white areas) is 15.96 in^2 (102.96 cm^2), while the area covered by fuel (summation of red areas) is 1.72 in^2 (11.1 cm^2); the ratio of fuel area to air area is equal to 0.108.

A mechanically governed throttle sits before the reed valve on the fuel line. The throttle and the reed valve are the only parts that control the AFR (air/fuel ratio) of this engine.

4.2.4 Fluid Structure Interaction (FSI) UDF

At start, a pressure difference-based (PDB) UDF was used to simulate the reed valve, which was starting/stopping the flow from the upstream intakes to the stuffing box, based on user-defined ΔP_{open} and ΔP_{close} values. In this method, ΔP stands for the difference

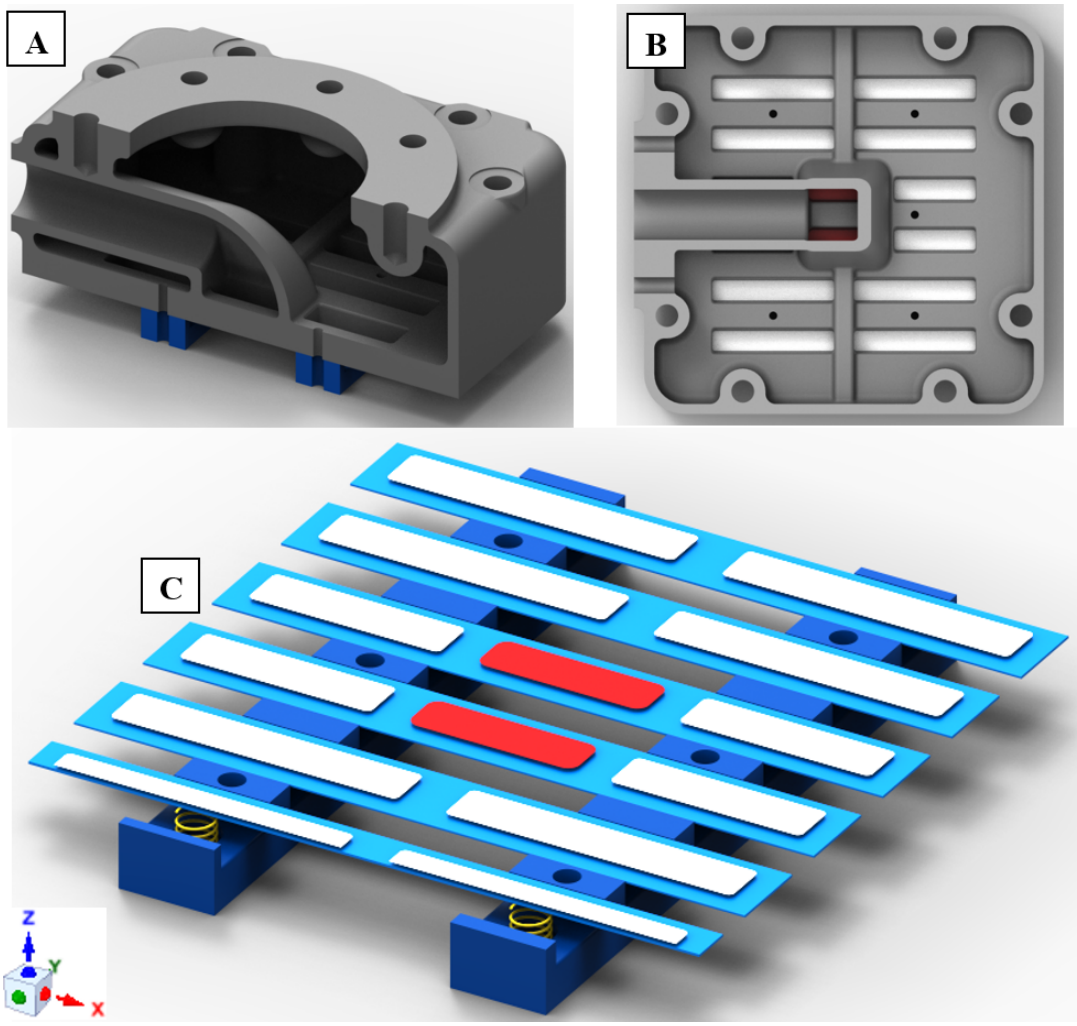

Figure 4.11: Reed valve parts; (A) vertical-cut view, (B) horizontal-cut view, (C) spring-loaded strips, with one half-cut view strip

between the average pressure of the air intake manifold, and the average pressure of the stuffing box. Satisfying results were not achievable using this method (for more details please refer to "Prediction of Air-Fuel Ratio Control of a Large Bore Natural Gas Engine Using CFD Modeling of Reed Valve Dynamics" [9]). After the failure of the simulations with PDB UDF, a high-speed camera was used to observe the behavior of the reed valve strips while motoring the engine. Closer analysis of the video, showed that the strips

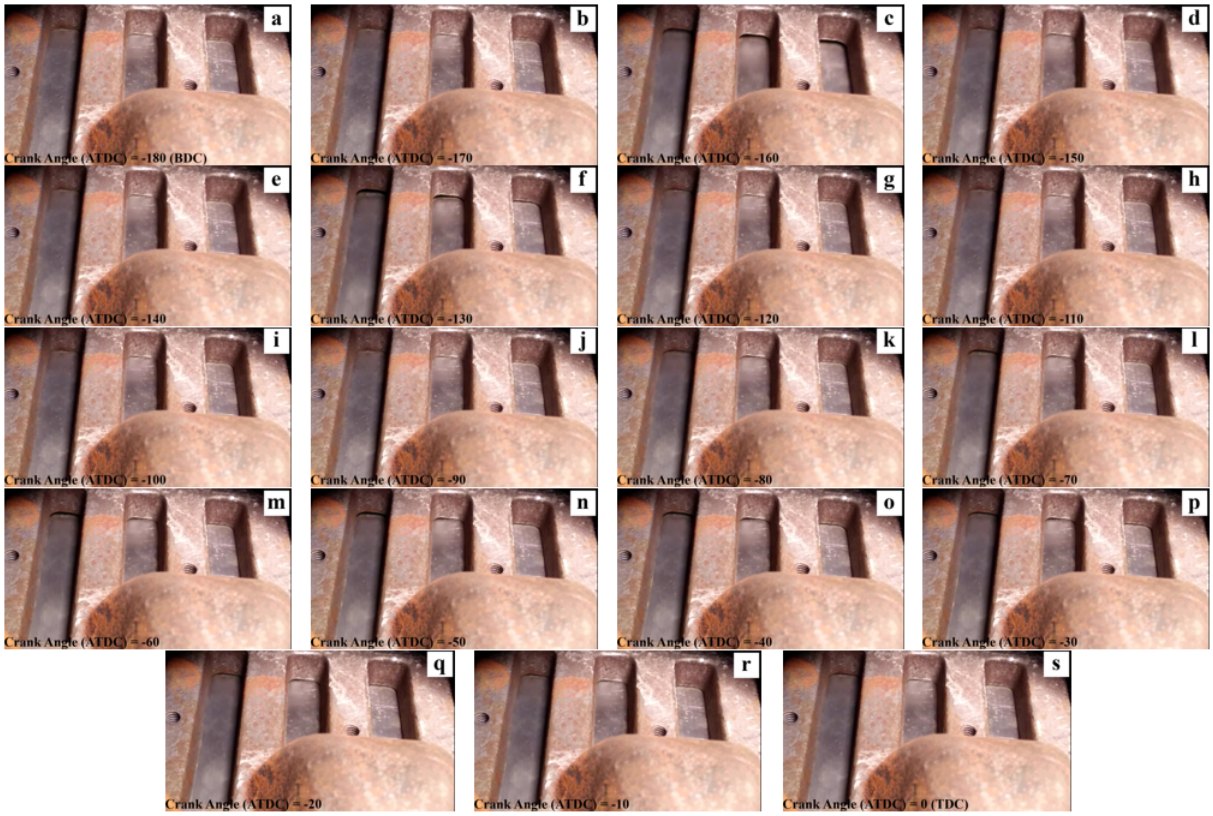

Figure 4.12: Still-frame images from the motion of the strips

present a fluttering behavior, as presented in still-frame images in Figure 4.12.

In Figure 4.12, it can be seen that the strips are closed at BDC (a); they then slightly open in (c), and are closed again in (d); for a second time, they open in (f), and close in (g). The strips open once more in (l), and remain open through (p), and they will not open for the rest of the cycle. It is very important to note that the strips move individually, and differently. In addition, it has to be noted that there are several open/close events for the reed valve strips, in just one cycle of the engine.

Knowing the complexity of the behavior of the reed valve, fluid structure interactions deemed capable of doing the simulations. As shown in LITERATURE REVIEW, FSI methods have been used for simulating different types of reed valves by a number of

researchers, and acceptable results have been achieved.

With FSI, in addition to the fluid flow, the solver solves the momentum equation for each strip, and considers all the pressure forces, and the flow field around the strips in the calculations. This makes the simulation of the reed valve much more dependable, and accurate. More details on the formulation of the FSI solver can be found in the Fluid Structure Interaction (FSI) section of the FORMULATIONS.

For the FSI model, the density of the strips, the spring constants, the free length of the springs, and the pre-load on the springs were needed. To this end, the reed valve was disassembled; an apparatus was made to measure the displacement of the springs using known weights. The spring constant was calculated to be 3 lbf/in (525 N/m). The free length of the springs is 0.515 in (1.3 cm), and the installed length is 0.383 in (0.97 cm). Based on this, the pre-load on each strip is set to 0.79 lbf (3.52 N).

4.2.5 Configuration of Seals

Boundary intersection is not allowed in CONVERGE CFD. To avoid having intersections, the diameter of the piston skirt should be slightly smaller than the liner diameter. This tiny gap between these two parts causes impractical flow between the separate regions in the simulation. The sealing feature solves this problem.

For sealing feature to work properly, perfect boundaries are required. To achieve these perfect boundaries, the liner and the piston skirt were repaired in the software after importing, and then the ports were projected on the liner surface. Two sets of seals had to be used to stop the leakage between the regions completely:

1. A seal to close the gap between the piston skirt and the liner, as visible in Figure 4.13 (A). This set of seals will prevent the leak from the combustion chamber to the stuffing box, through the gap between the liner and the piston skirt.

2. A seal to stop the flow from the intake and exhaust ports into the gap between the

liner and the piston skirt. This set of seals can be seen in Figure 4.13 (B). As can be seen, the seals are perpendicular to the piston skirt and liner; this is only achievable if perfect boundaries are properly made before defining the seals.

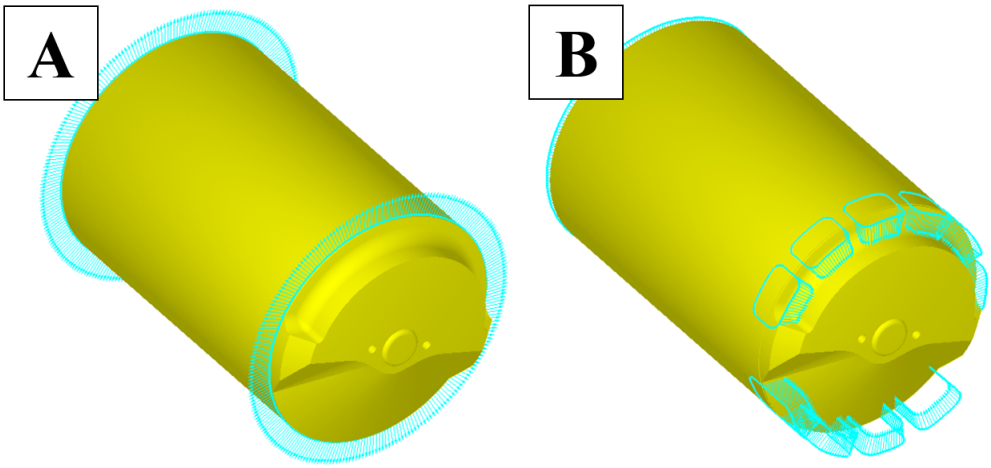

Figure 4.13: Seal configuration from: (A) the piston skirt to the liner; (B) the intake and exhaust ports to the piston skirt

4.2.6 Boundary Conditions

To set up the simulation, boundary conditions for all of the inlets (fuel and air intake), outlets (exhaust), and walls should be defined. As mentioned in the Test Matrix section, the numerical simulation will only focus on the full load (400 ft-lb), rated speed (525 RPM) case.

Pressures

A few initial simulations were done, using constant pressures for all the inlet and outlet boundaries, and the results did not match the experimental data as closely as desired (for more details please refer to "Prediction of Air-Fuel Ratio Control of a Large Bore Natural

Gas Engine Using CFD Modeling of Reed Valve Dynamics" [9]); this prompted the use of experimentally measured, crank angle resolved pressures for all of these boundaries.

As mentioned before, a piezoresistive pressure transducer was used to capture the crank angle resolved pressures at different locations on the engine. Total pressure is required for the simulation work. Total pressure pitot tubes were made from bendable aluminum (Figure 4.14) to make these measurements. The pitot tubes were mounted in such a way to face the flow, and sit at the center-line of the pipes.

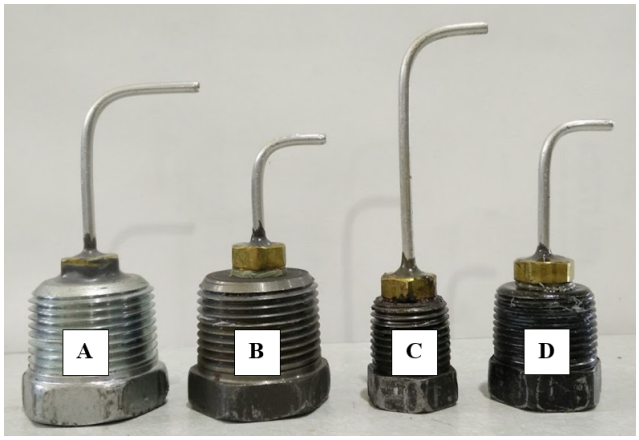

Figure 4.14: Total pressure pitot tubes used for pressure measurements at (A) air intake manifold, (B) fuel intake manifold, (C) exhaust manifold, (D) stuffing box.

To make sure that the boundary condition is set at the same location that it is captured experimentally, the geometry of the air intake pipe, and fuel intake pipe up to the points of measurement were added to the simulation geometry, as presented in Figure 4.15. The green part is the fuel intake, and the blue is the air intake.

To make sure that the boundary variations are not significant from one cycle to another, ten randomly selected individual cycles are overlaid on the average of 300 cycles. The results are presented in Figure 4.16 (A), (B), and (C). It can be seen that the variations are

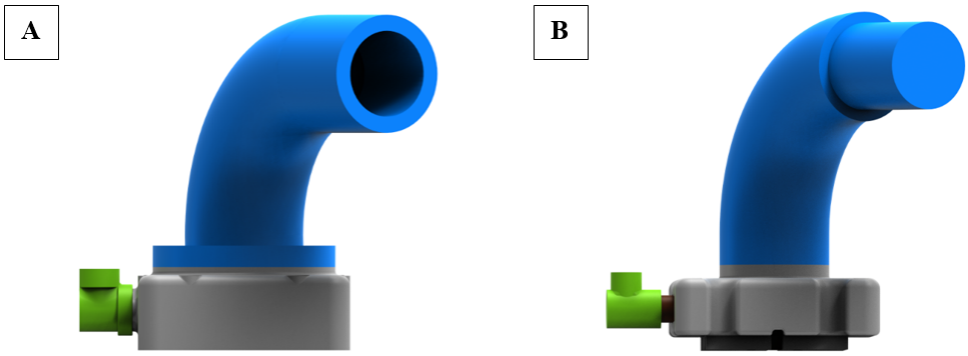

Figure 4.15: Air and fuel intake pipe geometries; (A) external surfaces, (B) extracted internal surfaces for the simulation.

small compared to the range of data, and so the pressures are stable at all the points. The average of 300 cycles were used as boundary conditions.

Temperatures

For the initial simulation of the engine (without considering the CHT), constant wall temperatures are defined as boundary conditions. Different values are set for each boundary, based on best guesses; ambient temperature (313 K) for the fuel intake, air intake, and valve walls, slightly higher temperatures (350∼400 K) for the stuffing box walls, and much higher temperatures (750∼800 K) for the walls that surround the combustion chamber (liner, cylinder head, spark plug, and piston crown).

The inlet boundaries also need a temperature for the fluid, which has been set as ambient temperature for both air and fuel intakes. The exhaust back-flow temperature is also set at a very high temperature (750 K), which has been found experimentally from the exhaust pipe.

Piston Motion

All the boundaries are set as stationary walls, except for the piston crown, piston skirt, and the inner surface of the piston, which move based on a predefined piston motion profile

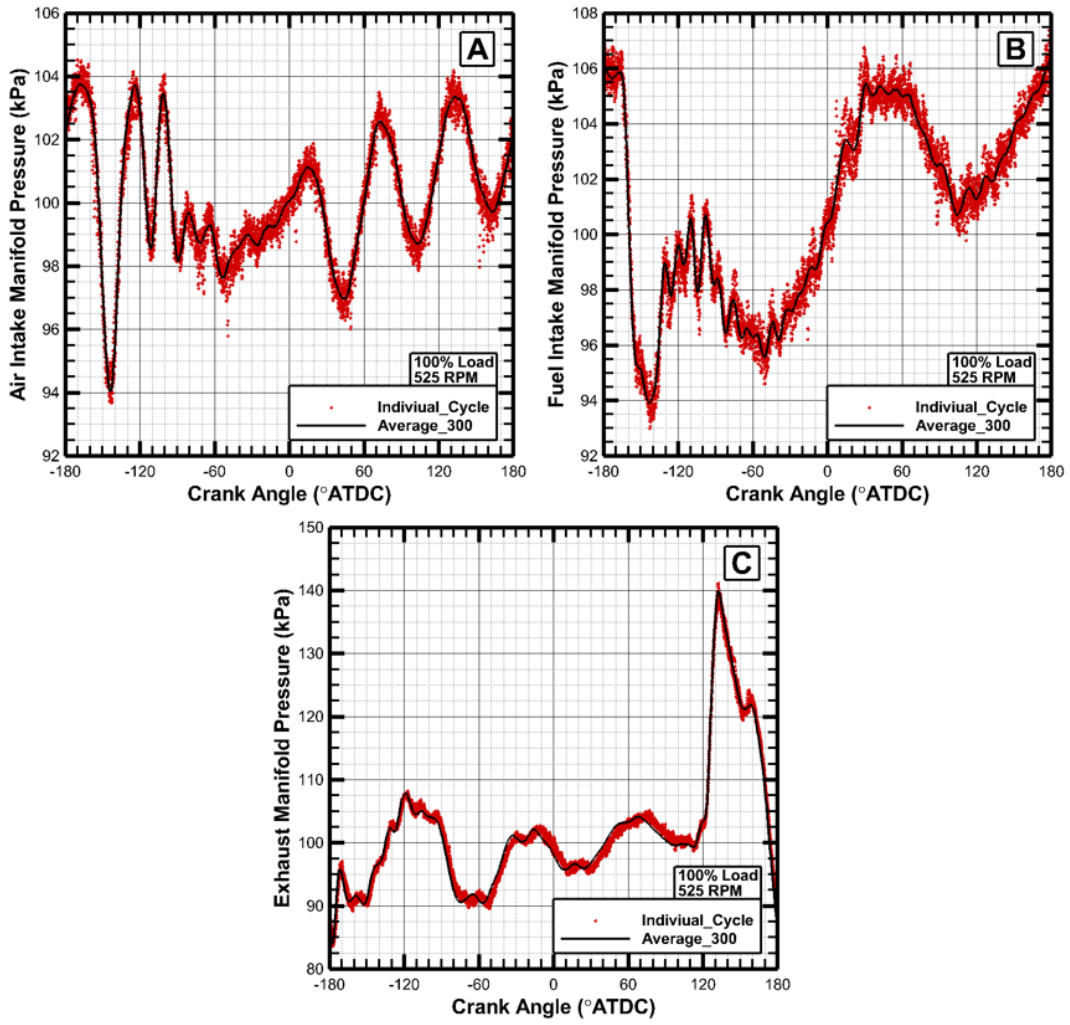

Figure 4.16: Experimental boundary conditions used for the simulation; (A) air intake manifold pressure, (B) fuel intake manifold pressure, (C) exhaust manifold pressure.

(Figure 4.17).

Inlet and Outlet Species

The species mass fractions listed in Table 4.1 were used for the inlet and outlet boundary conditions. The exhaust species are the products of an ideal reaction of a mixture with $\phi = 0.81$. The species of the fuel were set based on the gas analysis provided by local municipality on 03/03/2015 [70].

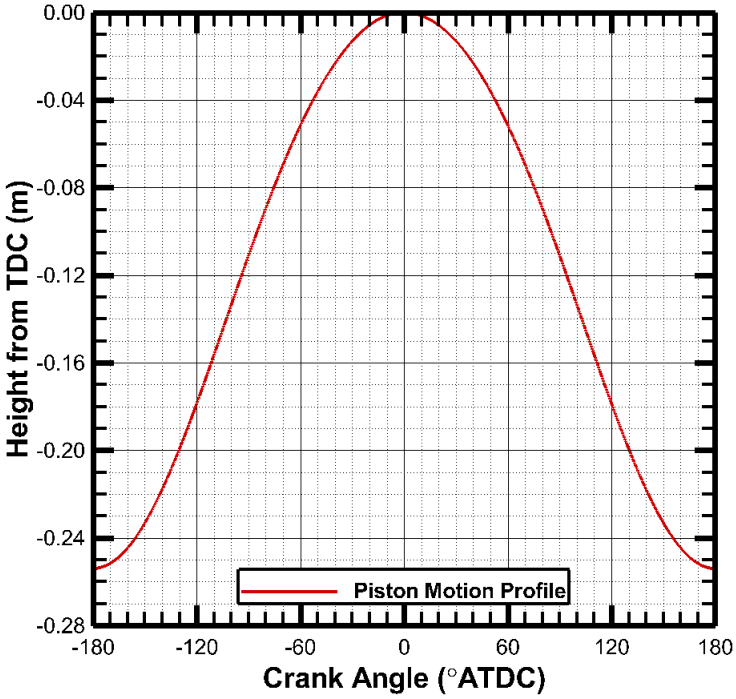

Figure 4.17: Piston motion profile

Walls

For all the walls law-of-wall is set as the velocity boundary condition, which is the well-established practice for the turbulent flows.

Passives

Setting passives for all the inlet and outlet boundaries helps with tracking the flows, and calculating the back-flow from the exhaust manifold to the chamber. For this purpose, five passives were defined:

- AIR_IN: The air that enters through the air intake manifold.
- GAS_IN: The fuel that enters through the fuel intake manifold.
- INTAKE_MIXED: The mixture that is inside the stuffing box.

Table 4.1: The mass fraction of species at the inlet and outlet boundaries

Boundary	Species	Mass Fraction
Air Intake	O_2	0.23
	N_2	0.77
Fuel Intake	CH_4	0.8613
	C_2H_6	0.7850
	C_3H_8	0.0061
	CO_2	0.0281
	N_2	0.0259
Exhaust Outlet	CO_2	0.1265
	H_2O	0.0998
	N_2	0.7315
	O_2	0.0422

- CHAMBER: The mixture inside the chamber.
- EXHAUST: The combustion products that are in the exhaust manifold.

4.2.7 Initial Conditions

Experimental data are used to set the initial values for variables in different regions (volumes in the solution domain). The following variables need to be set for each region as initial condition:

Temperature

Initial temperature for the fuel intake manifold and the air intake manifold are set equal to ambient temperature on the test day. Initial temperature of the exhaust manifold is set from the experimental data. Initial temperature of the stuffing box and the combustion chamber are set based on best guesses.

Pressure

Initial pressures in all the regions were set using experimental data.

Species

The initial mixture of the air intake manifold and the fuel intake manifold are set based on the known mass fractions of the species. The stuffing box is assumed to have equivalence ratio of 0.81 based on the experimental data, and so the species in the stuffing box are set accordingly. The simulation will be started at EPO; hence, it was assumed that the initial mixture of the chamber is composed of products of complete combustion of a mixture with $\phi = 0.81$. The exhaust manifold initial mixture was assumed the same as the combustion chamber.

4.2.8 Gas Simulation

For gas simulation, Redlich-Kwong model will be used. This model is in general the preferred equation of state for non-ideal gas behavior, which can be of significance in high-pressure, high-temperature situations [71]. This model is formulated as a cubic equation in the following form (Equation 4.2):

$$P = \frac{RT}{v - b} - \frac{a}{v^2 + ubv + wb^2} \tag{4.2}$$

Where the coefficients are defined as presented in Table 4.2.

Table 4.2: Coefficients for Redlich-Kwong equation of state

u	w	b	a
1	0	$\beta_{rk} v_c$	$\alpha_{rk} \frac{P_c v_c^2}{\sqrt{T_c}}$

Where $v_c = \frac{RT_c}{P_c}$, $\alpha_{rk} = 0.42748$, and $\beta_{rk} = 0.08664$. In this equation, v_c is the critical volume; T_c is the critical temperature; P_c represents the critical pressure; α stands for the attractive forces between molecules; and finally β is the volume of the molecules [72].

4.2.9 Reaction Mechanism

A reaction mechanism is a set of elementary chemical reactions that describe an overall chemical reaction. For example, the reaction of methane (CH_4) and oxygen (O_2), can be closely described in a set of 325 reactions, with 53 species [73], as explained in Reaction Mechanism section. GRI-Mech 3.0 will be the reaction mechanism used for the simulations. This mechanism is optimized for modeling natural gas combustion, and includes NO formation, as well as re-burns chemistry.

4.2.10 Gas Flow Solver

Gas flow solver is set to compressible. It is obvious that in high pressures and temperatures that are present in internal combustion engines, gases should be considered compressible, as the gas density changes with changes in temperature and pressure.

4.2.11 Combustion Modeling

SAGE detailed chemical kinetics solver, which solves for all the chemical reactions in the combustion process, with no limit in mechanism size, will be used to simulate the combustion. For more details on the formulation of multi-step chemical mechanisms, please refer to Formulation of Chemical Kinetics with Multi-Step Mechanisms in the FORMULATIONS. The SAGE solver starts 0.1 CAD before the spark timing, and stops at EPO.

Multi-Zone Model

All the cells at each discrete time, t, are at some thermodynamic state; solving detailed chemistry solver (SAGE) in zones (groups of cells with similar thermodynamic states) can accelerate the solution of detailed chemical kinetics [72, 45, 74]. Zoning is based on temperature and equivalence ratio in a 2D zoning strategy. SAGE chemistry solver runs only once for each zone. The average of temperature and composition of all the cells in a

zone will be considered as thermodynamic state of that zone.

Reaction is allowed in each zone from time t to $t + dt$. At time $t + dt$ the new composition of the zone is obtained, and mapped back to all the individual cells in that zone. The quality of the multi-zone model is strongly dependent on the remapping strategy. Further details can be found in CONVERGE Theory Manual [72].

Source Modeling

To simulate the spark ignition, a source volume is added to the combustion chamber, where the edges of the spark plug electrodes are. The total energy that the source releases during the spark ignition is set to 150 mJ. This energy will be released in a sphere with radius of 0.5 mm, in 236 μsec (which is the spark duration), starting at -11.2 ATDC CAD. The source is allowed to move with the flow for 1 mm at most, and then it will be reset at its initial location. During the spark event, the temperature inside the spark sphere reaches very high values (up to 50,000 K) as presented in Figure 4.18, which will initiate the combustion, by starting the flame kernel.

4.2.12 Turbulence Modeling

Proper simulation of turbulence is critical for an accurate simulation, since the rate of mixing of momentum, energy, and species increase with turbulence. Simulating all the turbulent eddies at all the length scales for large applications is not feasible with the current computational power; this makes using a turbulent model necessary to make up for the additional mixing that is not captured through the simulation.

For this purpose, Reynolds Averaged Navier-Stokes (RANS) equations, with $RNG\ k-\varepsilon$ turbulence models were used. Further details of these models can be found in Reynolds Averaged Navier-Stokes (RANS) section in the FORMULATIONS.

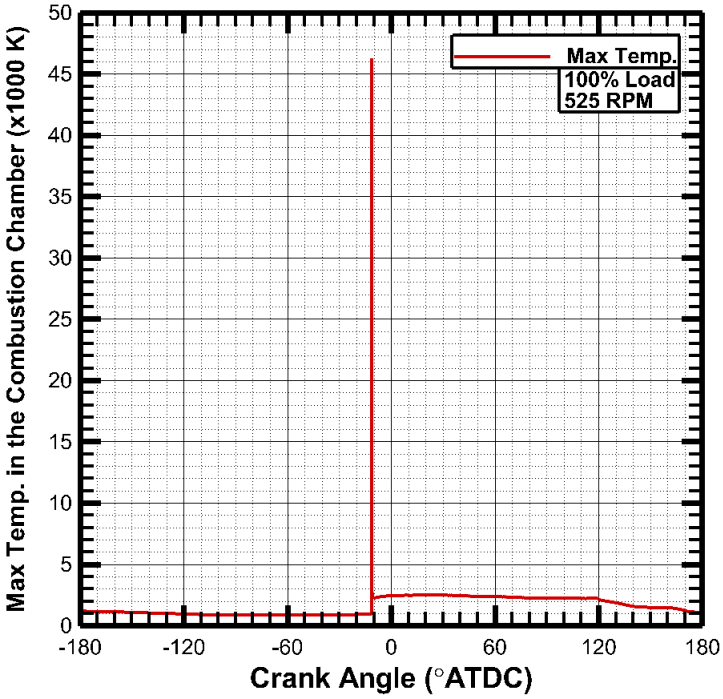

Figure 4.18: Maximum temperature inside the spark sphere

y$^+$

Although it may be necessary for the accuracy of the results, for some cases, it may not be possible to refine the grid up to the point that resolves the viscous sub-layer. To make up for this problem, a law-of-the-wall boundary condition is specified, which is a logarithmic curve fit for a turbulent boundary layer. With $k - \varepsilon$ turbulence model, the standard law-of-the-wall is used, as presented in Equation 4.3. The law-of-the-wall helps determine the tangential components of the stress tensor at the wall.

$$u^* = \begin{cases} \frac{1}{\kappa}\ln(E\mathrm{y}^+) & \mathrm{y}^+ > 11.2 \\ \mathrm{y}^+ & \mathrm{y}^+ \leq 11.2 \end{cases} \tag{4.3}$$

In this equation, $E = 9.8$, and y$^+$ is defined by Equation 4.4:

$$\mathrm{y}^+ = \frac{y\rho u_\tau}{\mu} \tag{4.4}$$

The stress tensor, σ_{ij}, can be written as:

$$\sigma_{ij} = \frac{U_{i,\tan}\rho u_\tau n_j}{u^*} \tag{4.5}$$

In Equation 4.5, u^* can be replaced from Equation 4.3, to get:

$$\sigma_{ij} = \frac{U_{i,\tan}\kappa\rho u_\tau n_j}{\ln(E\mathrm{y}^+)} \tag{4.6}$$

In this equation, $u_\tau = c_\mu^{1/4} k^{1/2}$, where k is the turbulent kinetic energy, and c_μ is the model constant for the $k-\varepsilon$ turbulence model.

The expression in Equation 4.6 will be used to make up for not being able to resolve the viscous sub-layer. When law-of-the-wall is used for boundaries, the desired value of y^+ is between 30 and 100 ($30 < \mathrm{y}^+ < 100$).

4.2.13 Super-Cycling Method

Ideally, the flow and heat transfer equations should be solved simultaneously in both the solid and fluid regions to get the best results. However, because the heat transfer process for solid regions has orders of magnitude larger time-scales than the fluid regions, it is not practical to run one coupled transient simulation to capture the conjugate heat transfer. Instead, a unique approach, called Super-Cycling [75] will be used. The results of the first simulated combustion cycle will be used to set boundary and initial conditions of the CHT simulation.

The following are the steps of a simulation with Super-Cycling:

1. Without storing the solid heat transfer data, both the fluid and solid equations are solved, with the goal to develop the fluid flow field.

2. At a predefined *supercycle_start_time*, values of HTC (heat transfer coefficient) and near-wall temperature at the solid/fluid interface will be stored for each cell.

3. For a predefined time (*supercycle_stage_interval*), the solver continues solving both fluid and solid equations, and stores HTC and near-wall temperatures.

4. When the time reaches *supercycle_start_time*+ *supercycle_stage_interval*, the fluid solver will be paused. At this point, time-averaged HTC and near-wall temperatures at the interface of solid/fluid will be calculated for each cell, based on values stored in step 3. Using these time-averaged values, the solver calculates the solid heat transfer with steady-state assumption, until the predefined tolerance of *supercycle_sie_tol* is achieved. This calculated steady-state solid temperature, will represent the temperature of the solid in the next step.

5. For a second time, both solid and fluid equations are solved, for a duration of *supercycle_stage_interval*. The fluid temperatures will change significantly at this step, due to the newly calculated solid temperatures of the previous step. The calculations continue, until the fluid temperatures level off; this is due to not enough temperature difference between the solid and fluid regions at the given flowrate. At the same time, the solver stores the HTC and near-wall temperatures for this step, at the interface of the solid-fluid phases for each cell.

6. The fluid solver will be paused again, when time reaches *supercycle_start_time*+ (2$\times$*supercycle_stage_interval*); this triggers the recalculation of the time-averaged HTC and near-wall temperatures that were stored in just the previous step. The solver also calculates the solid heat transfer equations as described in step 4.

7. This iterative process repeats, until the predefined end time is reached.

This method will be used to simulate the conjugate heat transfer (CHT) in the solid

parts, and through the cooling system. After the results are achieved, the newly calculated wall temperatures from the CHT simulation will be mapped to the combustion chamber walls for the next cycle of the combustion simulation. Then the newly calculated convective heat transfer coefficients and near-wall gas temperatures will be used for the next cycle of CHT simulations. This iteration should be done a couple of times, until the wall temperatures converge to their final values.

4.2.14 Grid Generation

As mentioned in the Approach / Methodology section, CONVERGE CFD generates the mesh in every time step automatically; this means that the time-consuming and critical task of grid generation is done after each time step by the software. CONVERGE uses perfectly orthogonal cells, which result in improved accuracy, and simplified numerics.

Different base grid sizes were tested; at the end, considering the computational resource limitations, base grid size of 7.5 mm was selected. Using finer grid would have increased the simulation time so much, that it would not be feasible to run the simulation any more. CONVERGE has features such as adaptive mesh refinement (AMR), and fixed embedding, which can make up for the rather large base grid size in important regions such as combustion chamber, around the spark plug, close to the intake and exhaust ports, and around the reed valve strips.

Adaptive Mesh Refinement (AMR)

In regions with high gradients of the following six variables, AMR can be activated: velocity, number of parcels per cell, temperature, species, passives, or boundary (y^+). In the combustion chamber, because of high gradients of velocity, temperature, and species, level 3 of AMR was used; this reduces the grid size to 0.94 mm. In the stuffing box, and the reed valve, high velocity gradients are present, because of which, AMR level 1 was used in these regions; this refines the grid size to 3.75 mm.

To avoid increasing the total number of cells to a point where the simulation was infeasible, the maximum number of cells in the whole domain was set to 3×10^6. This limits the AMR feature, to add too many cells to the domain. When level n of AMR is called in a group of cells with high gradients, those cells will be divided into 2^n finer cells, during the time that the high gradients are available. This is why the AMR was only activated in the reed valve region, during the suction cycle of the stuffing box, and during the gas exchange process; it also was activated in the chamber for only the velocity during the gas exchange, and then for velocity, temperature, and species, during the combustion process.

It has been shown in literature, that utilizing AMR will improve the accuracy of the simulation, without increasing the overall grid size too much. [76, 77, 78] Utilizing AMR could eliminate the need to run a grid independence test.

Fixed Embedding

In addition to AMR, fixed embedding was used in places where finer grid size was critical to the accuracy of the solution. For example, the close vicinity of the spark plug needs a much finer grid, to capture the details of the flame kernel growth. With fixed embedding, same as AMR, the grid size will be refined based on Equation 4.7:

$$dx_{\text{embed}} = \frac{dx_{\text{base}}}{2^{\text{embedding scale}}} \tag{4.7}$$

To capture the wall effects on the flow better, fixed embedding level 1 (3.75mm grid size) was set for all the walls. Additionally, the whole combustion chamber was embedded with level 3 (0.94 mm grid size), starting 1 CAD before start of spark ignition, and the embedding lasted for 20 CAD after ignition. Grid was also strongly refined around the spark plug, with embedding level 5 (0.23 mm grid size), in a cylinder shape around the electrode of the spark plug. This was done to make sure the initial growth of the flame kernel is properly captured. It has to be noted that CONVERGE will automatically add

intermediate grid sizes to smoothly transition from the very fine grid (level 5 embedding) to the chamber grid (level 3 embedding). The spark plug embedding was also started 3 CAD before the spark timing to let the flow field around the spark plug properly solved before ignition, and was kept for 20 CAD after the start of ignition. The combustion chamber and the spark plug area grids can be seen in Figure 4.19.

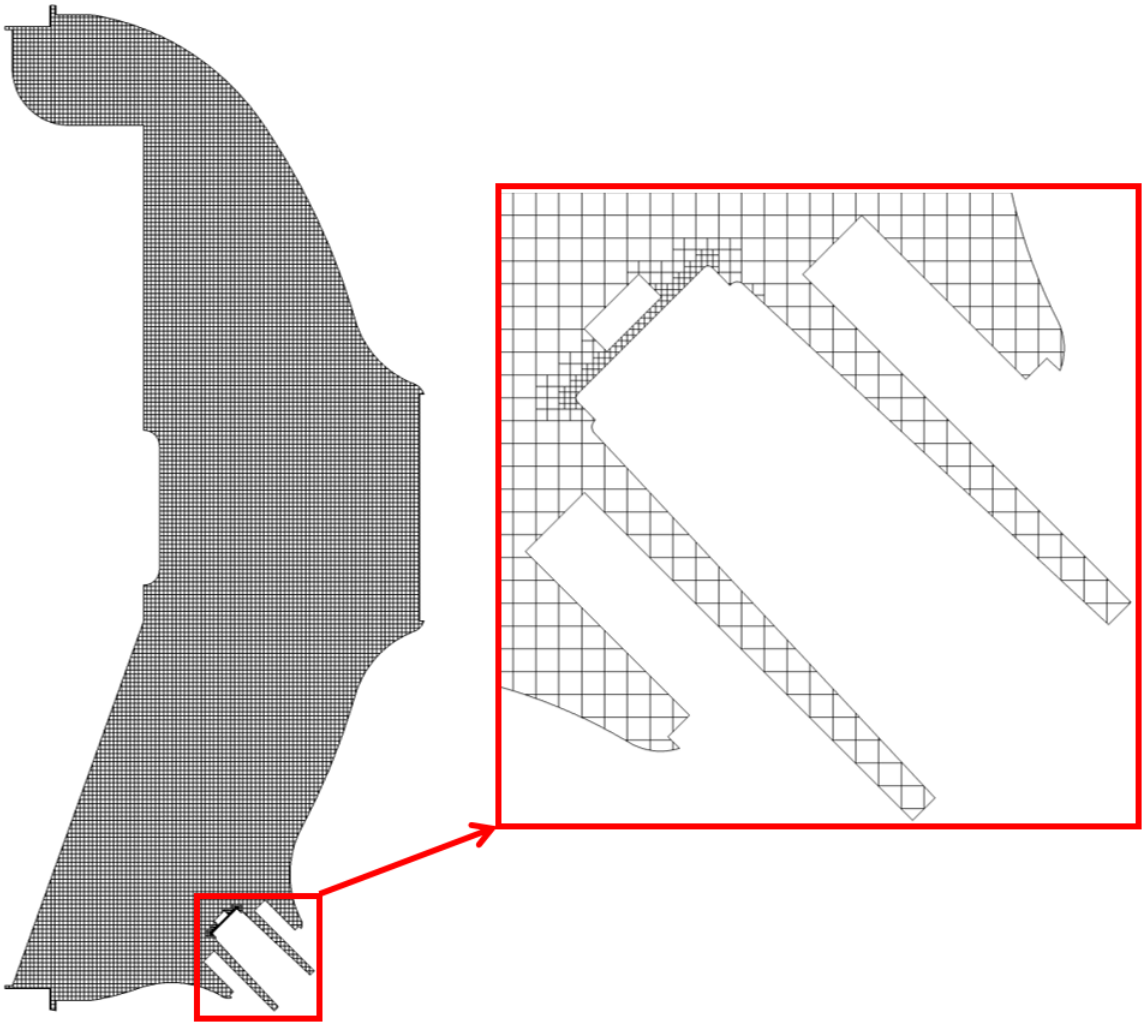

Figure 4.19: Grid of the combustion chamber and around the spark plug, right at the ignition timing, on a cut plane in the center of the chamber

5. RESULTS AND DISCUSSION

After selecting all the models, and setting the boundary and initial conditions, the simulations were started on the Texas A&M University's supercomputers. The simulations were parallelized on 40 cores, with 10 GB of memory assigned per core. As mentioned earlier, the maximum number of cells is limited to 3×10^6 , which means that at max number of cells, each core has to deal with 75,000 cells. The optimum number of cells per core is somewhere around 20,000 to 50,000. The simulations continued for nine full rotations of the engine (cycle). The simulation of each cycle takes almost eight wall-clock days. The results of the 1st cycle are neglected, as the initial conditions are not yet washed away; this means that only eight cycles will be discussed from this point forward. To make it easier to go through the results, these cycles are numbered from #1 to #8.

5.1 Grid Independence and Accuracy

The crank angle resolved total cell count is presented in Figure 5.1. The effects of fixed embedding and AMR are clearly visible in this figure, where there is a spike in the cell count right before the spark timing at -12 CAD, and also in the random changes in the number of cells in the rest of the simulation. What is interesting, is that despite having the max number of cells limited to 3×10^6, the limit has not reached at any point. This implies the independence from the grid size in the solution, as the gradients were not high enough to more refine the grid.

As mentioned earlier, y^+ should be looked at to make sure the grid is fine enough to properly capture the wall effects in turbulent flows. In the simulations, the following ranges of y^+ were observed on different walls:

- Intake manifold: 70-120

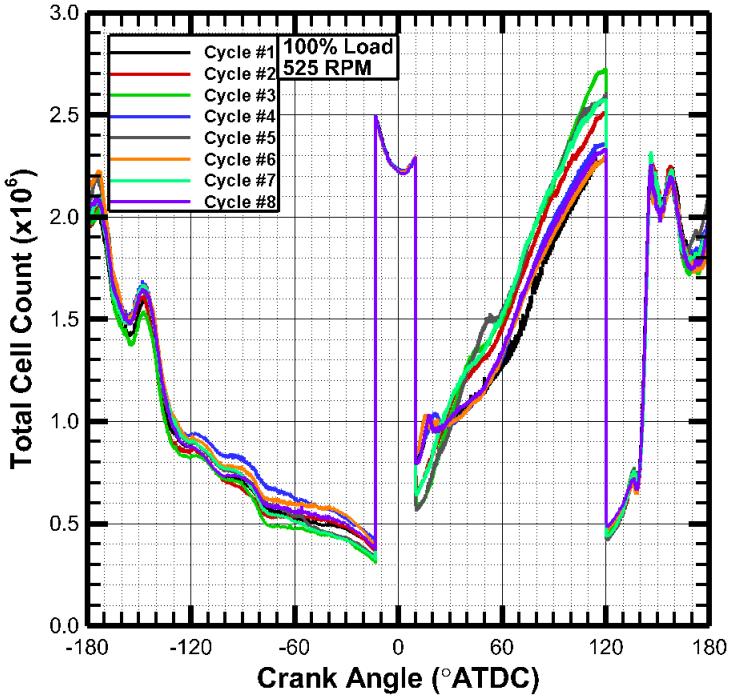

Figure 5.1: Total cell count

- Exhaust manifold: 80-350
- Liner: 30-100
- Spark plug: 25-40
- Cylinder head: 30-280

It can be seen that almost all the y^+ values are above the minimum acceptable range, which means that the simulation is properly capturing the wall effects on the flow field.

To check the possibility of refining the grid near the boundaries to get better y^+ values, the results of flow field calculations were mapped to only the geometry of the combustion chamber right after EPC. The number of layers and the level of embedding near the walls were increased by one; additionally, the embedding level near the spark plug was increased by one. With these modifications, because of the huge size of the engine, the number of

cells only in the combustion chamber skyrocketed to almost 16×10^6, making it impossible to run the simulation in a reasonable time.

5.2 Reed Valve Simulation Results

The next step was the simulation of the reed valve, and validation of its results. The validation criteria are the proper simulation of the reed valve behavior, matching of the stuffing box pressure, and finally proper control of the air fuel ratio in the stuffing box.

As shown for the measured boundary conditions, it is important to show that the measured pressures of the stuffing box do not vary too much from one cycle to another. For this reason, five randomly selected individual cycles and an average of 300 cycles were plotted; the results are presented in Figure 5.2. It is clearly visible that the variations are minimal.

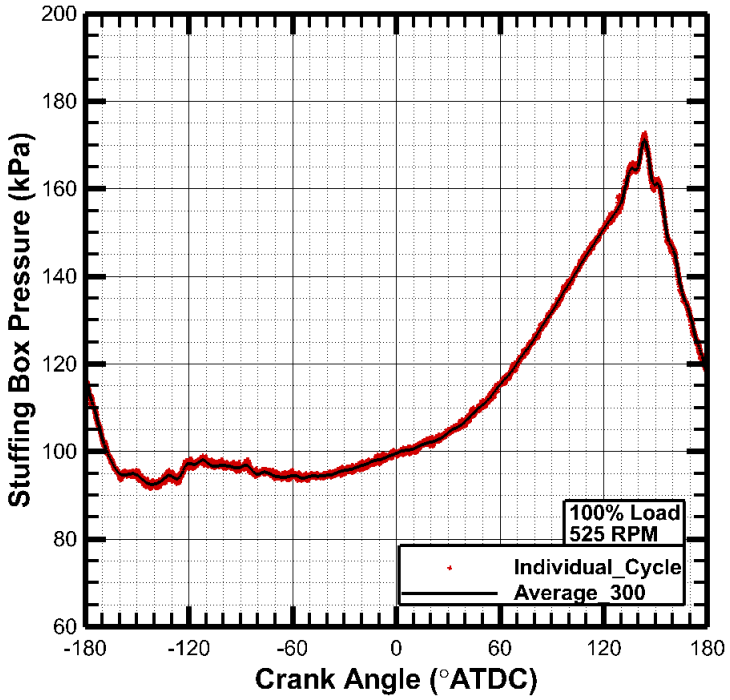

Figure 5.2: Variations of the stuffing box pressure

As mentioned in section 4.2.6, crank angle resolved pressure curves were used as boundary conditions for the simulation. In order to show the importance of using experimentally acquired boundary conditions, two cases are compared: 1) a case with constant pressure for air and fuel boundary conditions, and 2) a case where previously shown experimental pressure curve where used as boundary conditions. The results are presented in Figure 5.3. It can be seen how important is the use of experimentally acquired boundary conditions, for the simulation using the FSI. In addition, the close matching of the simulated and experimental stuffing box pressure validates the FSI results.

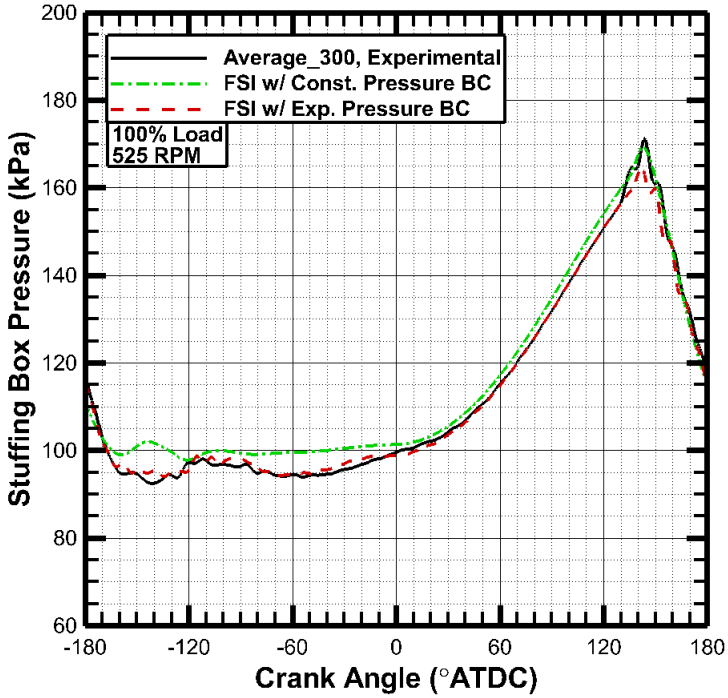

Figure 5.3: Simulated stuffing box pressure using FSI, vs. experimental data

Another criterion that has to be met to validate FSI results is capturing the behavior of the reed valve strips as was shown in Figure 4.12. Interestingly, the numerical simulation

captures the same fluttering behavior. The results are presented in Figure 5.4. It can be seen that all the strips start to open at -160 °ATDC, and show different motion profiles. It also is clear that there are more than one open/close event within one cycle, as was observed experimentally. It should be noted that strips #1, and strip #5 have only air pressurizing their top surfaces, while strip #3 has both air and fuel pressures on its top surface.

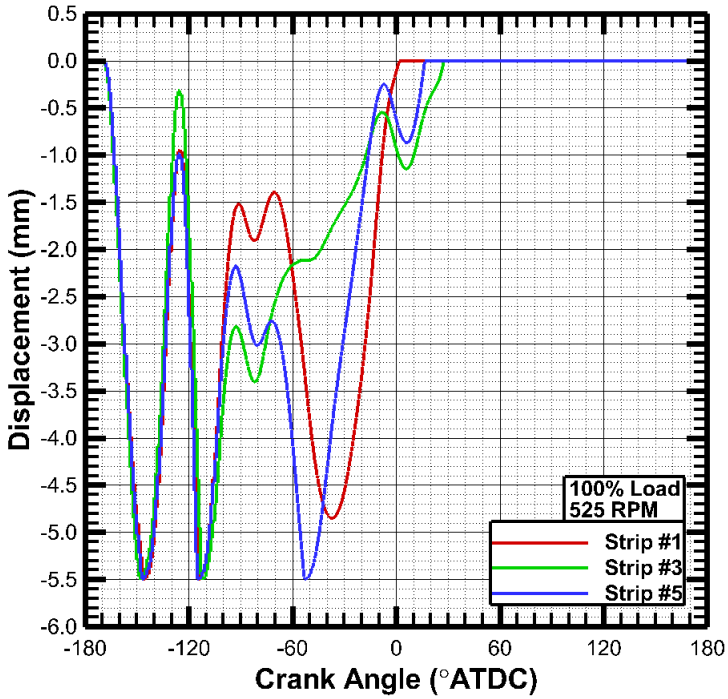

Figure 5.4: Displacement of the strips #1, #3, and #5 vs. crank angle for one cycle

The next validation criterion is the ability of the model to keep the stuffing box air fuel ratio close to the experimentally acquired values. Thorough experiments it has been shown that the equivalence ratio (ϕ) of the stuffing box should be approximately 0.81. As presented in Figure 5.5. It can be seen that despite minor changes in the stuffing box's equivalence ratio, the model is capable of keeping it reasonably stable.

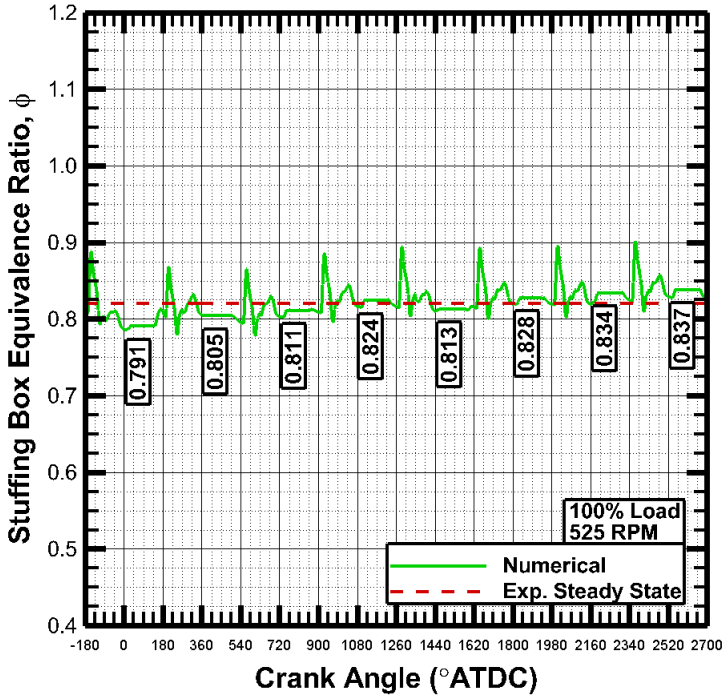

Figure 5.5: The simulated equivalence ratio of the stuffing box

5.3 Combustion Simulation Results

The next and most important criterion to validate the simulation results, is matching the pressure in the combustion chamber. This task usually starts with matching the motoring curve of the engine, with a simulated motoring curve; this helps confirm that the clearance volumes are the same. Unfortunately, because of the big size of the engine, a huge electric motor is required to turn the engine to capture the motoring curve experimentally; this electric motor is not yet available for testing. To overcome this problem, as was shown in Figures 4.7 and 4.8, a silicone mold was made to measure the clearance volume; using this experimentally measured volume, the piston location was set in numerical simulations in such a way that the simulations would capture the same V_c.

Relying on this confirmation, the simulations started and the simulated pressure of the

chamber was compared with the experimental data. Before presenting the comparison, it is important to mention that the engine is prone to cyclic variation. Cyclic variation simply means variation in the performance of the engine, from one cycle to the next. Cyclic variation can be qualitatively observed through combustion chamber pressure curves, as presented in Figure 5.6. It can be seen that increasing speed generally increases the cyclic variation, while increasing load, significantly reduces cyclic variation. [67]

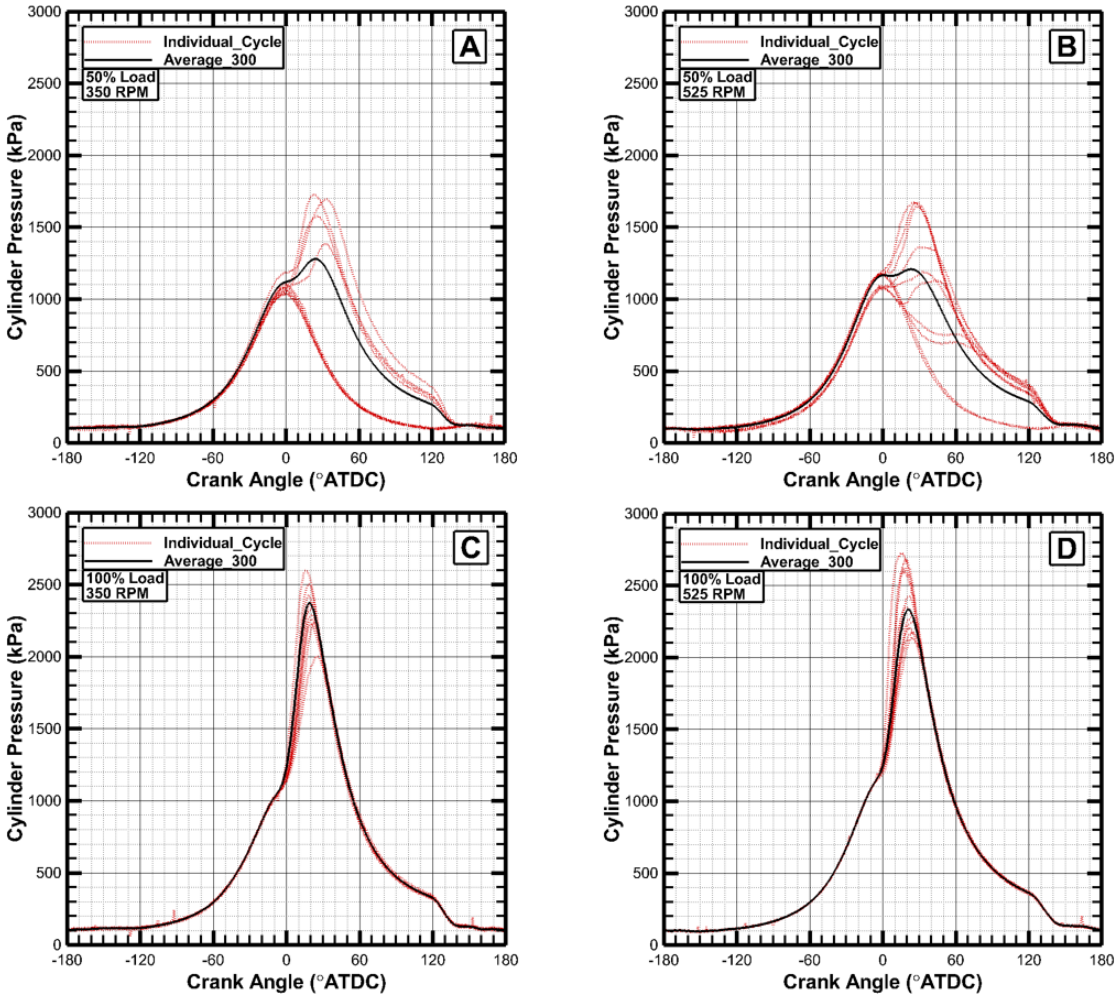

Figure 5.6: Measured individual cycles and 300-cycle-averaged in-cylinder pressures for (A) 350 RPM and (B) 500 RPM at 50% load and (C) 350 RPM and (D) 500 RPM at 100% load.

This same phenomenon can be quantified by coefficient of variability of IMEP (COV_{IMEP}), which is defined in Equation 5.1:

$$COV_{IMEP} = \frac{\sigma_{IMEP}}{IMEP_{average}} \tag{5.1}$$

Where σ_{IMEP} is the standard deviation of the IMEP over a sample of 300 cycles. In this equation, IMEP will be calculated from Equation 5.2:

$$IMEP = \frac{\sum_{i=1}^{N} P_i \Delta V_i}{V_d} \tag{5.2}$$

In which, ΔV_i is the volume difference between two encoder readings, and V_d is the displacement volume. Using Equation 5.1, the COV_{IMEP} for different load and speed conditions were calculated, and the results are listed in Table 5.1.

Table 5.1: COV_{IMEP} for different load and speed conditions

		Speed (RPM)	
		350	525
Load (% Full Load)	50	69.3%	83.9%
	100	1.6%	1.8%

Considering the huge COV_{IMEP} present in this engine, comparing the chamber's simulated pressure with the experimental data is not easy; it just has to be confirmed that the compression part of the cycles perfectly match, and that the simulated pressure curve is within the range of cyclic variation of the engine through the rest of the cycle. These results are presented in Figure 5.7. It can be seen that the simulated pressure of the chamber (in purple) matches very closely with the experimental data during the compression part of the cycle, and is within the range of the cyclic variation of the engine (red lines). This

plot validates the results of the simulation of the combustion chamber.

A study of cyclic variation was carried out as a side-project; the results are presented in more detail in APPENDIX B, CYCLIC VARIATION.

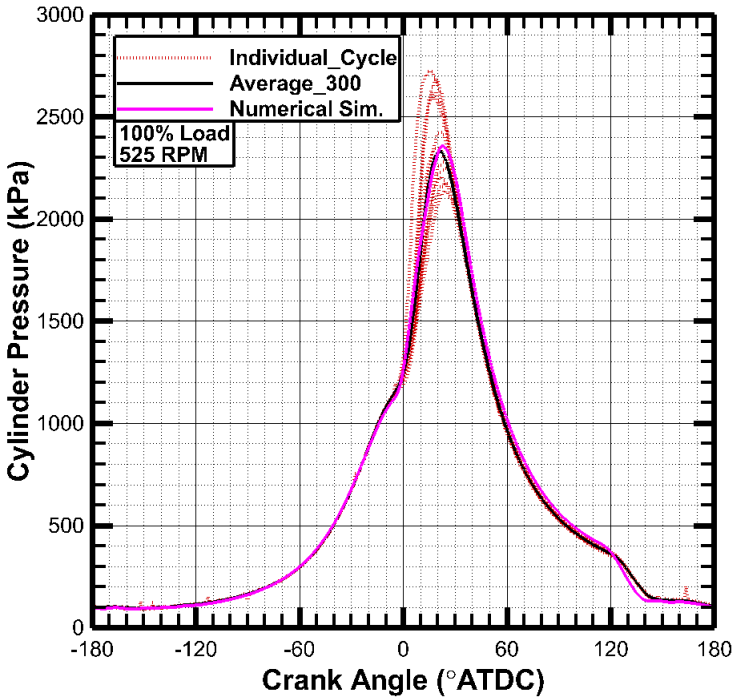

Figure 5.7: Validation of the simulated chamber pressure with experimental data

5.4 Gas Exchange Process Results

The validated simulation results were then used to look at different important variables in the engine. Gas exchange process, is one of the most important processes in a two-stroke engine. [1] To quantify this process, trapping efficiency, short-circuiting percentage, and scavenging efficiency are calculated.

Trapping efficiency is the ratio of the fresh charge trapped in the chamber, to the total mass of the fresh charge delivered during the scavenging process, and can be calculated

using Equation 5.3:

$$\eta_{tr} = \frac{\text{mass of trapped fresh charge}}{\text{mass of delivered fresh charge}} \tag{5.3}$$

Short-circuiting percentage is simply $1 - \eta_{tr}$, and represents the ratio of the fresh charge that leaves the chamber during the scavenging process through the exhaust ports to the total fresh charge delivered.

Based on simulations (as presented in Figure 5.8) the combustion efficiency is almost 100%, because the mass of CH_4 goes all the way down to zero during the combustion event, and before EPO. This means that all the trapped fuel inside the chamber burns during the combustion event. This is a valid assumption, since the engine runs lean of stoichiometric mixture. Having this in mind, it can be concluded that all the CH_4 that is being transferred from the chamber to the exhaust manifold, is due to short-circuiting, and the ratio of this amount to the total mass of CH_4 that has entered the chamber from the stuffing box will be the short-circuiting percentage.

Figure 5.9 shows the total mass of CH_4 transferred from the stuffing box to the chamber (delivered fuel), and from the chamber to the exhaust manifold (short-circuited fuel); the differences between the total value of each cycle and the previous cycle are the transferred masses of that cycle, and the short-circuiting percentage can be calculated from these values. The calculated η_{tr} and short-circuiting percentage values are listed in Table 5.2.

Scavenging efficiency is the ratio of the fresh charge trapped in the chamber, to the total trapped mass of the chamber, and can be written as Equation 5.4:

$$\eta_{sc} = \frac{\text{mass of trapped fresh charge}}{\text{trapped mass of the chamber}} \tag{5.4}$$

Using the values listed in Table 5.2, and the total mass transferred from the stuffing box to the chamber for each cycle as presented in Figure 5.10, the mass of trapped fresh

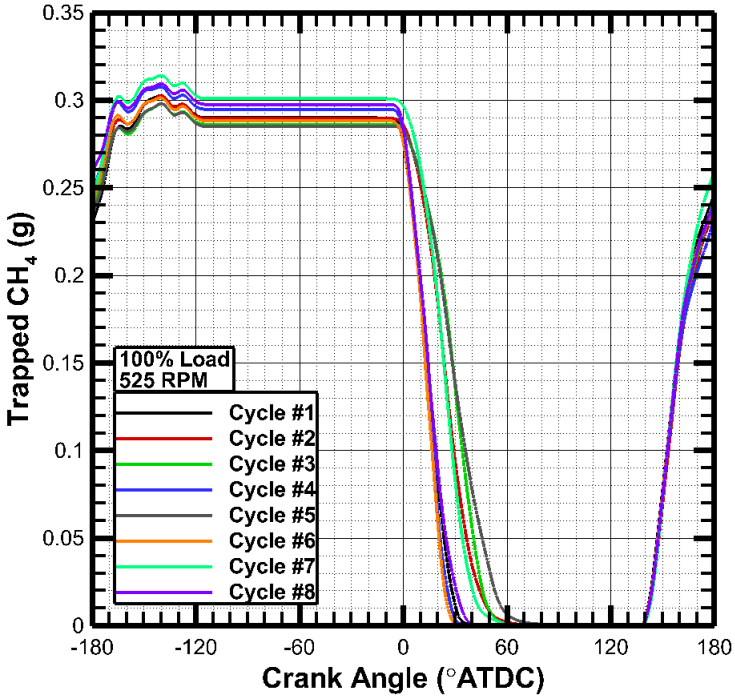

Figure 5.8: Trapped CH_4 in the chamber for different cycles

charge can be calculated. In addition, Figure 5.11 shows the total trapped mass inside the chamber. Using these two values, and Equation 5.4, η_{sc} values were calculated, and are listed in Table 5.3.

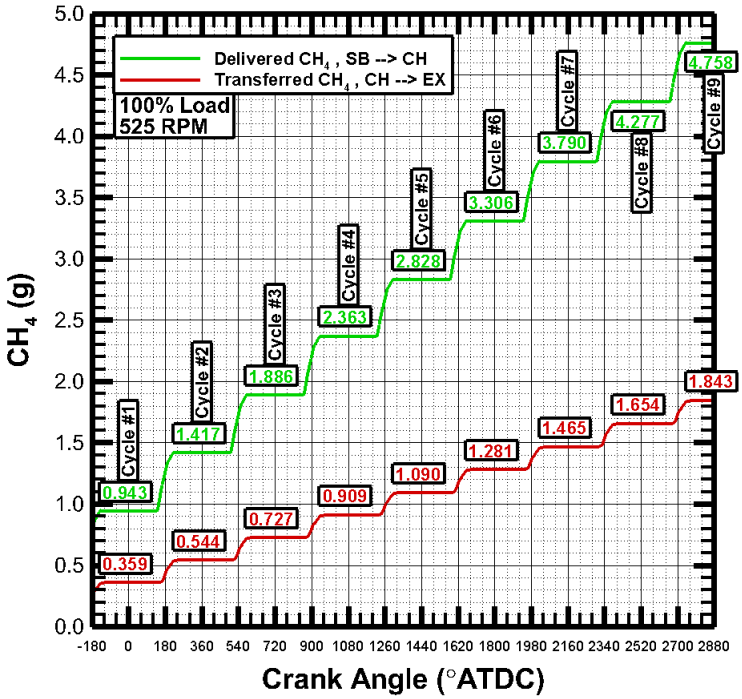

Figure 5.9: CH_4 transferred from stuffing box to chamber, and from chamber to exhaust manifold

Table 5.2: Short-circuiting percentage and trapping efficiency (η_{tr})

	Short-circuiting (%)	η_{tr} **(%)**
Cycle #1	39.03	60.97
Cycle #2	39.02	60.98
Cycle #3	38.16	61.84
Cycle #4	38.92	61.08
Cycle #5	39.96	60.04
Cycle #6	38.02	61.98
Cycle #7	38.81	61.19
Cycle #8	39.23	60.71

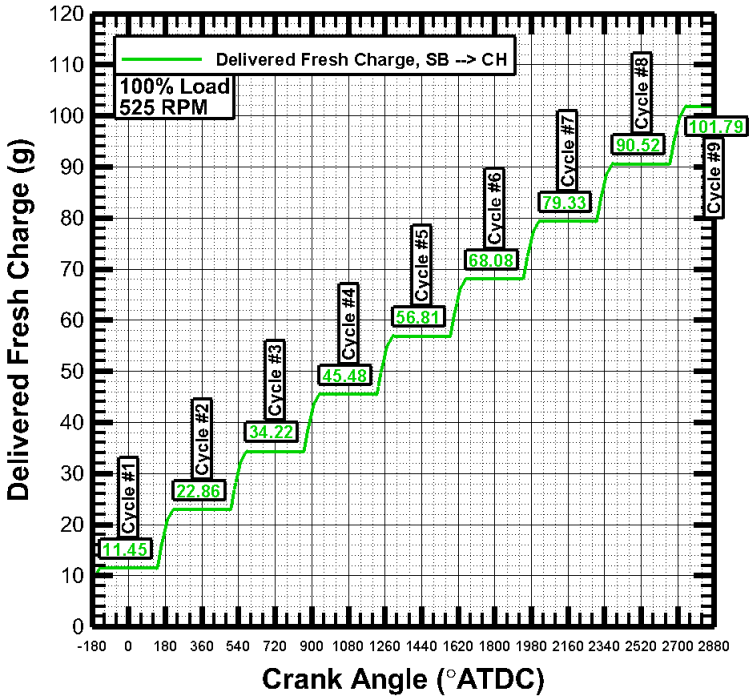

Figure 5.10: Total mass transferred from the stuffing box to the chamber

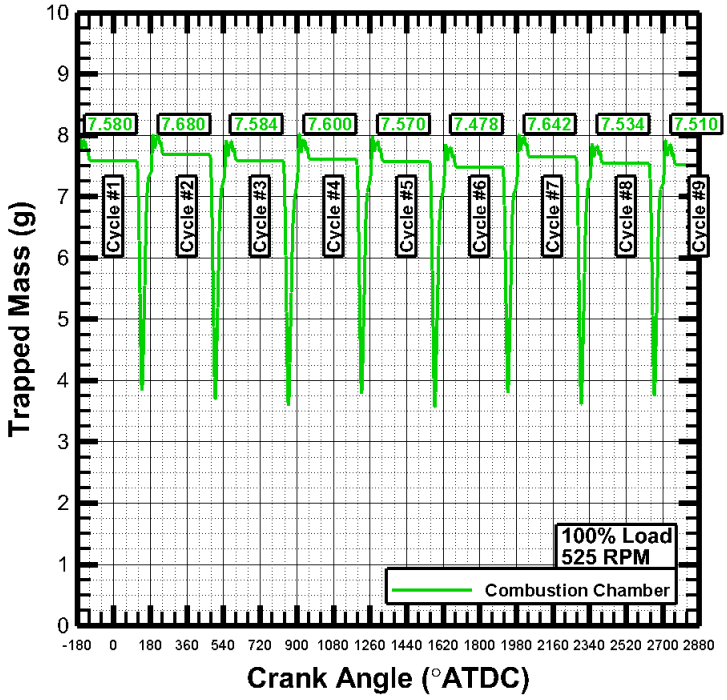

Figure 5.11: Total trapped mass of the chamber

Table 5.3: Scavenging efficiency (η_{sc})

	Delivered Fresh Charge (g)	η_{tr} **(%)**	**Retained Fresh Charge (g)**	**Trapped Mass (g)**	η_{sc} **(%)**
Cycle #1	11.410	60.97	6.957	7.680	90.58
Cycle #2	11.360	60.98	6.927	7.584	91.34
Cycle #3	11.260	61.84	6.963	7.600	91.62
Cycle #4	11.330	61.08	6.920	7.570	91.42
Cycle #5	11.270	60.04	6.767	7.478	90.49
Cycle #6	11.250	61.98	6.973	7.642	91.24
Cycle #7	11.190	61.19	6.847	7.534	90.88
Cycle #8	11.270	60.71	6.842	7.510	91.11

5.5 Conjugate Heat Transfer Simulation

For this purpose, the geometry of the cylinder block, and the cylinder head were required. These geometries were obtained, and prepared for the simulation work, as presented in Figure 5.12. It can be seen that coolant enters the cylinder block, absorbs the heat from the combustion chamber, and then exits from the top side of the cylinder head because of the density gradients that drive the coolant.

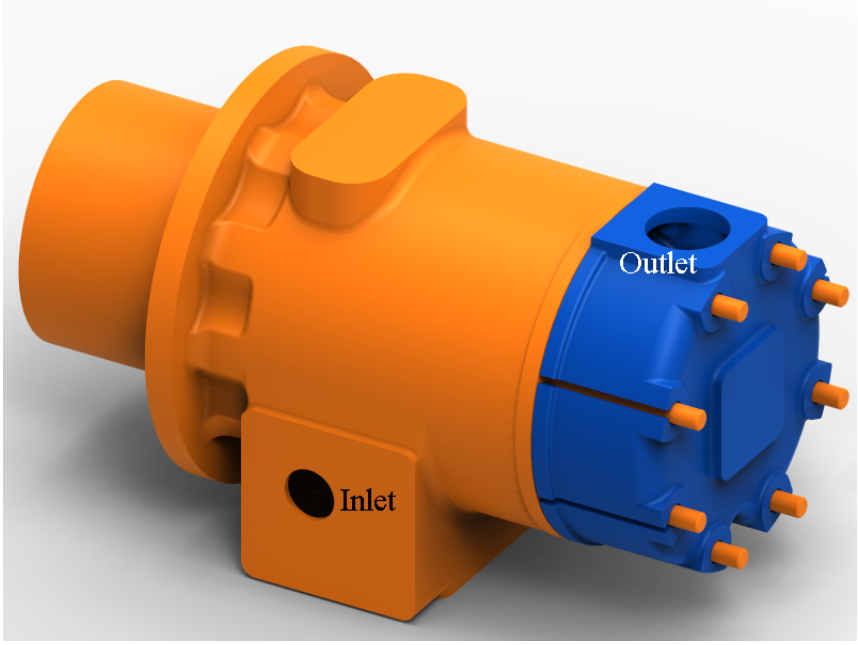

Figure 5.12: Geometry of the cylinder block (orange), and the cylinder head (blue)

Figure 5.13 helps visualize the coolant path inside the cylinder block, and the cylinder head. It can be seen in this figure, how the coolant enters the cylinder block, covers the sides of the liner, then moves inside the cylinder head, and exits from the top of the head.

In addition to Figure 5.13, looking at Figure 5.14 might help justify the results. In this figure, it can be seen how the coolant completely covers the area around the exhaust

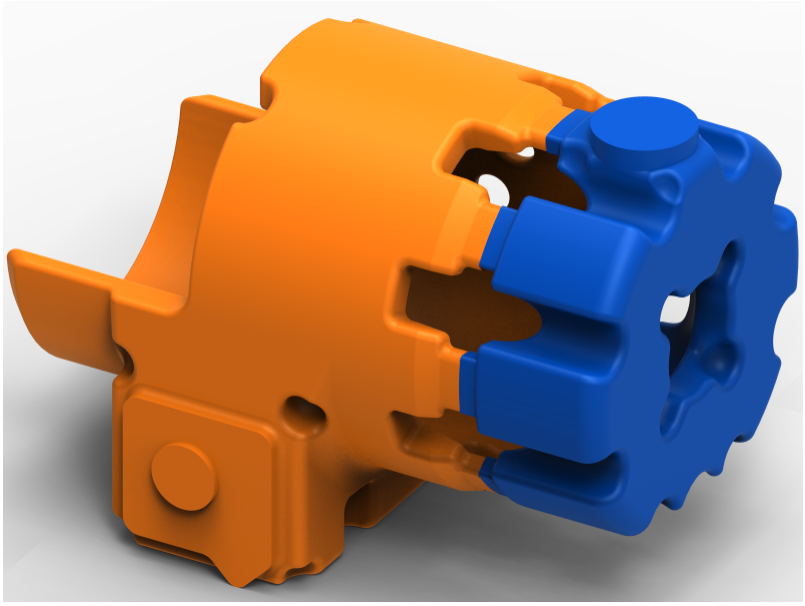

Figure 5.13: Geometry of the coolant path inside the cylinder block (orange), and the cylinder head (blue)

manifold, and then moves towards the cylinder head. It also has to be noted that the coolant path does not properly cover the area around the air-start cavity, and the spark plug, which probably are the hottest zones of the cylinder head, as will be shown.

5.5.1 The Simulation Process

An iteration between the combustion simulation and the CHT simulations was started. Super-Cycling method was used for the simulation of the conjugate heat transfer between the engine's solid parts (cylinder block and cylinder head), and its cooling system. These steps were taken to carry out this part of the simulation work:

1. The combustion simulation with the assumption of constant wall temperatures was ran, until all variables converged.
2. Spatially resolved convective heat transfer coefficients and gas temperatures on the vicinity of the combustion chamber walls were temporally averaged. These values

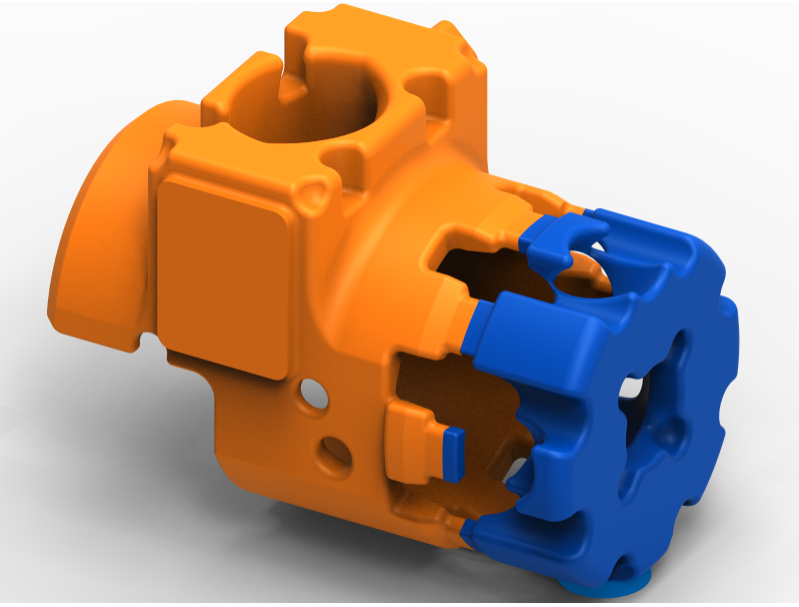

Figure 5.14: Upside down geometry of the coolant path inside the cylinder block (orange), and the cylinder head (blue)

were mapped to the CHT simulation, and used as boundary conditions.

3. The CHT simulation with newly acquired boundary conditions was carried out, until all temperatures converged. Temperatures of the walls interfacing with the combustion chamber were extracted to then be used as boundary conditions for the combustion simulation of the next step.

4. A new combustion simulation was started with the new boundary conditions.

5. This process was iterated a few times, until all temperatures were converged.

Boundary and Initial Conditions

As mentioned before, the convective heat transfer coefficients and gas temperatures close to the combustion chamber walls were used as boundary conditions around the combustion chamber for the CHT simulations. These two sets of boundary conditions for the

first iteration are presented in Figure 5.15 (A) and (B). A look at the convective heat transfer coefficients, reveals that the values are higher close to the intake ports, and at the neck of the air-start cavity. Near-wall gas temperatures, on the other hand, are obviously higher in the cylinder head area, where the combustion starts; the values are much higher around the spark plug, and also around the neck of the air-start cavity.

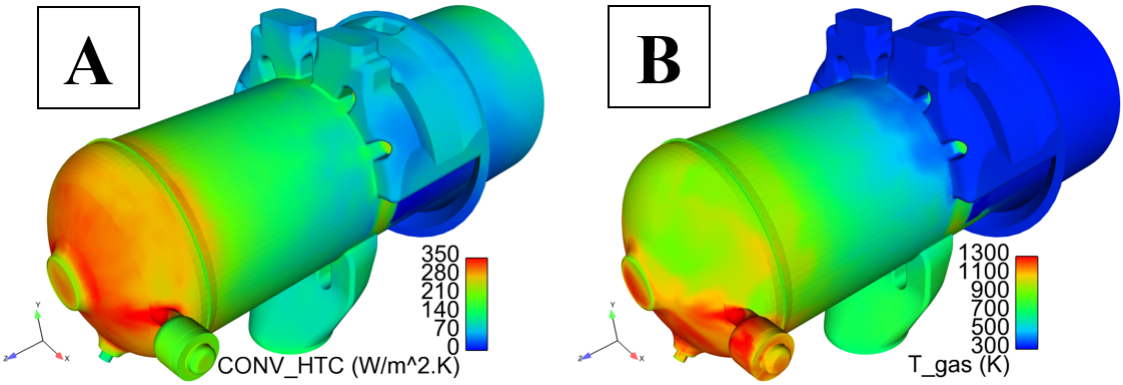

Figure 5.15: Temporally averaged, spatially resolved (A) convective heat transfer coefficients, (B) near-wall gas temperatures

The convective heat transfer coefficient is calculated using the law-of-the-wall correlation given by Amsden in 1997 [72, 79]. The estimated heat flux as presented in Equation 5.5 is used to calculate the convective heat transfer coefficient:

$$q'' = h(T_f - T_w) = \frac{\mu_m c_p F (T_f - T_w)}{\mathrm{Pr}_m y} n_i \Rightarrow h = \frac{\mu_m c_p F}{\mathrm{Pr}_m y} n_i \tag{5.5}$$

In which,

$$F = \begin{cases} 1.0 & \mathrm{y}^+ < 11.05 \\ \frac{(\frac{\mathrm{y}^+ \mathrm{Pr}_m}{\mathrm{Pr}_t})}{\frac{1}{\kappa}\ln(\mathrm{y}^+) + B + 11.05(\frac{\mathrm{Pr}_m}{\mathrm{Pr}_t} - 1)} & \mathrm{y}^+ > 11.05 \end{cases} \tag{5.6}$$

Where $y^+ = \frac{\rho u_\tau y}{\mu_m}$, κ is equal to 0.4187 (the Von Karman constant), B equals to $u^+|_{y^+=1}$, Pr_m and Pr_t are the molecular and turbulent Prandtl numbers respectively, wall and fluid temperatures are shown by T_w and T_f respectively, and finally, u_τ, which stands for the shear speed is put in from the momentum law-of-the-wall.

The initial temperature for the coolant and also the coolant inlet temperature were set from the experimental data, to 318 K. The coolant flowrate has been measured to be 2.5 gpm (≈0.16 kg/s) and has been set in the numerical simulations accordingly. [69]

To assess the effects of using various coolants, the simulations were done for two different cases:

- Pure water as coolant (will be called 'W' from this point forward).
- A mixture of water and ethylene glycol with a 50/50 volumetric ratio as coolant (will be called 'W/EG' from this point forward). This mixture has lower specific heat and heat conductivity than pure water. This means that it is expected to have higher temperatures in the solid parts of the engine when this mixture is used as coolant compared to the temperatures of the parts with pure water as coolant.

It should be noted that temperature-dependent properties were used for both coolants to increase the accuracy of the simulations.

5.5.2 CHT Results

The results of the CHT simulations are presented in this section.

Grid Independence

The first criterion to make sure that the numerical simulation results are accurate and reliable, is to make sure that the results do not depend on the grid size. For this purpose, three sets of simulations were ran with various grid sizes: 5 mm, 3 mm, and 2 mm. The average temperatures of the solid (cylinder block and cylinder head) and fluid (coolant)

regions were then compared to check for grid independence. The results are presented in Figure 5.16. It should be noted that the grid independence study was carried out only with pure water as coolant.

In this figure it can be seen that the average temperatures converge after almost 200 seconds. In addition, it can be seen that for the solid parts, $\Delta T_{5\text{mm}\rightarrow 3\text{mm}} = 14$ K, and $\Delta T_{3\text{mm}\rightarrow 2\text{mm}} = 3$ K. On the other hand, for the coolant, $\Delta T_{5\text{mm}\rightarrow 3\text{mm}} = 1.6$ K, and $\Delta T_{3\text{mm}\rightarrow 2\text{mm}} = 0.9$ K. The small variations between the mean temperatures of the 3 mm and 2 mm cases, confirm that the CHT simulations are independent of the grid size at this point.

The simulations were parallelized and ran on 320 cores. The 2 mm grid size case took almost 7 wall-clock days to converge; whereas, the 3 mm case took only 3 days. Since the results did not change much between the two cases, and the simulation time was significantly shorter for the 3 mm case, all the rest of the simulations were ran utilizing a grid size of 3 mm.

After establishing the grid independence of the results, the iterative process between the CHT simulation and the combustion simulation started. The results of these simulations are presented in the following sections.

Average Temperatures

Average temperatures of the solid and fluid regions were compared from one iteration to the next, to check the convergence of the aforementioned iterative process. The results for the case with pure water as coolant are presented in Figure 5.17. It can be seen that the differences between the iteration 3 and 4 temperatures are very small; for the coolant, $\Delta T_{iter\_3\rightarrow iter\_4} = 0.8$ K, while for the solid parts, $\Delta T_{iter\_3\rightarrow iter\_4} = 1.9$ K. These very small changes in the average temperatures prove that the iteration process has converged to its final values.

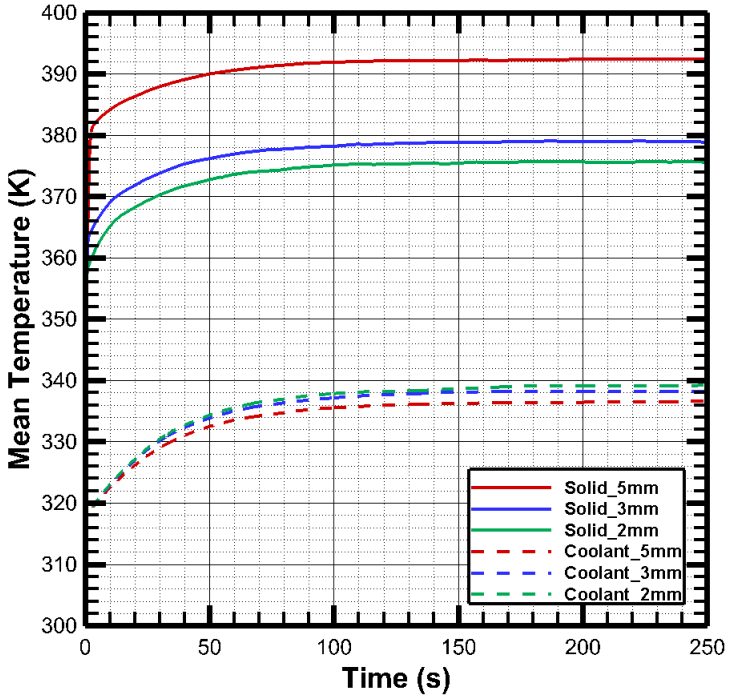

Figure 5.16: Grid independence study for the CHT simulations

The same simulations were carried out with W/EG as coolant; the results are presented in Figure 5.18. It is again very clear how minimal the changes are between the mean temperatures for iterations 3 and 4; for the coolant, $\Delta T_{iter\_3 \rightarrow iter\_4} = 0.01$ K, while for the solid parts, $\Delta T_{iter\_3 \rightarrow iter\_4} = 0.4$ K. These very small changes once again prove that the simulations have converged to their final values.

An interesting observation from the results is that the mean temperatures of the two coolants are not that different (≈ 2 K), while the mean temperature of the solid regions are higher (≈ 22 K) for the simulation with W/EG. This totally makes sense, since the heat conductivity and capacity of this mixture are lower than those of pure water.

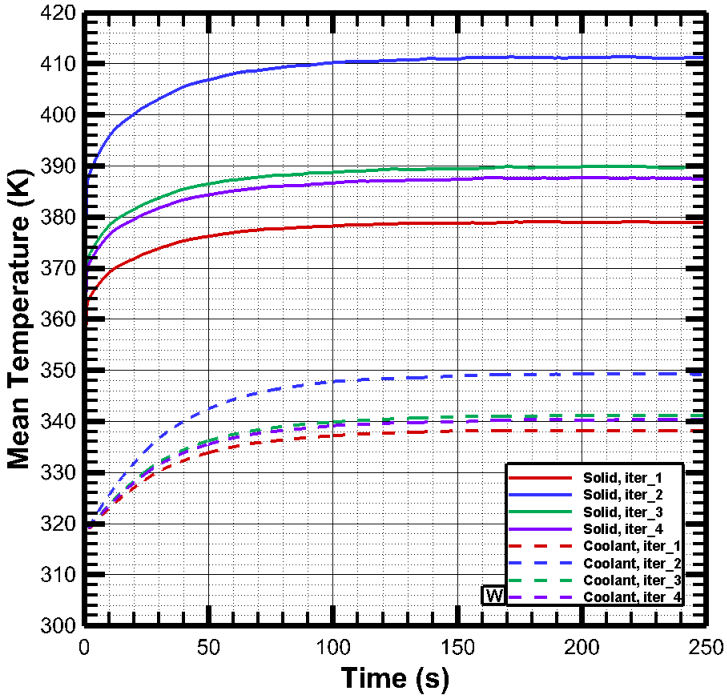

Figure 5.17: Mean temperature of the solid and fluid regions for different iterations with pure water as coolant

Temperatures at Monitor Points, and Experimental Validation

Another validation criterion to check the convergence of the iteration process is to look at individual monitor points around the engine. For this purpose, a few points were selected around the liner and were monitored for changes. These points are shown in Figure 5.19 (A). As visible in this figure, points #1 and #2 are between the coolant path and the liner on the intake side of the chamber; points #3 and #4 are between the coolant path and the liner on the exhaust side of the chamber; point#5 is on top of the cylinder head; and finally point#6 is behind the spark plug.

The results are presented in Figure 5.20. It can be seen that for all the points, the temperatures with pure water are lower than those of W/EG mixture. It also can be seen that changes in local temperatures for almost all the points are minimal; these changes are

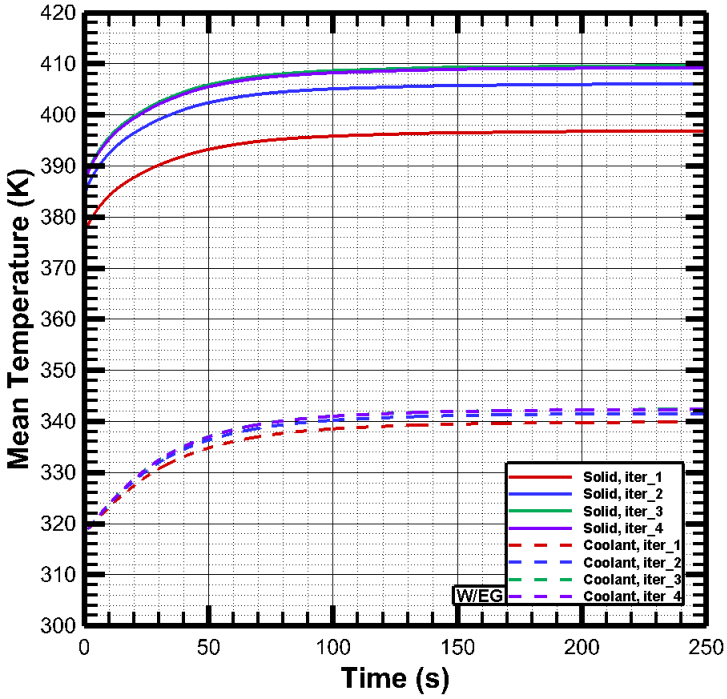

Figure 5.18: Mean temperature of the solid and fluid regions for different iterations with W/EG as coolant

Table 5.4: $\Delta T_{iter\_3 \rightarrow iter\_4}$ (K) for local monitor points

	Point#1	Point#2	Point#3	Point#4	Point#5	Point#6
Water	4.5	6	10	8	0.5	10
W/EG	2.3	4.2	1.8	1.5	2.1	3.6

listed in Table 5.4. This again confirms the convergence of the iteration process. On the other hand, these minor changes can be explained by changes in in-cylinder pressure as shown in the following section.

In addition to all these, there is a through-hole which can be used for additional lubrication on the side of the engine; it can be seen in Figures 4.5 and 5.14. This point can be used to make an experimental temperature measurement. A plug was made to fill the hole flush with the liner, and a fast-response type-K thermocouple was fitted tightly in this

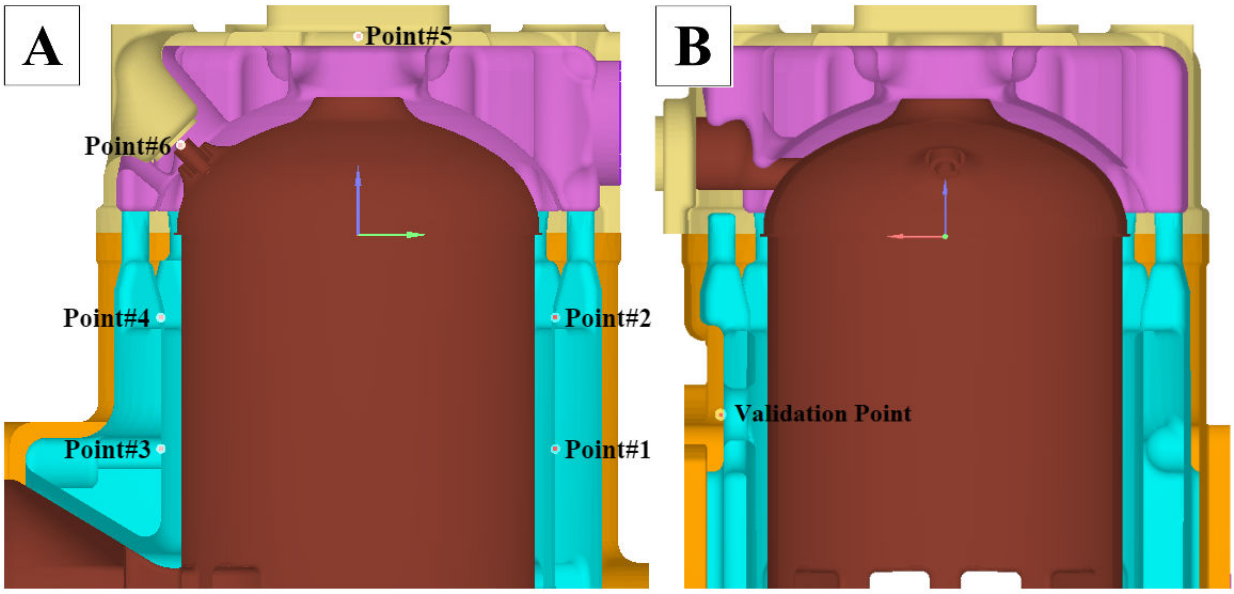

Figure 5.19: Location of monitor points: (A) used for convergence check, (B) used for experimental validation

plug at a certain distance from the liner surface (Figure 5.21). The transient heat penetration depth was calculated to make sure the point of measurement is not seeing the transient heat transfer behaviors The engine was ran at full-load, rated-speed for 30 minutes to reach steady-state, and then the temperature was measured to be $\approx$ 120 °C (393 K). It has to be noted that the experiment was done only with W/EG as coolant.

A monitor point was put at this same location in the simulations (Figure 5.19 (B)), and temperatures were compared. The results are presented in Figure 5.22, where the black line represents the steady state temperature measurement at the mentioned point. It can be seen that the simulated temperature with pure water as coolant is below the measured temperature, while with W/EG as coolant it is very close to the experimentally measured temperature. Although many other points should be used for experimental validation, there are not many places on the engine that are accessible for temperature measurements. This single validation point, adds to the reliability of the simulation data.

Pressure Curves

In this section, the effects of combustion chamber wall temperatures on in-cylinder pressures are studied. As shown in Figure 5.23, changes in wall temperatures affect the

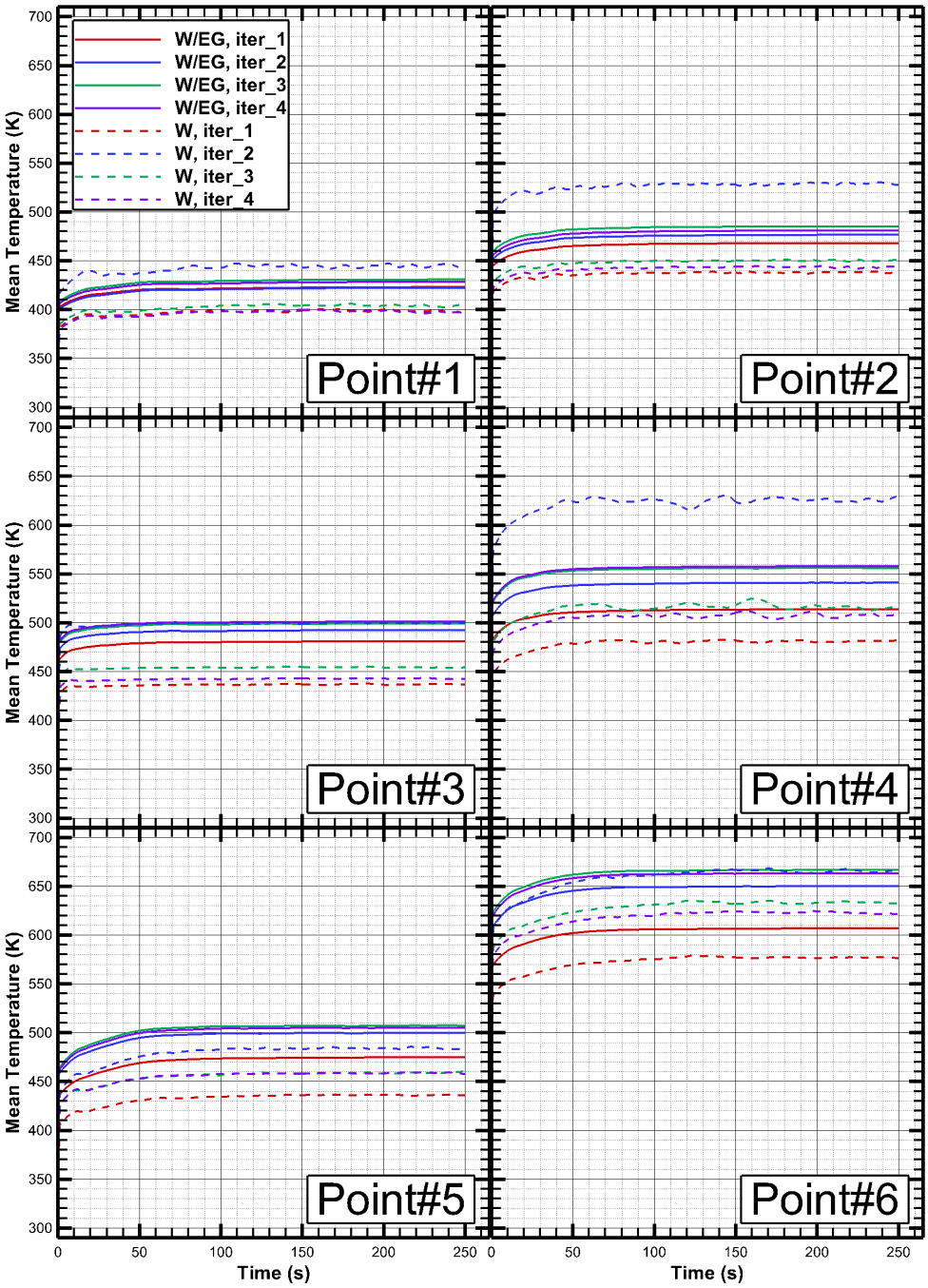

Figure 5.20: Local temperature at shown monitor points

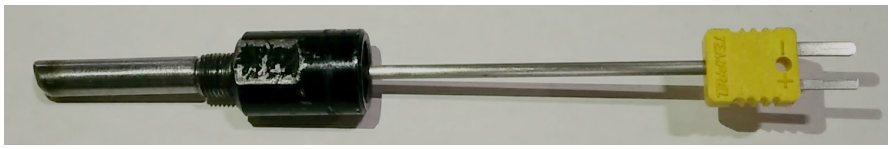

Figure 5.21: The plug and thermocouple used for the validation of CHT simulations

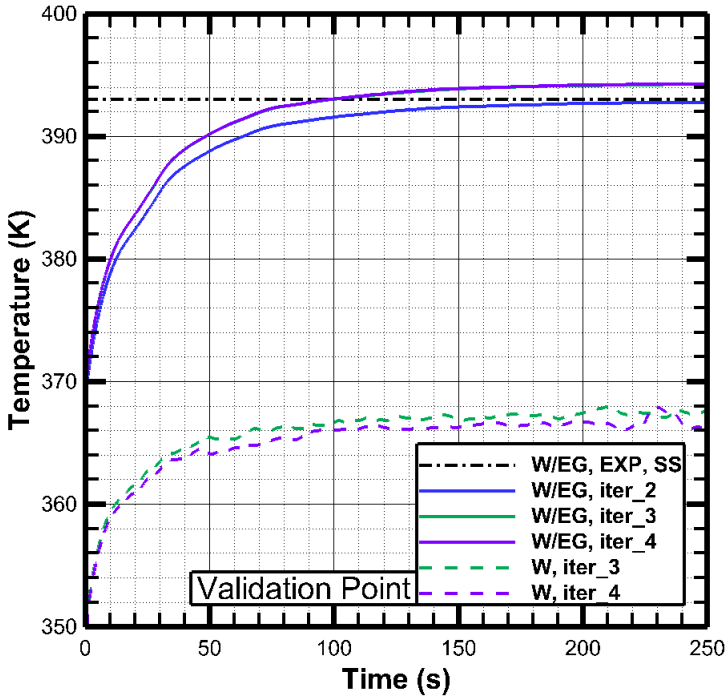

Figure 5.22: Comparison of experimental and numerical temperatures at the validation monitor point

in-cylinder pressures. This phenomena can be due to various reasons:

- Slightly different in-cylinder pressure at EPC timing. These small differences will be magnified when combustion starts.
- Different wall temperatures, could potentially change the combustion characteristics of the cycle. The changes in the combustion behavior could lead to different flame propagation characteristics. The rate of heat release (ROHR) curves can be used to

show this difference.

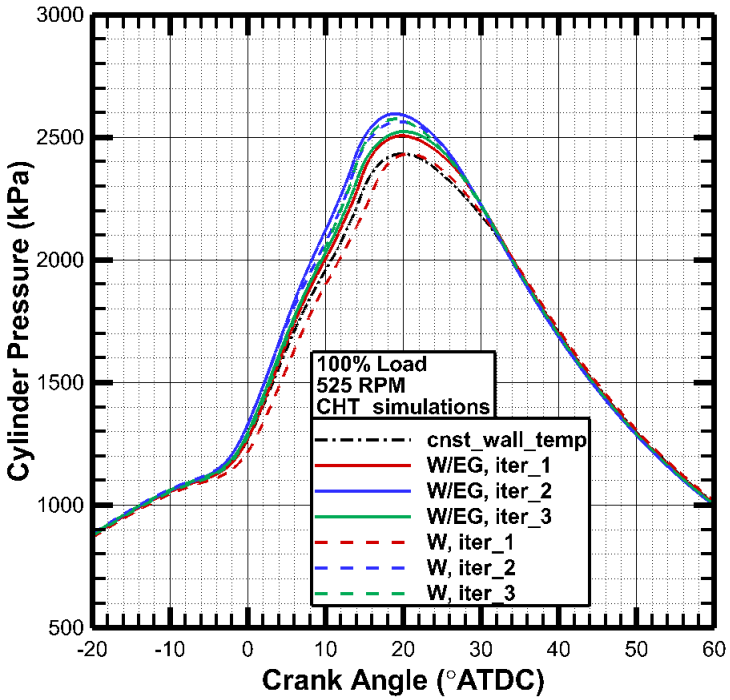

Figure 5.23: In-cylinder pressures with different wall temperatures

As mentioned, ROHR curves can be used to look at different combustion characteristics. It can be seen in Figure 5.24, that the net heat release for all the simulated cycles is almost constant, meaning that the trapped fuel, and the total released energies are identical. On the other hand, Figure 5.25 shows how different the ROHR curves look like for different wall temperatures. This means that the combustion characteristics are not the same between the cycles; these differences can be due to minor variations in the wall temperatures. In this figure, the difference in the slopes of the ROHR curves and the peak values is evident.

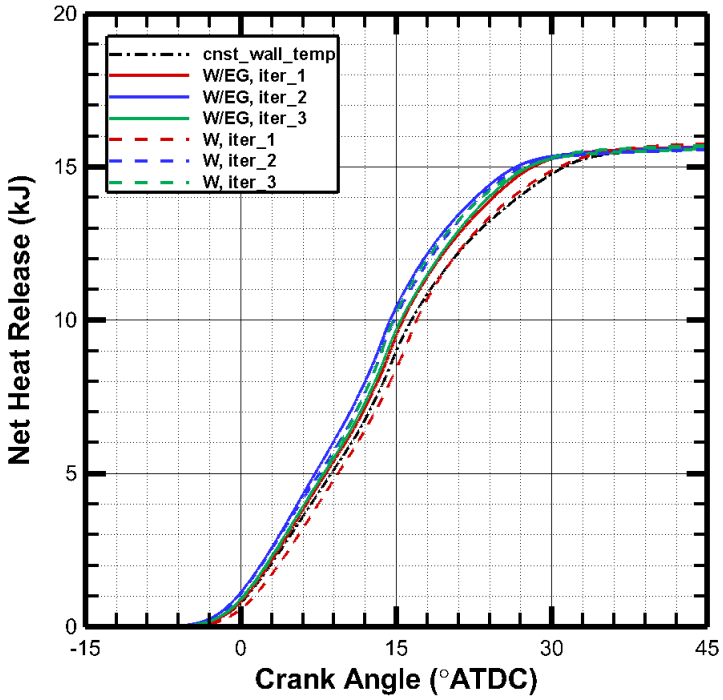

Figure 5.24: Net heat release for cycles with different wall temperatures

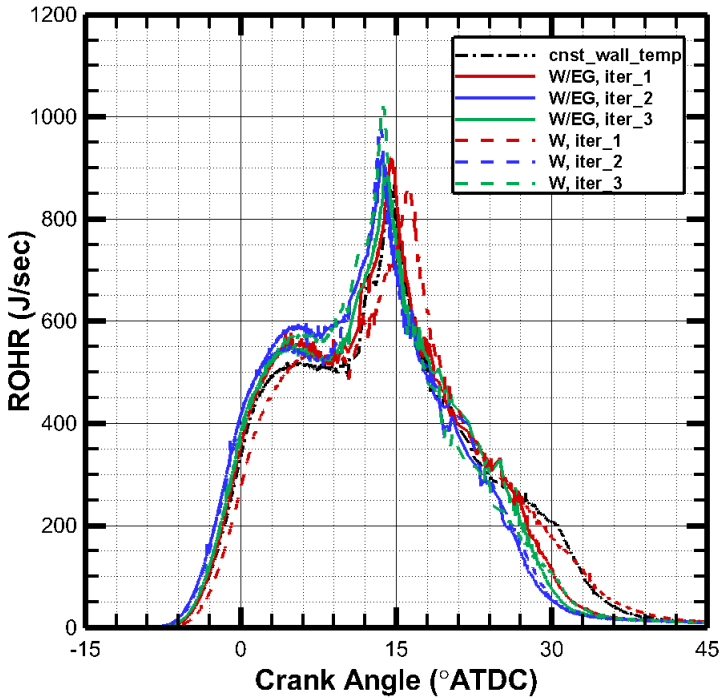

Figure 5.25: Rate of heat release (ROHR) for cycles with different wall temperatures

Temperature Distribution on the Combustion Chamber Walls

The last piece of results that can be looked at is the temperature distribution on the parts interfacing with the combustion chamber; achieving this, is the objective of the study. The overall temperature distribution on the combustion chamber walls is shown in Figure 5.26.

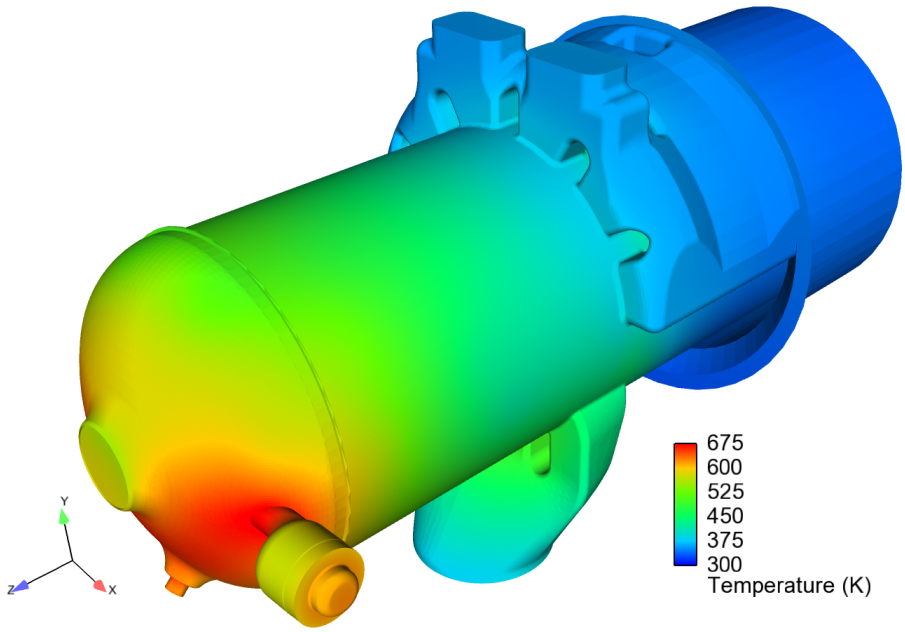

Figure 5.26: Overall temperature distribution on the combustion chamber walls

A few interesting observations can be made from this figure. The first point is that the temperature around the exhaust manifold is significantly lower than those of the cylinder head, the spark plug, and the air-start cavity. This has two main reasons:

- The gas temperatures inside the chamber are much lower at EPO, than they are at the peak temperature and pressure of the combustion chamber. This means that the fluids are much cooler, when exhaust port opens to let the combustion products out.

- As was shown in Figures 5.13 and 5.14, the inlet of the coolant (where it is the coolest in its cycle) is around the exhaust manifold. It also can be seen in those figures that the exhaust manifold is completely surrounded by the coolant path, while the paths around the air-start cavity, and the spark plug are narrow and limited. Additionally, the coolant is much warmer when it reached the cylinder head area.

Another interesting observation is that the wall temperatures are lower very close to the intake ports. The low temperature of the mixtures inside the stuffing box (close to environment temperature) is why the areas closer to the intake ports are cooler. At IPO, the low-temperature scavenging flows enter the combustion chamber through the intake ports, cooling down the walls on the intake side.

It would be very helpful to look at the flame propagation characteristics at this point. Figure 5.27 shows the steps of flame propagation within a single combustion cycle. The flame front is assumed to be the isosurface of methane concentration of 1e-09, which represents the surface at which the fuel is almost all burnt. Following the sequence of figures, the flame kernel starts forming at about -6.5°ATDC. It then evolves and expands almost spherically up to TDC. It can be seen that the flame expands towards the cylinder head, and does not reach the piston crown until 2°ATDC. Since in-cylinder temperatures are rising until almost 30°ATDC when combustion ends, the parts which are closer to the flame front (spark plug and parts of the cylinder head) during this period, are expected to be hotter.

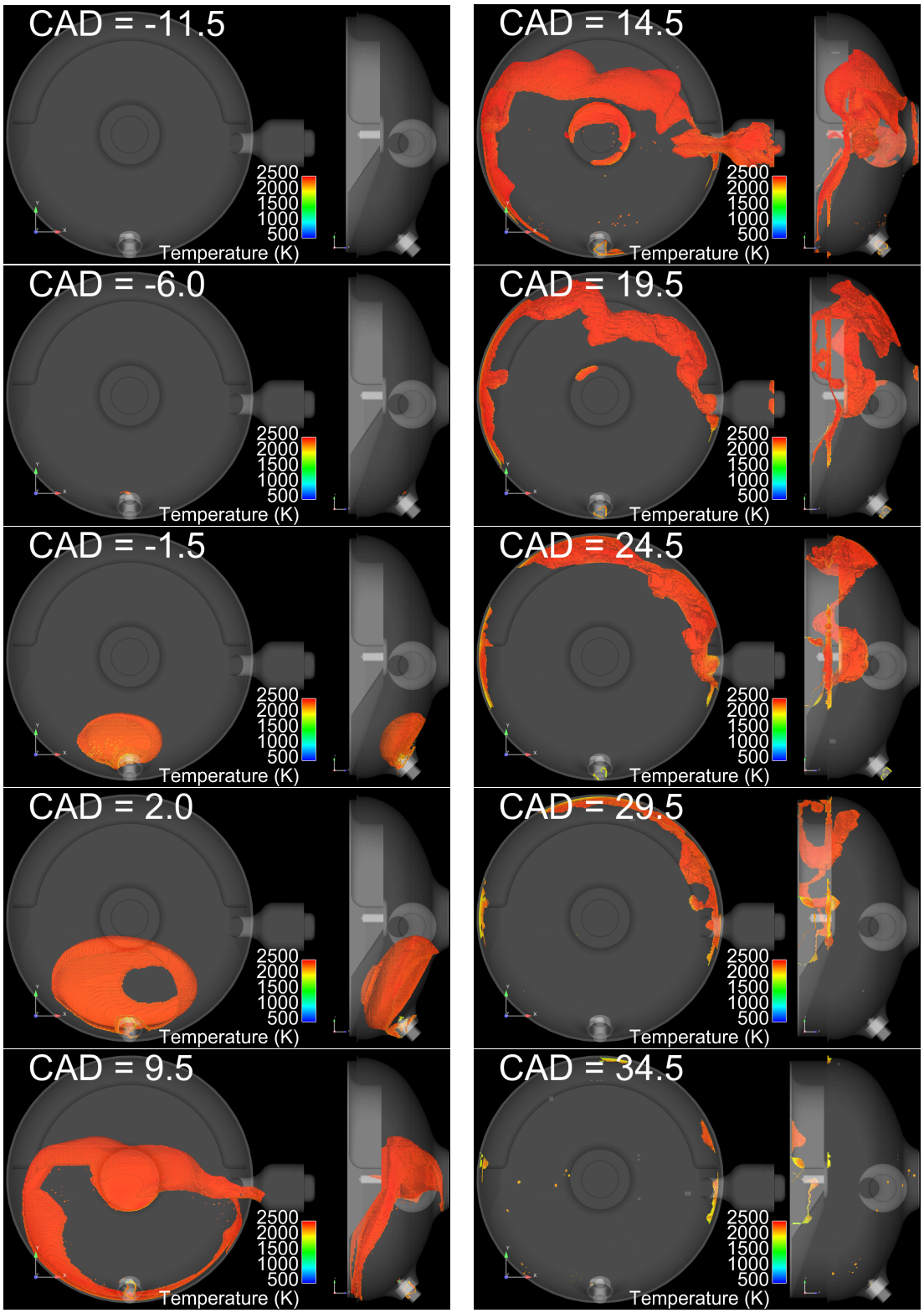

Figure 5.27: Flame front propagation within one combustion cycle

The temperature distribution on the cylinder head is presented in Figure 5.28. This temperature distribution can be easily explained by the flame front expansion behavior. As seen in Figure 5.27, and was explained before, the hot parts that are seen in Figure 5.28, are the areas which interact with the flame and/or combustion products the longest during one cycle.

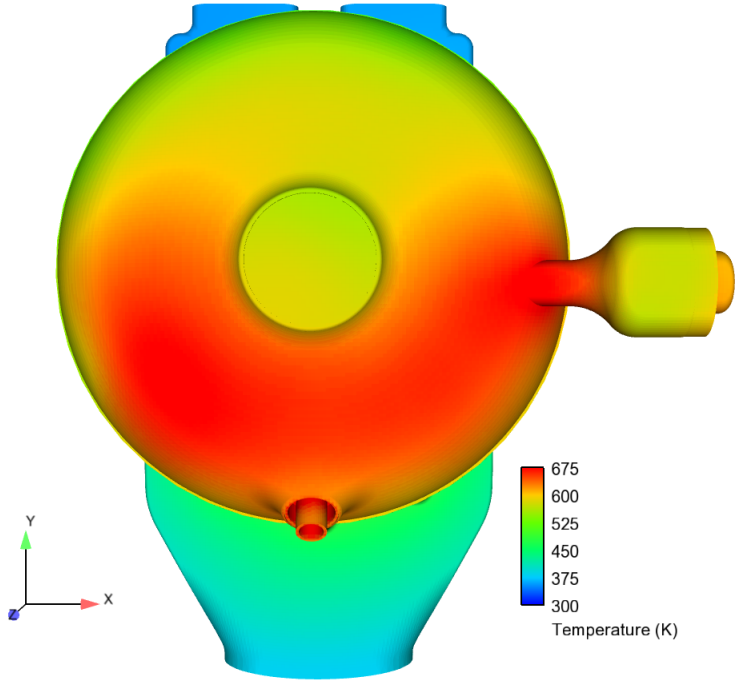

Figure 5.28: Temperature distribution on the cylinder head

Another interesting observation from Figure 5.28 is the hot surfaces around the neck of the air-start cavity. The reason for this phenomenon is the late arrival of the flame inside the cavity. It can be seen in Figure 5.27, that the flame front enters the cavity at about 9°ATDC. Because of the shape of the cavity, it acts as sort of a separate combustion chamber; the flame starts burning the mixture inside the cavity, rising its pressure and

temperature, which leads to burst of a high-temperature jet of fluids out of the cavity into the combustion chamber a few crank angles later. This phenomenon is shown in Figure 5.29. This hot jet is the reason, for having the hot surfaces around the neck of the air-start cavity. Additionally, as shown in Figure 5.13, the coolant paths do not surround the air-start cavity and especially its neck that well; hence; the edges get hotter than the rest.

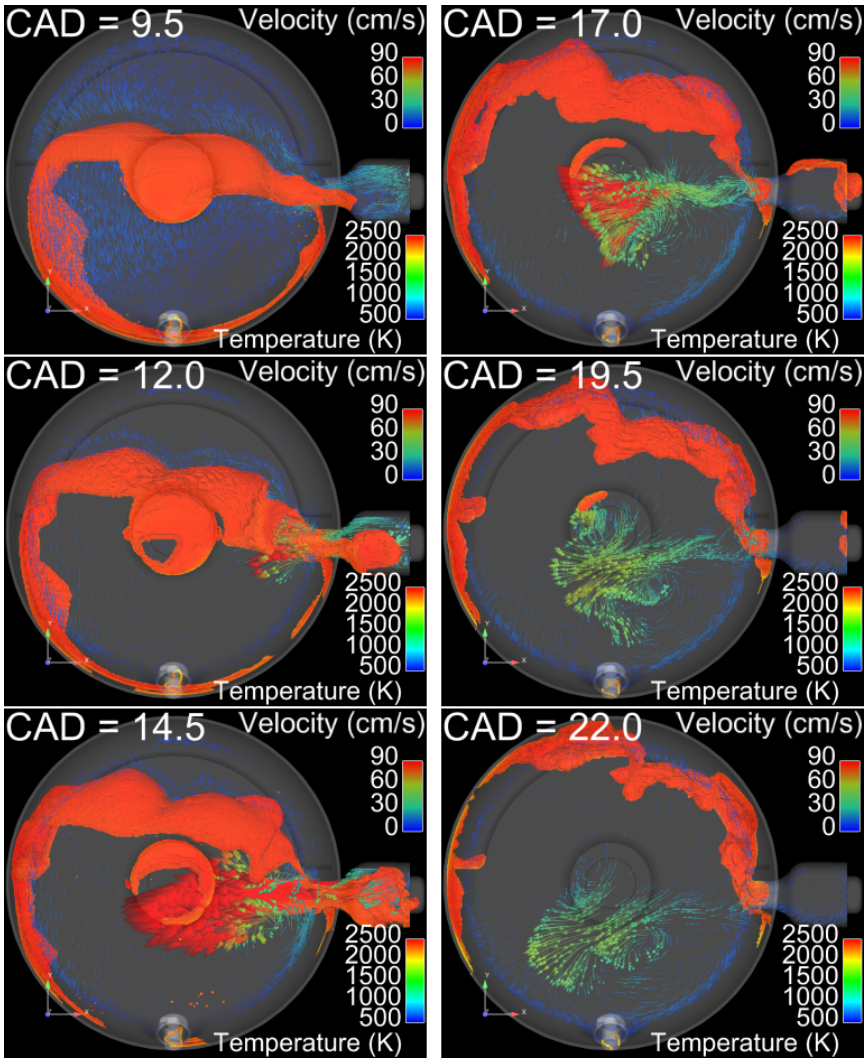

Figure 5.29: Velocity vectors on a plane on the center-line of the air-start cavity, along with the flame front

As expected, and as shown in Figure 5.30 (which shows inside of the cylinder head), the spark plug is the hottest piece in the combustion chamber. The coolant paths do not cover the areas around the spark plug that well, as shown in Figure 5.14. Additionally, the spark plug is inside the combustion chamber, and is emerged in flame and combustion products during the combustion cycle. The only cooling it gets, come from conduction through its body, and convection from the scavenging flows.

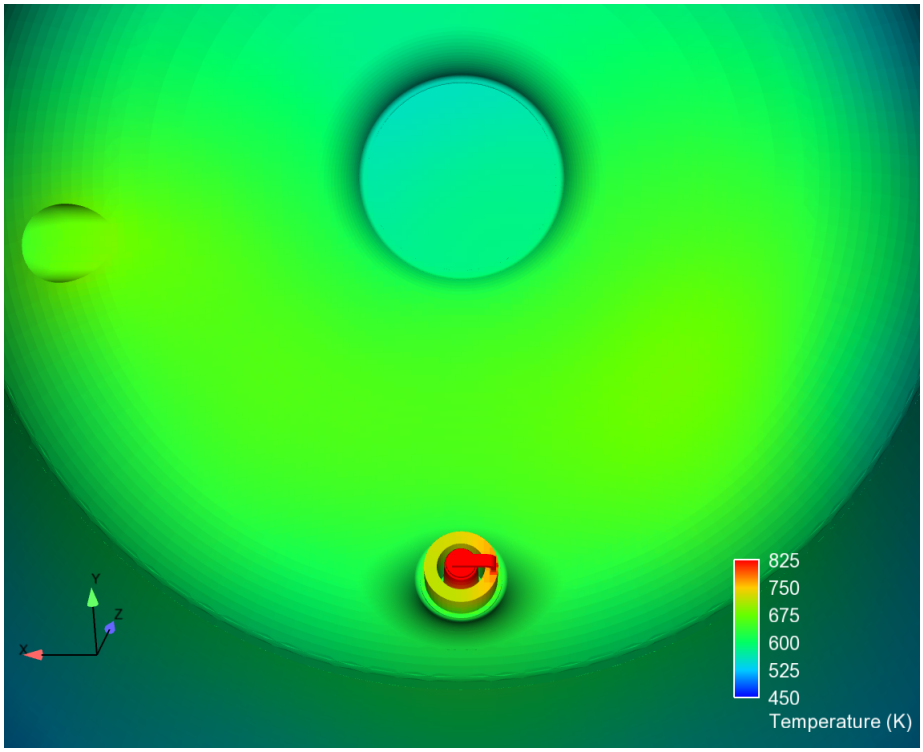

Figure 5.30: Temperature distribution on the inner surface of the cylinder head and around the spark plug

6. SUMMARY AND CONCLUSION

To improve the engine's performance, reduce its emission production, and re-design relevant parts for better mechanical endurance, the spatial temperature distribution in all the parts interfacing with the combustion chamber is required. For this purpose, the objective of the study was set to making a high-fidelity model capable of calculating the temperature distribution on these parts.

6.1 Summary

A thorough literature review was done. It was concluded that such a model requires a detailed and accurate simulation of all the processes that happen inside the engine; hence, the following tasks were defined and carried out:

- Simulation of the intake flows to the stuffing box through the reed valve:
  - FSI (fluid-structure interaction) methods were used to capture the body dynamics of the reed valve strips. Experimentally measured pressure profiles were used as boundary conditions for the air and fuel intake manifolds.
  - The simulation results were validated by matching the pressure of the stuffing box, as well as, the ability of the model in keeping the stuffing box's equivalence ratio within an acceptable range of the experimentally measured ϕ.
- Simulation of the gas exchange processes:
  - Geometries of the manifolds and ports were included to increase the accuracy of the numerical simulation.
  - Short-circuiting, trapping efficiency, and scavenging efficiency were calculated to be used for future improvements of the engine.

- Simulation of the combustion process:
  - The clearance volume (V_c) was experimentally measured. The geometry was then fine tuned to match the clearance volume of the engine.
  - SAGE detailed chemical kinetics solver was utilized with GRI-Mech 3.0 to accurately simulate the combustion process. The results were then validated by the experimentally data acquired from the engine.
  - It was understood that the simulations are capable of capturing the cyclic variation of the engine. The simulation results can later be used to find the culprit for the cyclic variation, and improve the engine's performance.
- Simulation of the conjugate heat transfer (CHT) process:
  - As it was not feasible to run the combustion and CHT simulations simultaneously, an iterative procedure was defined to couple the combustion simulation with the CHT simulation between the engine's cooling system and the solid parts interfacing with the combustion chamber.
  - The coolant flow rate and its temperature at the inlet were experimentally measured, and were used as boundary conditions for the simulation work.
  - To assess the effects of the coolant properties on the heat transfer characteristics of the engine, the simulations were done considering two different coolants: 1) water, 2) a 50-50 mixture of water and ethylene glycol.
  - The mean temperatures of both solid and coolant regions were used to check the convergence of the iterative process. It was concluded and shown that after four iterations, the temperatures converged.
  - A single experimental temperature measurement was done to validate the simulated temperature distribution. Additionally, a few monitor points were put at

different locations of the solid parts, and the convergence of the temperatures at these points were confirmed.

- It was shown that the changes in wall temperatures, affect the simulated combustion characteristics of the engine. This was observed in in-cylinder pressures, and ROHR curves.

With these tasks completed, the objective of the study was reached; a high-fidelity model, capable of simulating the conjugate heat transfer of a spark-ignited engine's cylinder, and providing the spatial temperature distribution in the solid parts interfacing with the combustion chamber.

6.2 Conclusions

The conclusions are divided into to subsections: 1) Reed Valve, Scavenging, and Combustion Simulation, and 2) CHT simulation.

6.2.1 Reed Valve, Scavenging, and Combustion Simulation

In the reed valve simulation section, it was proven that the use of FSI models along with experimentally measured boundary conditions is necessary for achieving accurate numerical results.

It was shown through short-circuiting calculations that the engine looses close to 40% of the fresh charge, leading to very high UHC emissions. A direct injection kit could be used to eliminate the UHC emissions through short-circuiting.

It was proven once again that the CFD tools are capable of simulating the combustion process accurately. These models are also able to capture the cyclic variation behavior of the engine. It was shown that the differences in flow field characteristics are the reasons for having so much CV.

6.2.2 CHT Simulation

Spatial temperature distribution on the combustion chamber walls was acquired through numerical simulations. The temperature distribution revealed that the wall temperatures are relatively higher near and around the spark plug and the air-start cavity. This observation suggests that the engine modification should center on either ensuring substantial durability to tolerate such high temperatures or improving heat transfer design to reduce the magnitude of temperatures at these locations.

An interesting observation was made that the combustion chamber wall temperatures influence the combustion characteristics; this was made obvious by looking at the in-cylinder pressure curves.

6.3 Future Work

The results of this study could later be used for these purposes, or be improved by the following suggestions:

1. The behavior of the reed valve could be analyzed, to improve the AFR control strategy of the engine.

2. The mixing of the air and fuel inside the stuffing box could be studied in detail, to come up with ways of improving the mixing characteristics.

3. It was shown in this study that the engine has high short-circuiting values; this is the main reason for the high UHC emissions of the engine. The shapes of the manifolds, and the piston crown could be modified in order to decrease the amount of fuel that is being lost due to short-circuiting.

4. As shown in the Combustion Simulation Results through experimental data, the engine has very high COV_{IMEP} values. It is shown in APPENDIX B, that the differences in flow development in the combustion chamber are the reasons for having

such high cyclic variation. The results of this study could be used to research the flow characteristics in much more detail, aiming to find solutions to reducing the COV_{IMEP}.

5. The results of the CHT simulations could be used for various improvements to the engine:
    - Redesign of relevant parts of the engine to increase their thermo-mechanical endurance.
    - An analysis could be done to assess the performance of the cooling system.
    - Local hot-spots could be eliminated by improving the cooling system. This would impact the combustion behavior and NO_x emission production of the engine.
6. The accuracy of the CHT simulation results could be improved by applying the following proposals:
    - Addition of the piston geometry to the conjugate heat transfer simulations.
    - Utilizing a nucleate boiling model, to capture the effects of the phase change phenomenon in the coolant fluid.
7. Most importantly, the use of this model can be expanded to other engines. All the above-mentioned studies then can be done for respective engines, for the same improvements.

REFERENCES

[1] J. B. Heywood and E. Sher, "The two-stroke cycle engine," *Warrendale, PA: Society of Automotive Engineers, 1999. 472*, 1999.

[2] J. Xin, S. Shih, E. Itano, and Y. Maeda, "Integration of 3D combustion simulations and conjugate heat transfer analysis to quantitatively evaluate component temperatures," 2003.

[3] "AJAX E-565 gas engine," 2014.

[4] C. Arcoumanis and J. H. Whitelaw, "Fluid mechanics of internal combustion engines -a review," *Proceedings of the Institution of Mechanical Engineers, Part C: Journal of Mechanical Engineering Science*, vol. 201, no. 1, pp. 57–74, 1987.

[5] T. D. Butler, L. D. Cloutman, J. K. Dukowicz, and J. D. Ramshaw, "Multidimensional numerical simulation of reactive flow in internal combustion engines," *Progress in Energy and Combustion Science*, vol. 7, no. 4, pp. 293–315, 1981.

[6] S.-C. Kong, Z. Han, and R. D. Reitz, "The development and application of a diesel ignition and combustion model for multidimensional engine simulation," Tech. Rep. 0148-7191, SAE Technical Paper, 1995.

[7] W. W. Pulkrabek, *Engineering fundamentals of the internal combustion engine*. Upper Saddle River, N.J.: Pearson Prentice Hall, 2004.

[8] R. Stone, *Introduction to internal combustion engines*. SAE International, 4th ed., 2012.

[9] A. Mashayekh, T. Jacobs, M. Patterson, and J. Etcheverry, "Prediction of air-fuel ratio control of a large bore natural gas engine using cfd modeling of reed valve dynamics," *International Journal of Engine Research*, 2017.

[10] J. B. Heywood, *Internal combustion engine fundamentals*. McGraw-Hill series in mechanical engineering, New York: McGraw-Hill, 1988.

[11] G. A. Lavoie, J. B. Heywood, and J. C. Keck, "Experimental and theoretical study of nitric oxide formation in internal combustion engines," *Combustion Science and Technology*, vol. 1, no. 4, pp. 313–326, 1970.

[12] R. D. Reitz, "Directions in internal combustion engine research," *Combustion and Flame*, vol. 160, no. 1, pp. 1–8, 2013.

[13] E. T. Hinds and G. P. Blair, "Unsteady gas flow through reed valve induction systems," 1978.

[14] G. P. Blair, E. T. Hinds, and R. Fleck, "Predicting the performance characteristics of two-cycle engines fitted with reed induction valves," 1979.

[15] R. Fleck, G. P. Blair, and R. A. R. Houston, "An improved model for predicting reed valve behaviour in two-stroke cycle engines," 1987.

[16] W. Mitianiec and A. Bogusz, "Theoretical and experimental study of gas flow through reed valve in a two-stroke engine," 1996.

[17] G. Cunningham, R. J. Kee, and J. Boyall, "CFD prediction of crankcase flow regimes in a crankcase scavenged two-stroke engine," 1997.

[18] G. Cunningham, R. J. Kee, and R. G. Kenny, "Reed valve modelling in a computational fluid dynamics simulation of the two-stroke engine," *Proceedings of the Institution of Mechanical Engineers, Part D: Journal of Automobile Engineering*, vol. 213, no. 1, pp. 37–45, 1999.

[19] F. F. S. Matos, A. T. Prata, and C. J. Deschamps, "Numerical simulation of the dynamics of reed type valves," 2002.

[20] Y. Zeng, S. Strauss, P. Lucier, and T. Craft, "Predicting and optimizing two-stroke engine performance using multidimensional CFD," 2004.

[21] M. Battistoni, C. N. Grimaldi, R. Baudille, M. Fiaccavento, and M. Marcacci, "Development of a model for the simulation of a reed valve based secondary air injection system for si engines," 2005.

[22] R. J. Rothbauer, G. Grasberger, Z. Abidin, and R. A. Almbauer, "Reed valve, crankcase and exhaust models coupled to 3d fluid domains for the predictive CFD simulation," tech. rep., SAE Technical Paper, 2007.

[23] N. Govindan, V. Jayaraman, R. S. Venkatasamy, and M. Ramasamy, "Mathematical modeling and simulation of a reed valve reciprocating air compressor," *Thermal Science*, vol. 13, no. 3, pp. 47–58, 2009.

[24] D. Jajcevic, R. Almbauer, S. Schmidt, K. Glinsner, and M. Fitl, "Reed valve CFD simulation of a 2-stroke engine using a 2D model including the complete engine geometry," *SAE Int. J. Engines*, vol. 3, no. 2, pp. 448–461, 2010.

[25] I. Gonzalez, O. Lehmkuhl, A. Naseri, J. Rigola, and A. Oliva, "Fluid-structure interaction of a reed type valve," 2016.

[26] M. E. G. Sweeney, G. G. Swann, R. G. Kenny, and G. P. Blair, "Computational fluid dynamics applied to two-stroke engine scavenging," Tech. Rep. 0148-7191, SAE Technical Paper, 1985.

[27] J. G. Smyth, R. G. Kenny, and G. P. Blair, "Steady flow analysis of the scavenging process in a loop scavenged two-stroke cycle engine -a theoretical and experimental study," Tech. Rep. 0148-7191, SAE Technical Paper, 1988.

[28] E. Sher, "Scavenging the two-stroke engine," *Progress in Energy and Combustion Science*, vol. 16, no. 2, pp. 95–124, 1990.

[29] E. Sher, I. Hossain, Q. Zhang, and D. E. Winterbone, "Calculations and measurements in the cylinder of a two-stroke uniflow-scavenged engine under steady flow conditions," *Experimental thermal and fluid science*, vol. 4, no. 4, pp. 418–431, 1991.

[30] Y. G. Lai, A. J. Przekwas, and R. L. T. Sun, "Three-dimensional computation of the scavenging flow process in a motored two-stroke engine," Tech. Rep. 0148-7191, SAE Technical Paper, 1993.

[31] C. W. Dekanski, M. I. G. Bloor, and M. J. Wilson, "A parametric model of a 2-stroke engine for design and analysis," *Computer methods in applied mechanics and engineering*, vol. 137, no. 3, pp. 411–425, 1996.

[32] B. D. Raghunathan and R. G. Kenny, "CFD simulation and validation of the flow within a motored two-stroke engine," Tech. Rep. 0148-7191, SAE Technical Paper, 1997.

[33] S. Mc Elligott, R. Douglas, R. G. Kenny, and S. Glover, "An assessment of a stratified scavenging process applied to a loop scavenged two-stroke engine," Tech. Rep. 0148-7191, SAE Technical Paper, 1999.

[34] F. Payri, J. Galindo, H. Climent, J. M. Pastor, and C. Gaia, "Optimisation of the scavenging and injection processes of an air-assisted direct fuel injection 50 cc. 2-stroke SI engine by means of modelling," Tech. Rep. 0148-7191, SAE Technical Paper, 2001.

[35] J. Benajes, R. Novella, D. De Lima, P. Tribotte, N. Quechon, P. Obernesser, and V. Dugue, "Analysis of the combustion process, pollutant emissions and efficiency of an innovative 2-stroke HSDI engine designed for automotive applications," *Applied Thermal Engineering*, vol. 58, no. 1, pp. 181–193, 2013.

[36] M. Garg, D. Kumar, M. Syed, and S. Nageswara, "CFD modelling of a two stroke engine to predict and reduce short circuit losses," *SAE International Journal of Engines*, vol. 9, no. 2015-32-0702, pp. 355–364, 2015.

[37] R. D. Reitz and C. J. Rutland, "Development and testing of diesel engine CFD models," *Progress in Energy and Combustion Science*, vol. 21, no. 2, pp. 173–196, 1995.

[38] H. Jasak, J. Y. Luo, B. Kaludercic, A. D. Gosman, H. Echtle, Z. Liang, F. Wirbeleit, M. Wierse, S. Rips, A. Werner, G. Fernstrom, and A. Karlsson, "Rapid CFD simulation of internal combustion engines," 1999.

[39] P. K. Senecal, *Development of a methodology for internal combustion engine design using multi-dimensional modeling with validation through experiments*. Ph.D., The University of Wisconsin - Madison, 2000.

[40] S.-C. Kong and R. D. Reitz, "Application of detailed chemistry and CFD for predicting direct injection HCCI engine combustion and emissions," *Proceedings of the Combustion Institute*, vol. 29, no. 1, pp. 663–669, 2002.

[41] M. C. Drake, T. D. Fansler, and A. M. Lippert, "Stratified-charge combustion: modeling and imaging of a spray-guided direct-injection spark-ignition engine," *Proceedings of the Combustion Institute*, vol. 30, no. 2, pp. 2683–2691, 2005.

[42] S. X. Cheng and J. S. Wallace, "Modeling of ignition and combustion for glow plug assisted direct injection natural gas engines," *Proceedings of the ASME Internal Combustion Engine Division Fall Technical Conference - 2012*, pp. 767–779, 2012.

[43] X. Yang, A. Solomon, and T.-W. Kuo, "Ignition and combustion simulations of spray-guided SIDI engine using arrhenius combustion with spark-energy deposition model," 2012.

[44] Z. Wang, R. Scarcelli, S. Som, S. McConnell, N. Salman, Y. Zhu, K. Hardman, K. Freeman, R. Reese, P. K. Senecal, M. Raju, and S. Givler, "Multi-dimensional modeling and validation of combustion in a high-efficiency dual-fuel light-duty engine," 2013.

[45] M. Raju, M. Wang, M. Dai, W. Piggott, and D. Flowers, "Acceleration of detailed chemical kinetics using multi-zone modeling for CFD in internal combustion engine simulations," 2012.

[46] J. Etcheverry, M. Patterson, and D. Grauer, "Modern design methods applied to the redesign of a legacy large bore, two-stroke cycle, spark ignited gas engine," in *ASME 2013 Internal Combustion Engine Division Fall Technical Conference*, American Society of Mechanical Engineers, 2013.

[47] J. Etcheverry, M. Patterson, and D. Grauer, "Virtual design of an industrial, large-bore, spark-ignited, natural gas, internal combustion engine for reduction of regulated pollutant emissions," in *ASME 2013 Internal Combustion Engine Division Fall Technical Conference*, American Society of Mechanical Engineers, 2013.

[48] S. D. Givler, M. Raju, E. Pomraning, P. K. Senecal, N. Salman, and R. Reese, "Gasoline combustion modeling of direct and port-fuel injected engines using a reduced chemical mechanism," 2013.

[49] A. C. Alkidas, "Heat transfer characteristics of a spark-ignition engine," *Journal of Heat Transfer*, vol. 102, no. 2, pp. 189–193, 1980.

[50] A. C. Alkidas and J. P. Myers, "Transient heat-flux measurements in the combustion chamber of a spark-ignition engine," *Journal of Heat Transfer*, vol. 104, no. 1, pp. 62–67, 1982.

[51] C. Angelberger, T. Poinsot, and B. Delhay, "Improving near-wall combustion and wall heat transfer modeling in SI engine computations," Tech. Rep. 0148-7191, SAE Technical Paper, 1997.

[52] M. S. Baniasad, E. Khalil, and F. Shen, "Exhaust valve thermal management and robust design using combustion and 3D conjugate heat transfer simulation with 6-sigma methodology," 2006.

[53] V. Esfahanian, A. Javaheri, and M. Ghaffarpour, "Thermal analysis of an SI engine piston using different combustion boundary condition treatments," *Applied Thermal Engineering*, vol. 26, no. 2, pp. 277–287, 2006.

[54] E. Urip, K. H. Liew, and S. L. Yang, "Modeling IC engine conjugate heat transfer using the KIVA code," *Numerical Heat Transfer, Part A: Applications*, vol. 52, no. 1, pp. 1–23, 2007.

[55] E. Urip and S.-L. Yang, "An efficient IC engine conjugate heat transfer calculation for cooling system design," 2007.

[56] S. Fontanesi and E. V. McAssey, "Experimental and numerical investigation of conjugate heat transfer in a HSDI diesel engine water cooling jacket," 2009.

[57] S. Fontanesi, G. Cicalese, and M. Giacopini, "Multiphase CFD-CHT analysis and optimization of the cooling jacket in a v6 diesel engine," Tech. Rep. 0148-7191, SAE Technical Paper, 2010.

[58] S. Fontanesi, G. Cicalese, A. D'Adamo, and G. Pivetti, "Validation of a CFD methodology for the analysis of conjugate heat transfer in a high performance SI engine," 2011.

[59] Y. Li and S.-C. Kong, "Coupling conjugate heat transfer with in-cylinder combustion modeling for engine simulation," *International Journal of Heat and Mass Transfer*,

vol. 54, no. 11, pp. 2467–2478, 2011.

[60] S. Fontanesi and M. Giacopini, "Multiphase CFD-CHT optimization of the cooling jacket and FEM analysis of the engine head of a v6 diesel engine," *Applied Thermal Engineering*, vol. 52, no. 2, pp. 293–303, 2013.

[61] H. Punekar and S. Das, "Numerical simulation of subcooled nucleate boiling in cooling jacket of IC engine," 2013.

[62] S. Fontanesi, G. Cicalese, G. Cantore, and A. D'Adamo, "Integrated in-cylinder/CHT analysis for the prediction of abnormal combustion occurrence in gasoline engines," Tech. Rep. 0148-7191, SAE Technical Paper, 2014.

[63] O. Iqbal, K. Arora, and M. Sanka, "Thermal map of an IC engine via conjugate heat transfer: Validation and test data correlation," 2014.

[64] S. Jahangirian, A. Srivastava, S. A. Hosseini, S. Ballard, N. Wu, and J. Kiedaisch, "A multi-physics 3D modeling methodology for multi-cylinder diesel engine thermal management and fatigue life prediction," 2015.

[65] G. Cicalese, F. Berni, and S. Fontanesi, "Integrated in-cylinder / CHT methodology for the simulation of the engine thermal field: An application to high performance turbocharged DISI engines," 2016.

[66] P. Kundu, R. Scarcelli, S. Som, A. Ickes, Y. Wang, J. Kiedaisch, and M. Rajkumar, "Modeling heat loss through pistons and effect of thermal boundary coatings in diesel engine simulations using a conjugate heat transfer model," 2016.

[67] A. Griffin, *Combustion Characteristics of a Two-Stroke Large Bore Natural Gas Spark-Ignited Engine*. M.Sc. thesis, Texas A&M University, 2015.

[68] "Water cooled absolute pressure sensor, type 4049a," 2010.

[69] J. Brown, S. Chakravarthy, T. Kroeger, and Y. Sun, "Instrumenting a thermosiphon cooling system on a large-bore two-stroke spark-ignited natural gas engine," tech. rep., 2016.

[70] "Gas analysis report," Tech. Rep. 04016300, Hicks Dry Plant, 03/03/2015 2015.

[71] O. Redlich and J. N. S. Kwong, "On the thermodynamics of solutions. v. an equation of state. fugacities of gaseous solutions," *Chemical Reviews*, vol. 44, no. 1, pp. 233–244, 1949.

[72] *CONVERGE Manual (CONVERGE CFD 2.2).* CONVERGE CFD (TM), 2015.

[73] G. P. Smith, D. M. Golden, M. Frenklach, N. W. Moriarty, B. Eiteneer, M. Goldenberg, C. T. Bowman, R. K. Hanson, S. Song, J. William C. Gardiner, V. V. Lissianski, and Z. Qin, "GRI MECH 3.0," 1999.

[74] A. Babajimopoulos, D. N. Assanis, D. L. Flowers, S. M. Aceves, and R. P. Hessel, "A fully coupled computational fluid dynamics and multi-zone model with detailed chemical kinetics for the simulation of premixed charge compression ignition engines," *International journal of engine research*, vol. 6, no. 5, pp. 497–512, 2005.

[75] *CONVERGE Manual (CONVERGE CFD 2.3).* CONVERGE CFD (TM), 2016.

[76] A. M. Lippert, S. Chang, S. Are, and D. P. Schmidt, "Mesh independence and adaptive mesh refinement for advanced engine spray simulations," 2005.

[77] E. Pomraning, K. Richards, and P. K. Senecal, "Modeling turbulent combustion using a RANS model, detailed chemistry, and adaptive mesh refinement," 2014.

[78] Q. Xue and S.-C. Kong, "Development of adaptive mesh refinement scheme for engine spray simulations," *Computers & Fluids*, vol. 38, no. 4, pp. 939–949, 2009.

[79] A. A. Amsden, "KIVA-3V: A block-structured KIVA program for engines with vertical or canted valves," tech. rep., Los Alamos National Lab., NM (United States), 1997.

[80] S. R. Turns, "An introduction to combustion: concepts and applications," *McGraw-Hill series in mechanical engineering.*, 2000.

[81] P. K. Senecal, E. Pomraning, K. J. Richards, T. E. Briggs, C. Y. Choi, R. M. McDavid, and M. A. Patterson, "Multi-dimensional modeling of direct-injection diesel spray liquid length and flame lift-off length using CFD and parallel detailed chemistry," 2003.

[82] Z. Han and R. D. Reitz, "Turbulence modeling of internal combustion engines using $RNG\ k-\varepsilon$ models," *Combustion science and technology*, vol. 106, no. 4-6, pp. 267–295, 1995.

[83] M. Biruduganti, S. Gupta, B. Bihari, S. McConnell, and R. Sekar, "Air separation membranes: An alternative to EGR in large bore natural gas engines," *Journal of Engineering for Gas Turbines and Power*, vol. 132, no. 8, p. 082804, 2010.

[84] H. Gao, M. J. Hall, O. A. Ezekoye, and R. D. Matthews, "Railplug design optimization to improve large-bore natural gas engine performance," pp. 15–23, American Society of Mechanical Engineers, 2005.

[85] K. D. Beaty and C. C. D. Wood, "Integral gas compressor engines: Cylinder balancing, NOx, and efficiency," vol. 1, p. 9, American Society of Mechanical Engineers, 1997.

[86] M. Abraham and S. Prakash, "A theory of cyclic variations in small two-stroke cycle spark ignited engines - an analytical validation of experimentally observed behaviour," 1992.

[87] J. W. Daily, "Cycle-to-cycle variations: a chaotic process?," Tech. Rep. 0148-7191, SAE Technical Paper, 1987.

[88] M. B. Young, "Cyclic dispersion-some quantitative cause-and-effect relationships," Tech. Rep. 0148-7191, SAE Technical Paper, 1980.

[89] G. Karim, "An examination of the nature of the random cyclic pressure variations in a spark-ignition engine," *Journal of the Institute of Petroleum*, vol. 53, no. 519, pp. 112–120, 1967.

[90] R. E. Winsor and D. J. Patterson, "Mixture turbulence-a key to cyclic combustion variation," Tech. Rep. 0148-7191, SAE Technical Paper, 1973.

[91] B. D. Peters and G. L. Borman, "Cyclic variations and average burning rates in a si engine," Tech. Rep. 0148-7191, SAE Technical Paper, 1970.

[92] F. A. Matekunas, "Modes and measures of cyclic combustion variability," Tech. Rep. 0148-7191, SAE Technical Paper, 1983.

[93] P. G. Hill, "Cyclic variations and turbulence structure in spark-ignition engines," *Combustion and flame*, vol. 72, no. 1, pp. 73–89, 1988.

[94] J. G. Hansel, "Lean automotive engine operation-hydrocarbon exhaust emissions and combustion characteristics," Tech. Rep. 0148-7191, SAE Technical Paper, 1971.

[95] M. B. Young, "Cyclic dispersion in the homogeneous-charge spark-ignition engine-a literature survey," Tech. Rep. 0148-7191, SAE Technical Paper, 1981.

[96] R. S. Jupudi, C. E. A. Finney, R. Primus, S. Wijeyakulasuriya, A. E. Klingbeil, B. Tamma, and M. K. Stoyanov, "Application of high performance computing for simulating cycle-to-cycle variation in dual-fuel combustion engines," Tech. Rep. 0148-7191, SAE Technical Paper, 2016.

[97] R. Scarcelli, N. S. Matthias, and T. Wallner, "Numerical and experimental analysis of ignition and combustion stability in EGR dilute GDI operation," pp. V001T03A015–V001T03A015, American Society of Mechanical Engineers, 2014.

[98] R. Scarcelli, J. Sevik, T. Wallner, K. Richards, E. Pomraning, and P. K. Senecal, "Capturing cyclic variability in EGR dilute SI combustion using multi-cycle RANS," pp. V002T06A010–V002T06A010, American Society of Mechanical Engineers, 2015.

[99] K. Richards, D. Probst, E. Pomraning, P. K. Senecal, and R. Scarcelli, "The observation of cyclic variation in engine simulations when using RANS turbulence modeling," pp. V002T06A010–V002T06A010, American Society of Mechanical Engineers, 2014.

APPENDIX A

FORMULATIONS

A.1 Fluid Structure Interaction (FSI)

For this model, the stress tensor will be integrated over the surfaces if the FSI object; the results of this integral will be the fluid force:

$$F_{fluid-i} = \int_S (-P\delta_{ij} + \sigma_{ij}) n_j dS \tag{A.1}$$

In this equation, n_j is the normal vector, P is the pressure, and σ_{ij} represents the viscous stress tensor. In the next step, the total moment ($M_{fluid-i}$) could be calculated using Equation A.2:

$$M_{fluid-i} = \int_S \varepsilon_{ijk} r_j (-P\delta_{kl} + \sigma_{kl}) n_j dS \tag{A.2}$$

In which, ε_{ijk} is the Levi-Civita symbol, and r_j is the center of mass distance from the surface boundary.

Then, the governing equation for the translational motion of the center of mass will be solved, using Equation A.3:

$$\Sigma F_{external-i} + F_{fluid-i} = m\ddot{x}_i \tag{A.3}$$

In which, m is the mass, and the displacement of the center of mass of the FSI object in the direction, is represented by $\ddot{x}_i$. [75]

A.2 Formulation of Chemical Kinetics with Multi-Step Mechanisms

A chemical reaction mechanism with multiple steps can be written as the following [80]:

$$\sum_{n=1}^{N} v'_{n,r} X_n \Leftrightarrow \sum_{n=1}^{N} v''_{n,r} X_n, \text{ for } r = 1, 2, \cdots, R \text{ (total number of reactions)} \tag{A.4}$$

In this reaction, $v'_{n,r}$ and $v''_{n,r}$ are respectively the stoichiometric coefficients of the reactants and products sides of the reaction, for species n and reaction r. Then the net production rate of the species n can be calculated using Equation A.5:

$$\dot{\omega}_n = \sum_{r=1}^{R} v_{n,r} q_r, \text{ for } n = 1, 2, \cdots, N \text{ (total number of species)} \tag{A.5}$$

Where $v_{n,r} = v''_{n,r} - v'_{n,r}$. In Equation A.5, q_r stands for the rate-of-progress variable, for the r^{th} elementary reaction; it can be formulated as:

$$q_r = k_{fr} \prod_{n=1}^{N} [X_n]^{v'_{n,r}} - k_{rr} \prod_{n=1}^{N} [X_n]^{v''_{n,r}} \tag{A.6}$$

In this equation, $[X_n]$ represents the molar concentration of species n, and k_{fr}, and k_{rr} are respectively the forward and reverse rate coefficients for reaction r. SAGE uses Equation A.7 for reaction forward rate coefficient, which is expressed in Arrhenius form [72, 81].

$$k_{fr} = A_r T^{b_r} \exp(-E_r / R_u T) \tag{A.7}$$

In which, A_r is the pre-exponential factor, b_r is the temperature exponent, E_r stands for the reaction activation energy, and finally R_u is the universal gas constant.

In addition, the backward rate coefficient (k_{rr}), can either be specified as another equation, like Equation A.7, or can be calculated from equilibrium coefficient, k_{cr}:

$$k_{rr} = \frac{k_{fr}}{k_{cr}} \tag{A.8}$$

The k_{cr}, which stands for the equilibrium constant depends on the thermodynamic properties, and is calculated by:

$$k_{cr} = \exp\left(\frac{\Delta S_r^0}{R} - \frac{\Delta H_r^0}{RT}\right) \cdot \left(\frac{P_{atm}}{RT}\right)^{\sum_{n=1}^{N} v_{n,r}} \tag{A.9}$$

And the terms in Equation A.9 are described as the following:

- P_{atm}: the atmospheric pressure
- R: the gas constant
- T: temperature
- $\frac{\Delta S_r^0}{R} = \sum_{n=1}^{N} v_{n,r} \frac{S_n^0}{R}$, S: entropy
- $\frac{\Delta H_r^0}{R} = \sum_{n=1}^{N} v_{n,r} \frac{H_n^0}{R}$, H: enthalpy

Using all the above presented equations, the mass and energy conservation equations can be written as Equation A.10 and Equation A.11 respectively.

$$\frac{d[X_n]}{dt} = \dot{\omega_n} \tag{A.10}$$

$$\frac{dT}{dt} = \frac{V\frac{dP}{dt} - \sum_{n=1}^{N}\left(\bar{h}_n \dot{\omega}_n\right)}{\sum_{n=1}^{N}\left([X_n]\bar{c}_{p,n}\right)} \tag{A.11}$$

In Equation A.11, the terms are described as:

- V: volume
- T: temperature
- P: pressure
- $\bar{h}_n$: molar specific enthalpy of species n
- $\bar{c}_{p,n}$: molar constant-pressure specific heat of species n

All of these equations are solved in each time-step; based on the results, species are updated appropriately in each cell.

A.3 Reynolds Averaged Navier-Stokes (RANS)

As explained in [72, 82], the flow variables such as velocity will be decomposed into two terms as presented in Equation A.12:

$$\underbrace{u_i}_{\text{instantaneous velocity}} = \underbrace{\bar{u}_i}_{\text{ensemble mean}} + \underbrace{u_i'}_{\text{fluctuating}} \tag{A.12}$$

This decomposition is then substituted in the Navier-Stokes equation resulting in Equation A.13 for the mass transport, and Equation A.14 for the momentum transport:

$$\frac{\partial \bar{\rho}}{\partial t} + \frac{\partial \bar{\rho}\tilde{u}_j}{\partial x_j} = 0 \tag{A.13}$$

$$\frac{\partial \bar{\rho}\tilde{u}_i}{\partial t} + \frac{\partial \bar{\rho}\tilde{u}_i\tilde{u}_j}{\partial x_j} = -\frac{\partial \bar{P}}{\partial x_i} + \frac{\partial}{\partial x_j}\left[\mu\left(\frac{\partial \tilde{u}_i}{\partial x_j} + \frac{\partial \tilde{u}_j}{\partial x_i}\right) - \frac{2}{3}\mu\frac{\partial \tilde{u}_k}{\partial x_k}\delta_{ij}\right] + \frac{\partial}{\partial x_j}\big(-\bar{\rho}\widetilde{u_i'u_j'}\big) \tag{A.14}$$

Where $\tilde{u}_i \equiv \dfrac{\overline{\rho u_i}}{\bar{\rho}}$. The last terms of Equation A.14 ($-\bar{\rho}\widetilde{u_i'u_j'}$) are called Reynolds stresses, which represent the effects of turbulence. These stress terms should be modeled

for solving Equation A.14. Equation A.15 is used to model the Reynolds stress terms for the standard $k-\varepsilon$ and RNG models.

$$\tau_{ij} = -\bar{\rho}\widetilde{u_i' u_j'} = 2\mu_t S_{ij} - \frac{2}{3}\delta_{ij}\left(\rho k + \mu_t \frac{\partial \tilde{u}_i}{\partial x_i}\right) \tag{A.15}$$

Where μ_t (turbulent viscosity) is given by $\mu_t = c_\mu \rho \dfrac{k^2}{\varepsilon}$. In the definition of the turbulent viscosity, the term k (turbulent kinetic energy) is defined by $k = \dfrac{1}{2}\widetilde{u_i' u_i'}$. Also c_μ is a tuning model constant, which can be changed for any particular flow, and ε is the dissipation of the turbulent kinetic energy. The term S_{ij} in Equation A.15, represents the mean strain rate tensor, and is given by:

$$S_{ij} = \frac{1}{2}\left(\frac{\partial \tilde{u}_i}{\partial x_j} + \frac{\partial \tilde{u}_j}{\partial x_i}\right) \tag{A.16}$$

Turbulent diffusion and turbulent conductivity terms are used to account for the turbulence in mass transport and energy transport equations. These terms are defined by Equation A.17 and Equation A.18 respectively.

$$D_t = \left(\frac{1}{\mathrm{Sc}_t}\right),\ \mathrm{Sc}_t : \text{turbulent Schmidt number} \tag{A.17}$$

$$K_t = \left(\frac{1}{\mathrm{Pr}_t}\right)\mu_t c_p',\ \mathrm{Pr}_t : \text{turbulent Prandtl number} \tag{A.18}$$

Obtaining the turbulent viscosity μ_t, for the RNG $k-\varepsilon$ model requires additional transport equations; one for the turbulent kinetic energy, k:

$$\frac{\partial \rho k}{\partial t} + \frac{\partial \rho u_i k}{\partial x_i} = \tau_{ij}\frac{\partial u_i}{\partial x_j} + \frac{\partial}{\partial x_j}\frac{\mu}{\mathrm{Pr}_k}\frac{\partial k}{\partial x_j} - \rho\varepsilon + \frac{c_s}{1.5}S_s \tag{A.19}$$

And one for the dissipation of the turbulent kinetic energy, ε:

$$\frac{\partial \rho\varepsilon}{\partial t} + \frac{\partial (\rho u_i \varepsilon)}{\partial x_i} = \frac{\partial}{\partial x_j}\left(\frac{\mu}{\mathrm{Pr}_\varepsilon}\frac{\partial \varepsilon}{\partial x_j}\right) + c_{\varepsilon 3}\rho\varepsilon\frac{\partial u_i}{\partial x_i} + \left(c_{\varepsilon 1}\frac{\partial u_i}{\partial x_j}\tau_{ij} - c_{\varepsilon 2}\rho\varepsilon + c_s S_s\right)\frac{\varepsilon}{k} + S_\rho R \tag{A.20}$$

In the above equation, S represents the user-supplied source term. For the $RNG\ k-\varepsilon$ method, which is used for the simulations, Equation A.21 defines R:

$$R = \frac{C_\mu \eta^3 (1-\eta/\eta_0)}{(1+\beta\eta^3)}\frac{\varepsilon^2}{k} \tag{A.21}$$

And $\eta = \dfrac{k}{\varepsilon}|S_{ij}| = \dfrac{k}{\varepsilon}\sqrt{2S_{ij}S_{ij}}$.

APPENDIX B

CYCLIC VARIATION

It is known that the lean-burn 2-stroke engines in general are prone to cyclic variation. There are many reports available of the research works done to find out the culprit for having so much cyclic variation in 2-stroke engines, trying to improve their performance.

B.1 Literature Review

Many factors influence the cyclic variations in engines; it has been shown that the CV decreases as the equivalence ratio (ϕ) increases from lean towards stoichiometric [83, 84]. In addition, CV has been shown to affect the peak pressures; an increase in peak pressures was observed with reduction of CV [85].

Many researchers have tried to find the root cause of the cyclic variation; it appears that the general consensus is that the delay in the transition of the flame kernel into a developed flame front is what contributes the most to the CV [86, 87, 88, 89]. This transition happens in a small portion of the combustion chamber (very close to the spark plug); this suggests that probably the factors local to the spark plug are more dominant than averaged values in the whole combustion chamber [86, 90, 91]. These local factors include, but are not limited to poor scavenging near the spark plug [86, 89, 92], flow field characteristics (e.g. velocity and turbulence) near the spark plug at spark timing [90, 92, 93], and equivalence ratio (ϕ) in the vicinity of the spark plug [89, 94].

There is only one global factor that has been mentioned to affect the CV. It is known that the flame speed increases at air-fuel ratios closer to stoichiometric, and that an increase in flame speed generally results in lower CV; hence, the global ϕ is shown to impact the cyclic variation. [95]

It has been shown that the cyclic variation is influenced by load and speed of the engine. In high speed engines, an increase in speed would increase turbulence, which might blow-out the flame kernel and discourage its growth. This might not be the case for this engine, since this engine's rated speed is 525 RPM. On the other hand, increasing load generally decreases the cyclic variation. At higher loads, the engine runs at a richer global equivalence ratio, which as mentioned earlier reduces the CV. [67]

CFD numerical simulations could be used to look into the cyclic variation phenomenon in more details. It has been shown that LES models are capable of simulating the CV in engines, but these simulations are very time-consuming and expensive. Recently, it has been proven that the RANS models (which are far less expensive) are also capable of capturing the CV behavior of engines. To achieve this, small time steps, higher-order numerical schemes, and finer grids should be utilized for the simulation work. [96, 97, 98, 99]

In the current study numerical simulation was used to study all the contributing factors to CV, trying to isolate the most influential factor. The results of this study could later be used to improve the engine's performance by reducing the cyclic variation.

B.2 Results and Discussion

As mentioned in the previous section, it was shown that by using finer grids, and proper high-order numerical schemes, cyclic variation can be observed even by using a RANS solver. This can be seen in Figure B.1, where the numerically simulated chamber pressures are presented, and are compared with experimental data. It can be seen how the numerical simulation has captured the good (cycles #1, #4, #6, and #8) and the bad (cycles #2,#3, #5, and #7) cycles. It has to be noted that the order of good/bad cycles are not the same in experimental and numerical results, because there is no good/bad pattern to the cycles, and they happen randomly.

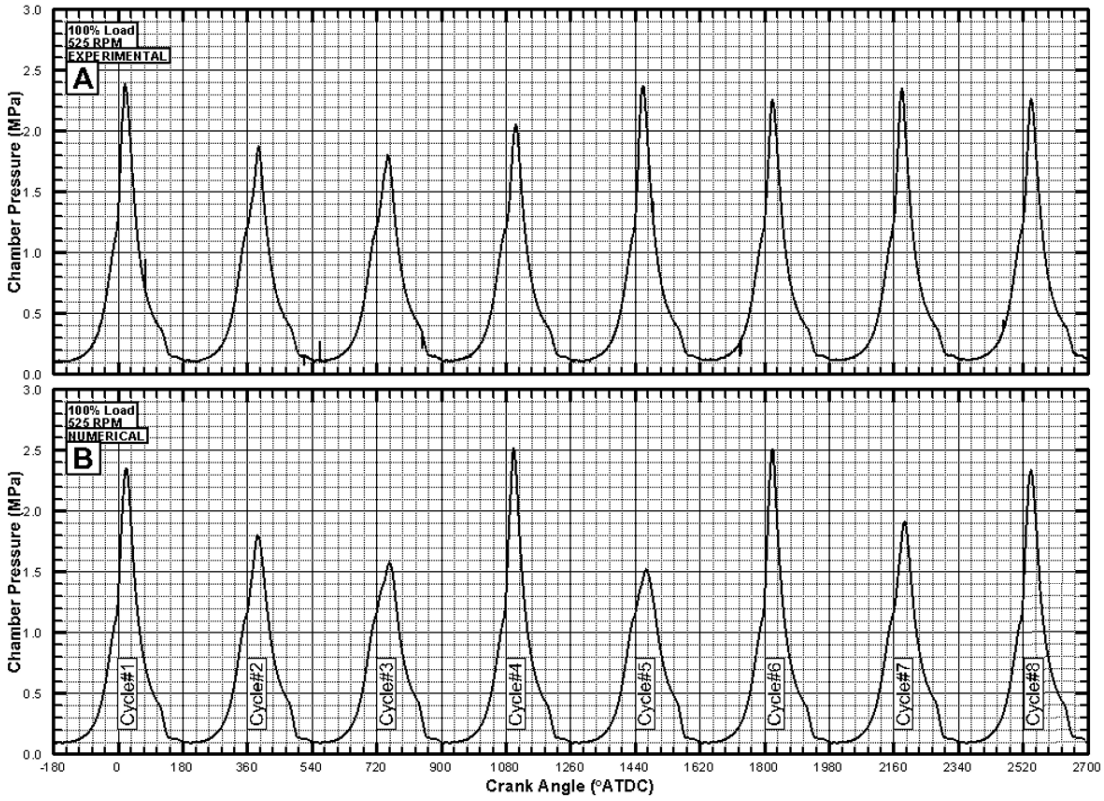

Figure B.1: (A) experimental and (B) simulated sequential in-cylinder pressures for 100% load and 525 RPM conditions

The numerical simulation results were then used to look into the details of the combustion process, trying to find out the culprit for the observed cyclic variation. Please note that from this point forward, the good cycles are colored green, while the bad cycles are shown in red.

Figure B.2 shows the heat release rate for all the simulated cycles. It is clear in the graph that the rate of heat release is much higher for the good cycles (e.g. cycle#7), compared to the bad cycles (e.g. cycle #6). The higher slopes of ROHR at the initial part of the combustion for the good cycles, implies a faster flame speed. It also should be noted that the bad cycles have a longer heat release duration (slow-burn), while the good cycles have a narrower heat release duration (fast-burn).

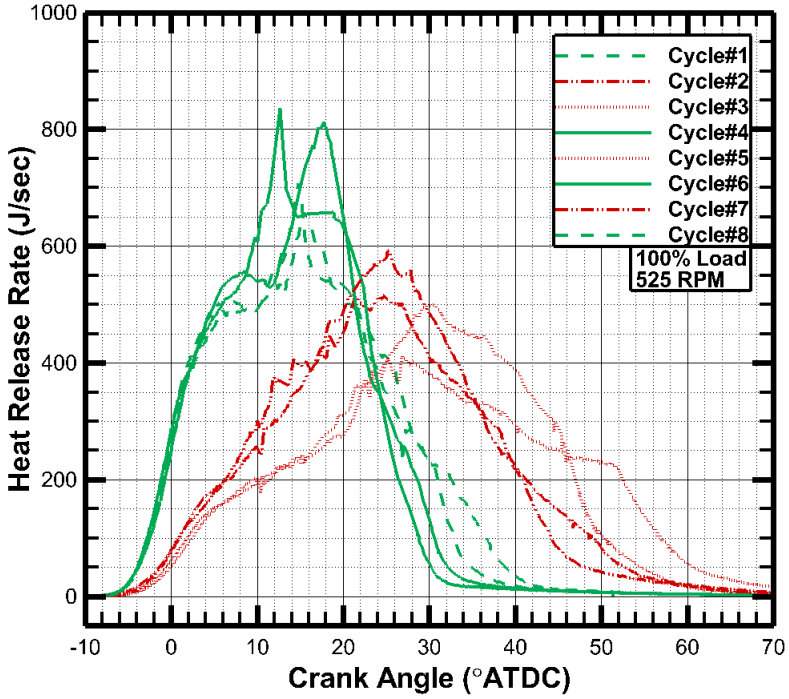

Figure B.2: Simulated heat release rate for all the cycles

It was mentioned in the Literature Review, that one of the global variables which influences the CV is the trapped ϕ of the combustion chamber. Figure B.3 presents this value for all the cycles, and it can be seen that the trapped ϕ does not significantly change for these cycles; hence, it cannot be concluded that the trapped ϕ is the dominant factor causing the CV. In addition, the figure includes the chamber's trapped mass, which again does not vary that significantly, and can be ruled out as the main cause of the observed CV.

The mixing characteristics of the trapped mixture could also be an important factor affecting the combustion rate. Figure B.4 shows the distribution of the trapped cells within each range of equivalence ratio (ϕ). It can be seen that except for cycle #2, for almost all the rest of cycles, all the trapped cells are within ϕ-range of 0.8 to 0.9. This means that all the cycles have comparable mixing at the ignition timing. This observation rules out mixing as the main reason for having this much CV.

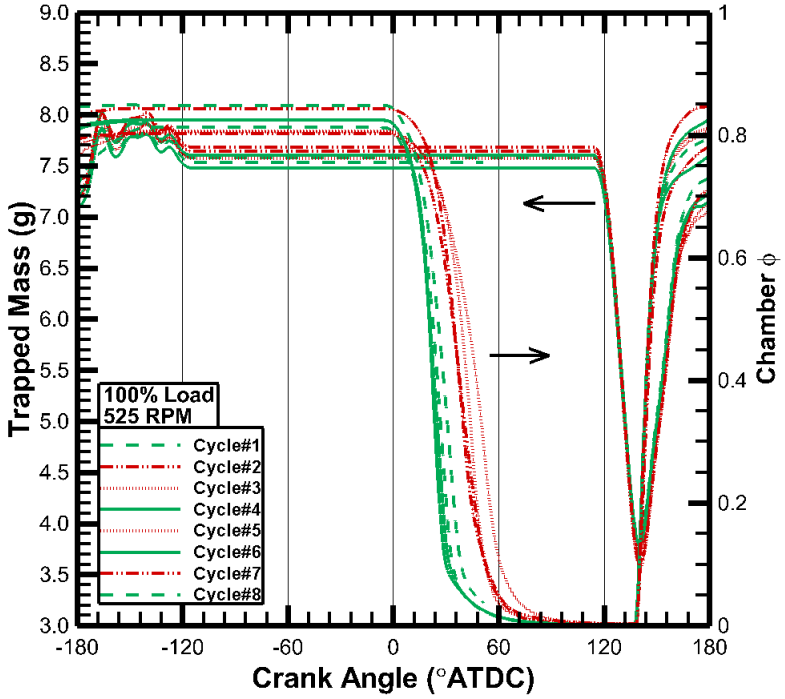

Figure B.3: Trapped ϕ and trapped mass inside the combustion chamber

It was mentioned in the Literature Review that factors local to the spark plug are more likely to cause the delay in the transitioning of the initial flame kernel into a developed flame front, which can increase the CV. For this purpose, a few local variables were studied as well. The first variable was the equivalence ratio in the vicinity of the spark plug, as presented in Figure B.5. It is evident in the graph that the changes in the ϕ values near the spark plug from one cycle to another are minimal. It also is clear that there are both good and bad cycles with slightly richer or leaner than average mixtures. This means that most probably the ϕ near the spark plug is not the controlling factor for the CV.

Another important factor local to the spark plug is the turbulent kinetic energy (TKE) which is presented in Figure B.6. It can be seen in this plot that the better cycles have higher TKE values; this suggests that the difference in velocity field near the spark plug could be the reason for having cyclic variation in this engine. TKE is calculated by Equa-

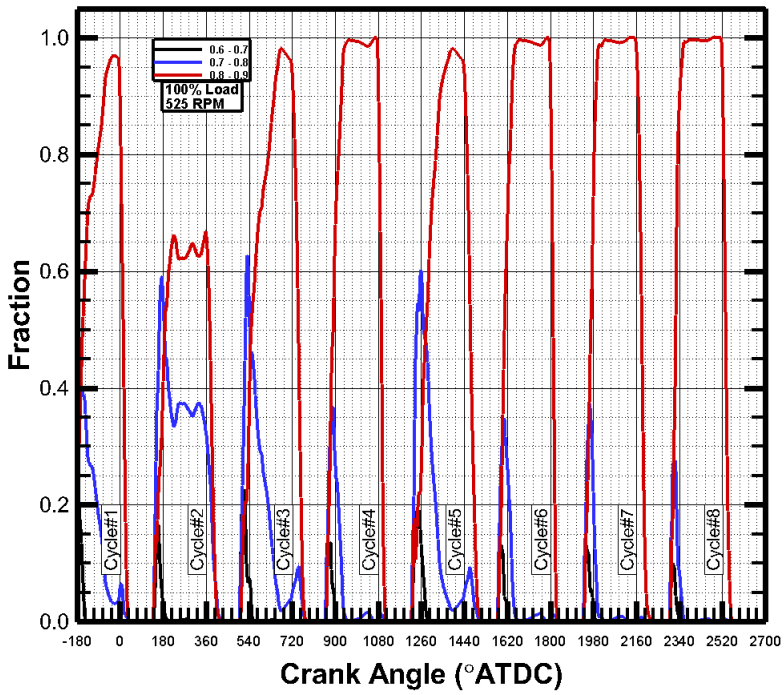

Figure B.4: Fraction of trapped mixture within each equivalence ratio (ϕ) range for all the cycles

tion B.1, and includes all the components of the velocity vector. Further analysis seems required to realize which of the three components of the velocity is the most influential factor.

$$\text{TKE} = \frac{1}{2}\left(\overline{(u')^2} + \overline{(v')^2} + \overline{(w')^2}\right) \tag{B.1}$$

In order to look at individual velocity components, swirl ratio, tumble ratio x, and tumble ratio y were plotted. Before presenting the results, it would be helpful to take another look at Figures 4.2 and 4.4 to better understand the coordinates.

Swirl ratio which represents the rotational velocity around the Z-axis is shown in Figure B.7 . The swirl ratio is averaged in the whole combustion chamber. As shown in this figure, most of the good cycles had larger absolute values for the swirl ratio during the

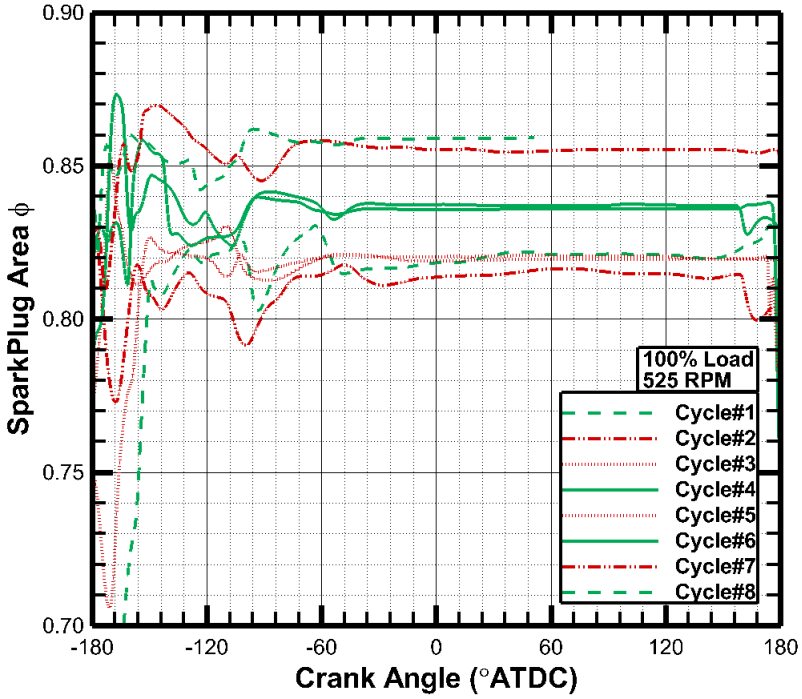

Figure B.5: Equivalence ratio (ϕ) in the vicinity of the spark plug

scavenging process. It also is very interesting that the swirl ratio for all the good cycles has the same shape or profile. This implies that the flow is being developed differently for the good cycles.

In addition to swirl ratio, tumble ratio X and tumble ratio Y were plotted. The results are presented in Figures B.8 and B.9 respectively. It can be seen in Figure B.8 that the good cycles have a different behavior as bad ones; the tumble ratio X decreases much faster for the good cycles, and is slightly lower at spark timing. On the other hand, Figure B.9 shows a very distinct pattern for the good cycles. The absolute values of the tumble ratio Y are much higher during the scavenging process for the good cycles. Additionally, the tumble ratio Y absolute values are almost 10 times higher than the bad cycles at the spark timing.

A look at the flame front expansion behavior reveals interesting observations. It can

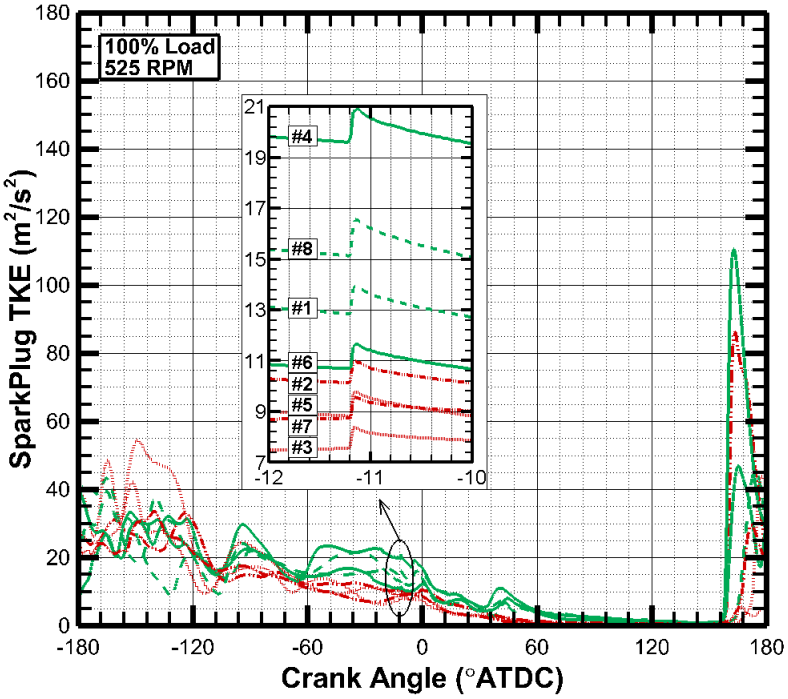

Figure B.6: TKE (turbulent kinetic energy) at the vicinity of the spark plug

be observed that for a bad cycle, unlike the good cycles (shown in Figure 5.27), the flame front expands much slower. Also, the shapes of the flame fronts are clearly distinguishable. Both of these are mostly happening because of the explained differences in the velocity fields inside the combustion chamber and around the spark plug.

To better look at these mentioned differences in flow fields, velocity vectors could be used. ordinarily, for some geometries having a cut plane of the velocity field is helpful, but in this case with its complicated geometry there is no reasonable 2D view that provides meaningful information, thus the velocity vector figures are not included in the dissertation.

Scavenging process is what develops the flow field inside the combustion chamber. Since swirl ratio, tumble ratio X, tumble ratio Y, and TKE were concluded to be the reason for having the observed CV, it can be stated with confidence that the 'scavenging process'

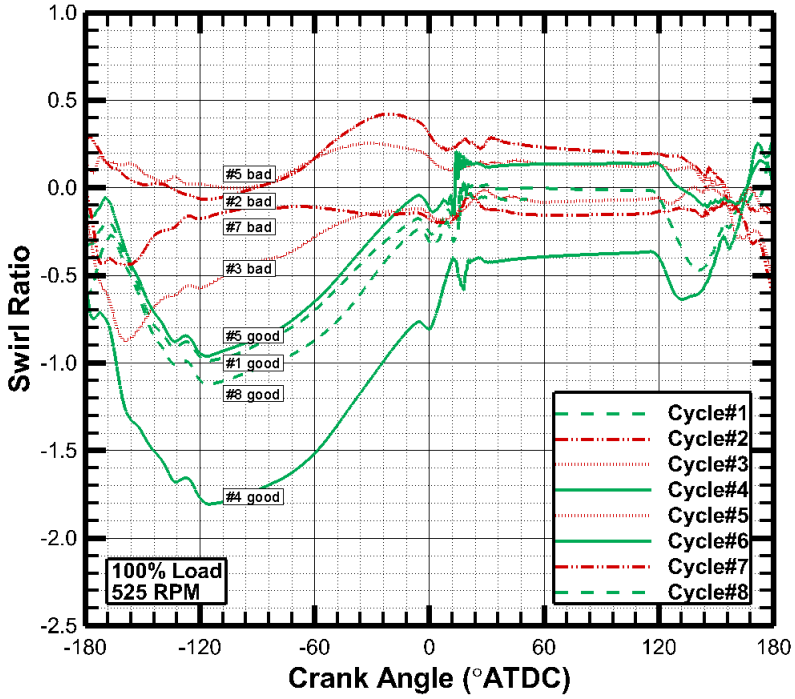

Figure B.7: Crank angle resolved swirl ratio in the combustion chamber

is the main culprit for such a high cyclic variation.

Further detailed studies are required to find out why the scavenging process varies as it does. A causation analysis could later result in a significantly improved engine performance.

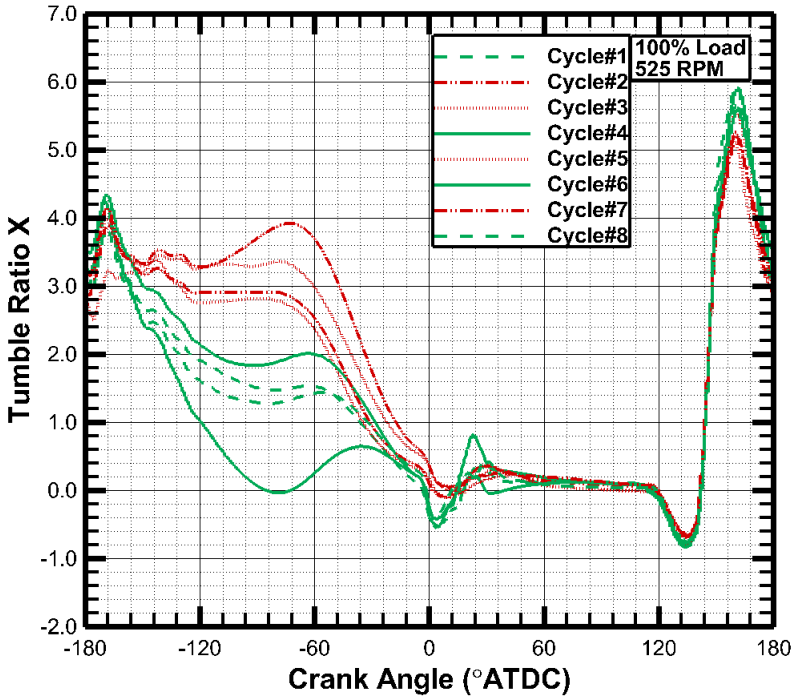

Figure B.8: Crank angle resolved tumble ratio X in the combustion chamber

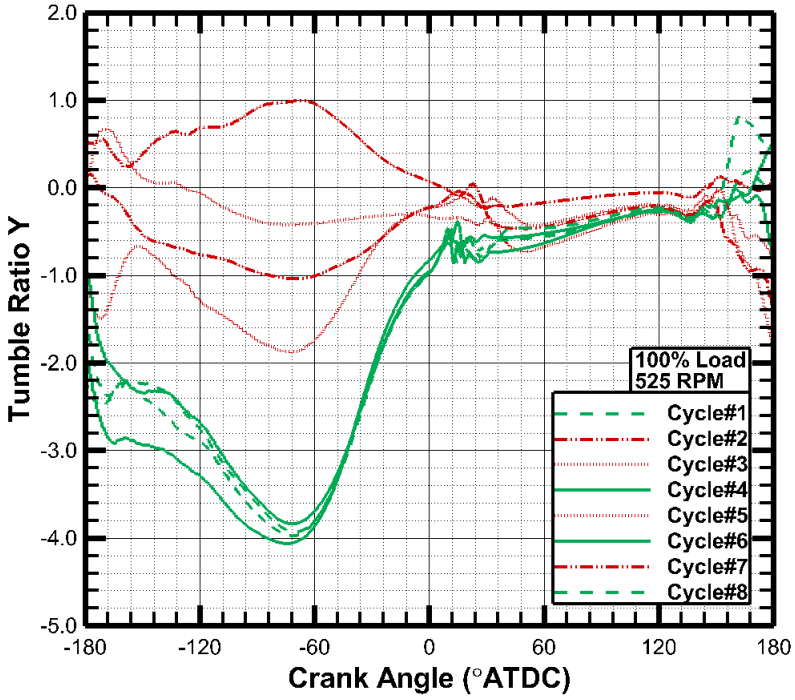

Figure B.9: Crank angle resolved tumble ratio Y in the combustion chamber

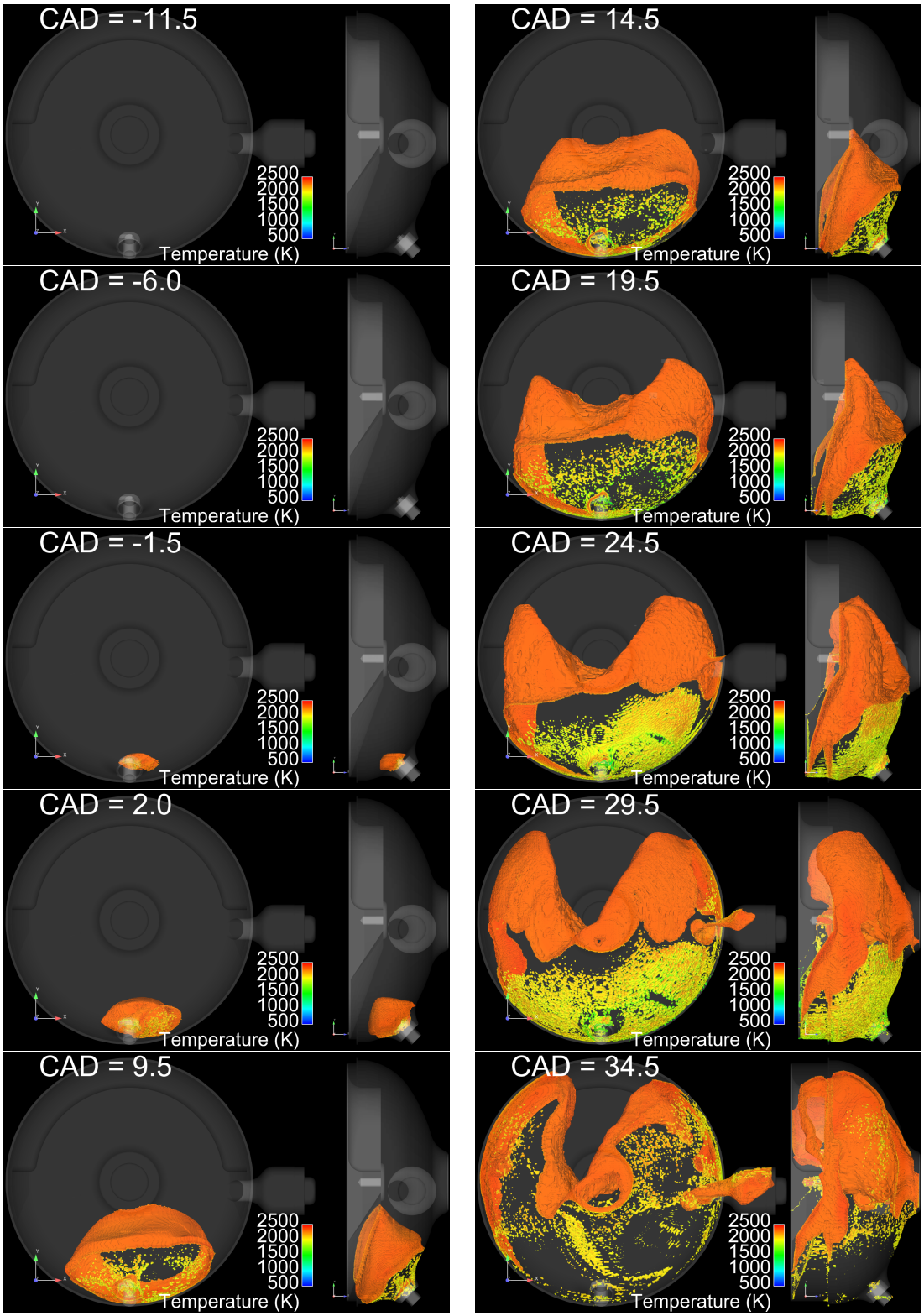

Figure B.10: Flame front propagation within one bad combustion cycle